

# Wireless Communications

## University of Kiel

Prof. Dr.-Ing. Dirk Manteuffel

### **Coupling element antennas for small terminals based on the characteristic modes**

Robert Ledig





1. Gutachter Prof. Dr.-Ing. Dirk Manteuffel
2. Gutachter Prof. Ph.D. Cyril Luxey
3. Gutachter Prof. Dr.-Ing. Klaus Solbach

Datum der mündlichen Prüfung: 13.11.2015



**Coupling element antennas for small terminals  
based on the characteristic modes**

**Dissertation**

zur Erlangung des akademischen Grades  
Doktor der Ingenieurwissenschaften (Dr.-Ing.)  
der Technischen Fakultät der  
Christian Albrechts-Universität zu Kiel

**Robert Ledig**

geb. Martens

Kiel

13.11.2015



Hiermit versichere ich, dass ich die Doktorarbeit

**Coupling element antennas for small terminals based on the characteristic modes**

selbständig und ohne unzulässige fremde Hilfe angefertigt habe und dass ich alle von anderen Autoren wörtlich übernommenen Stellen, wie auch die sich an die Gedankengänge anderer Autoren eng anlehnenden Ausführungen meiner Arbeit, besonders gekennzeichnet und die entsprechenden Quellen angegeben habe. Weiterhin wurde die Arbeit ausschließlich an der Christian-Albrechts-Universität zu Kiel im Rahmen eines Prüfungsverfahrens vorgelegt, jedoch wurden Teile in Form von Beiträgen in Fachzeitschriften und Tagungsbänden veröffentlicht bzw. zur Veröffentlichung eingereicht (siehe Abschnitt zu Publikationen). Diese Arbeit ist unter Einhaltung der Regeln guter wissenschaftlicher Praxis der Deutschen Forschungsgemeinschaft entstanden.

**Robert Ledig**

geb. Martens





# Abstract

Future mobile communication systems use the broadband and multiple antenna technology (MIMO) to increase the spatial efficiency of the transmission channel and therefore provide higher data rates over a particular frequency range. However, the implementation of multi-antenna systems on small mobile terminals is very challenging. Multiple antenna elements require additional space on the small handheld devices, and they suffer from large distances to each other. In addition, the antenna elements should be decoupled as possible with respect to their polarization and its radiation pattern. The last requirement can be currently difficult to overcome, due to the fact that all antennas are using the same electrical reference platform, respectively the chassis of the terminal itself.

In this thesis, the Theory of Characteristic Modes (TCM) was followed, which allows principally the use of the orthogonal chassis modes, decomposed out of the current density distribution, in order to design broadband and multiple antenna systems.

A major challenge was the development of suitable coupling structures to excite several modes independently. Here, the capacitive, the inductive and the hybrid coupling concepts were discussed and compared for the selective coupling of the characteristic modes. A reconstruction of the resulting radiation patterns and the calculation of the power coefficient realized the specific coupling of the modes, the respective power budget and antenna matching as well. In particular, the results indicated a direct relationship between the characteristic modes and the low correlation of the transfer functions in multi-antenna systems. In order to show a direct coupling of the several concepts, different kind of feeding networks at the feed-point of the investigated coupling element have been developed and evaluated. Moreover, they include the power splitter and the matching networks as well.

On the development of multi-band and broadband antennas, different coupling concepts for the common coupling of several modes have been investigated. This kind of excitation could be realized by using the coupling elements itself as a tuning element or by using space efficient matching networks at the feeding port.

The results of this thesis reveals the utilization of the theory of characteristic modes for

the design of the space efficient multi-antenna systems, as well as multi-band and broad-band antennas by direct coupling of the chassis itself. In addition, the approach was evaluated as a useful analysis and synthesis tool for developing integrated antenna systems on small mobile terminals.

# Zusammenfassung

Zukünftige mobile Kommunikationssysteme verwenden die Breitband-, als auch MIMO- (Multiple Input Multiple Output) Antennentechnologie, um die räumliche Effizienz des Übertragungskanals zu steigern und somit höhere Datenraten über einen bestimmten Frequenzbereich zu ermöglichen. Die damit verbundene Implementierung von Mehrantennensystemen stellt insbesondere in kleinen Endgeräten eine große Herausforderung dar. Zum einen erfordert eine Vielzahl von Antennen zusätzlichen Raum in den ohnehin vom Streben nach hoher Integrationsdichte getriebenen Geräten. Zum anderen müssen die Einzelstrahler bei der Verwendung üblicher Konzepte möglichst weit voneinander im Gerät platziert werden. Zudem sollen Sie hinsichtlich ihrer Polarisation und ihres Richtdiagramms möglichst entkoppelt sein. Gerade die letzte Forderung lässt sich gegenwärtig nur schwer realisieren, da alle Antennen dieselbe elektrische Bezugsplattform, nämlich das Chassis des Endgeräts, verwenden müssen.

In dieser Dissertation wurde die Theorie der Charakteristischen Moden verfolgt, die es grundsätzlich ermöglicht, orthogonale Moden der Stromdichteverteilung auf dem Chassis selbst als Breitband- und Mehrantennensystem zu verwenden.

Eine wesentliche Herausforderung war die Entwicklung geeigneter Koppelstrukturen mit denen mehrere dieser Moden auf der gewählten Plattform unabhängig voneinander angeregt werden können. Hierbei wurden kapazitive, induktive und hybride Koppelkonzepte für die selektive Einkopplung der Charakteristischen Moden verfolgt und verglichen. Eine Rekonstruktion der resultierenden Richtcharakteristiken und die Berechnung der Leistungskoeffizienten, machte es möglich Rückschlüssen auf die gezielte Einkopplung der Moden, deren Leistungsbudget und Antennenanpassung zu geben. Insbesondere indizierten die Ergebnisse den direkten Bezug der Charakteristischen Moden zu einer geringen Korrelation der Übertragungsfunktionen in Mehrantennensystemen. Um eine direkte Einkopplung der verschiedenen Konzepte zu verfolgen, wurden verschiedene Speisetzwerke entwickelt und evaluiert, welche Leistungsteiler und Anpassnetzwerke an den Fusspunkten der Koppler beinhalteten.

Zur Entwicklung von Mehrband- und Breitbandantennen wurden mehrere Koppelkonzepte zur gemeinsamen Einkopplung verschiedener Moden entwickelt. Diese konnten mit und ohne Hilfe von Anpassnetzwerken platzeffizient aufgebaut und evaluiert werden.

Die Ergebnisse dieser Dissertation zeigen, dass mittels der Theorie der Charakteristischen Moden platzeffiziente Mehrantennensystem als auch Mehrband- und Breitbandantennen durch die Ankopplung des Chassis selbst realisiert werden können. Zudem erwies sich der gewählte Ansatz als hilfreiches Analyse- und Syntheseinstrument zur Entwicklung integrierter Antennensysteme.

## Danksagung

Die vorliegende Arbeit entstand während meiner Tätigkeit als wissenschaftlicher Mitarbeiter in der Arbeitsgruppe für Funkkommunikation der Christian-Albrechts-Universität zu Kiel.

An dieser Stelle möchte ich mich ganz besonders bei Herrn Prof. Dr.-Ing. Dirk Manteuffel bedanken, der mir die Möglichkeit gegeben hat, in dem spannenden Feld der neuartigen Antennentechnik zu forschen und zu promovieren. Ich bin dankbar für die vielen Diskussionen, den fachlichen Rat und die Freiheit in der Ausgestaltung der Forschungsschwerpunkte.

Für das Interesse an dieser Arbeit und die Übernahme des Koreferats danke ich Herrn Prof. Ph.D. Cyril Luxey und Herrn Prof. Dr.-Ing. Klaus Solbach. Ebenso bedanke ich mich bei dem Vorsitzenden der Promotionskommission Herrn Prof. Dr.-Ing. Peter Adam Höher und dem Prüfer Herrn Prof. Dr.-Ing. Michael Höft.

Ein großes Dankeschön geht an die gesamte Arbeitsgruppe Funkkommunikation für die gute Zusammenarbeit. Ganz besonders möchte ich mich bei meinen Kollegen Markus Grimm, Eugen Safin, D.Sc. (Tech.) Risto Valkonen, Yi Chen, Florian Marx, Thade Wunderlich und Gastwissenschaftler D.Sc. (Tech.) Jari Holopainen für die gemeinsame Zeit bedanken. Hierbei seien besonders die fachlichen Diskussionen hervorzuheben, die zum Gelingen dieser Arbeit beigetragen haben.

Darüber hinaus möchte ich mich bei meiner Familie und meinen Freunden für die offenen Ohren und den Rat in allen Lebenslagen bedanken.

Mein ganz besonderer Dank gilt meiner Frau Katja, die mich mit großem Verständnis und unermüdlicher Geduld von Anfang an unterstützt hat.



# Content

<b>Abstract</b> .....	<b>I</b>
<b>Zusammenfassung</b> .....	<b>III</b>
<b>Danksagung</b> .....	<b>V</b>
<b>List of Author’s Publications and Contributions</b> .....	<b>XI</b>
<b>Notation Remarks</b> .....	<b>XV</b>
<b>1. Introduction</b> .....	<b>1</b>
1.1 Background .....	1
1.2 Objective of this work.....	2
1.3 Contents and organization of the thesis.....	3
1.4 Main scientific merits.....	5
<b>2. The Theory of Characteristic Modes</b> .....	<b>7</b>
2.1 The impedance operator and the generalized eigenvalue problem .....	7
2.2 Orthogonal properties of the characteristic modes.....	9
2.3 Orthogonal properties of the modal eigenfields.....	10
2.4 Modal field energies and eigenvalues .....	12
2.5 Modal solution of the characteristic modes and characteristic fields.....	13
2.6 Modal solution of the complex power.....	14
<b>3. The RWG Edge Elements and its Relation to the TCM</b> .....	<b>17</b>
3.1 RWG edge elements.....	17
3.2 Modal excitation concepts.....	19
3.3 Input admittance and impedance.....	22
3.4 Modal complex power including the modal excitation .....	24

<b>4. Modal Analysis of Simple Radiation Structures.....</b>	<b>27</b>
4.1 Modal analysis of a small rectangular strip.....	28
4.1.1 Analysis of the eigenvalues, the eigenfields and the current distributions.....	28
4.1.2 Modal significance .....	30
4.1.3 Modal radiating bandwidth and quality factor analysis .....	31
4.2 Modal analysis based on a parameter study of a small generic plate .....	32
4.2.1 Variation example of the minor axis .....	32
4.2.2 Modal radiation $Q$ .....	34
4.3 Modal analysis of simple dipole antennas.....	36
4.3.1 Modal power coefficient based on the characteristic mode analysis.....	37
4.3.2 Numerical analysis of dipole antennas based on the characteristic mode analysis.....	39
<b>5. Selective Excitation of the Characteristic Modes of the Small Rectangular Plate</b>	<b>51</b>
5.1 Modal analysis of a small rectangular plate .....	52
5.2 Coupling probes for the selective excitation of characteristic modes .....	57
5.3 Evaluation of different coupling elements .....	63
5.3.1 Inductive loop and double loop coupling element .....	66
5.3.2 Dipole and T-shape coupling element.....	67
5.3.3 Inverted-L coupling element .....	69
5.3.4 Capacitive feed coupling element .....	69
5.3.5 Loop element including a parasitic capacitive feed capacitance.....	70
5.3.6 Loop element including a capacitive track.....	71
5.3.7 Selection of the elements for the selective excitation of the desired modes .....	71
5.4 Selective capacitive coupling of the characteristic modes by using non-resonant CCEs .....	72
5.5 Selective inductive excitation of the characteristic modes by using non-resonant ICEs.....	75
<b>6. Common Excitation of the Characteristic Modes on Small Handheld Devices ....</b>	<b>81</b>
6.1 Common excitation of modes using capacitive coupling or inductive coupling..	82
6.2 Capacitive coupling by using distributed element pairs.....	86
6.3 Inductive coupling by using distributed element pairs.....	89
6.4 Capacitive excitation of characteristic modes by using off-ground elements .....	93



6.4.1	Small off-ground T-shaped CCE's.....	93
6.4.2	Large off-ground CCE .....	101
<b>7.</b>	<b>Applications on Small Antenna Design .....</b>	<b>115</b>
7.1	3-port antenna design based on a selective inductive excitation.....	116
7.2	Broadband matched hybrid coupling element (HCE) .....	123
7.3	2-port antenna based on a tuned unsymmetrical CCE and a distributed pair of ICEs.....	128
7.4	Multiple-port antenna based on a broadband tuned CCE and self-resonant CFCEs .....	134
<b>8.</b>	<b>Conclusion.....</b>	<b>139</b>
	<b>Bibliography.....</b>	<b>142</b>
	<b>Curriculum Vitae .....</b>	<b>149</b>



## List of Author's Publications and Contributions

The dissertation contains textual materials and figures from the below listed author's publications. The relevant publications are criticized in the text and in the caption of the respective figures by their Roman numerals. The use of those materials requires the permission of *IEEE*.

- I. Martens, R.; Safin, E.; and Manteuffel, D., "Selective excitation of characteristic modes on small terminals," *Antennas and Propagation (EUCAP), Proceedings of the 5th European Conference on, Barcelona, Spain, pp. 2492-2496, 11-15 April 2011.***

The author was responsible of developing the idea and content of the paper. Mr. Safin assisted in calculating the characteristic modes and Prof. Manteuffel supervised the work.

- II. Martens, R.; Safin, E.; and Manteuffel, D., "Inductive and capacitive excitation of the characteristic modes of small terminals," *Antennas and Propagation Conference (LAPC), 2011 Loughborough, Loughborough University, UK, pp. 1-4, 14-15 Nov. 2011.***

The author was responsible of developing the idea and content of the paper. Mr. Safin assisted in calculating the characteristic modes and Prof. Manteuffel supervised the work.

- III. Martens, R. and Manteuffel, D., "A feed network for the selective excitation of specific characteristic modes on small terminals," *Antennas and Propagation (EUCAP), 2012 6th European Conference on, Prague, Czech, pp. 1842-1846, 26-30 March 2012.***

The author was responsible of developing the idea and content of the paper. Prof. Manteuffel supervised the work.

- IV. Martens, R.; Holopainen, J.; Safin, E.; Ilvonen, J.; and Manteuffel, D., "Optimal Dual-Antenna Design in a Small Terminal Multiantenna System," *Antennas and Wireless Propagation Letters, IEEE, Vol.12, pp. 1700-1703, 2013.***

The author had the main responsibility of developing the content for the paper. The original idea was developed by the author and Dr. Holopainen. Dr. Holopainen participated in developing the matching circuit of the distributed elements and in writing the paper. Mr. Safin assisted in the characteristic mode analysis and Mr. Ilvonen assisted in measurements and calculated the envelope correlation out of the measured data. Prof. Manteuffel supervised the work.

- V. Martens, R. and Manteuffel, D., "Systematic design method of a mobile multiple antenna system using the theory of characteristic modes," *Microwaves, Antennas & Propagation, IET, Vol.8, No.12, pp. 887-893, Sept. 16 2014.***

The author had the main responsibility in developing the idea and the content for the paper. Prof. Manteuffel supervised the work.

- VI. Martens, R. and Manteuffel, D., "Mobile LTE-A handset antenna using a hybrid coupling element," *Antennas and Propagation Society International Symposium (APSURSI), 2014 IEEE, Memphis, USA, pp. 1419-1420, 6-11 July 2014.***

The author had the main responsibility in developing the idea and the content for the paper. Prof. Manteuffel supervised the work.

- VII. Chen, Y., Martens, R., Valkonen, R., and Manteuffel, D., "Evaluation of Adaptive Impedance Tuning for Reducing the Form Factor of Handset Antennas", *Antennas and Propagation, IEEE Transactions on*, Vol. 63, No. 2, pp. 703-710, Feb. 2015.**

Mr. Chen had the main responsibility of developing the content for the paper. The original idea was developed by Mr. Chen, the author and Dr. Valkonen. The author participated in developing the non-resonant coupling design and the broadband matched hybrid coupling element, assisted in the measurements and in writing the paper. Dr. Valkonen participated in implementing the adaptive matching circuit design and also assisted in the matching circuitry measurements and had an instructive role in developing the content of the paper. Prof. Manteuffel supervised the work.

- VIII. Martens, R. and Manteuffel, D., "Optimal Placement of PCB-integrated Diversity Elements in a Compact Tunable Handset Antenna," in *Antennas and Propagation (EUCAP), 2015 9th European Conference on.*, Lisbon, Portugal, pp. 1-2, April 2015.**

The author had the main responsibility in developing the idea and the content for the paper. Prof. Manteuffel supervised the work.

In addition, other related publications authored or co-authored by the author of this thesis are given in the reference list as [Mar10\_1, Mar10\_2, Man11\_1, Man11\_2, Man12, Mar12, Had13, Man13, Mar14, Che14, Man16, Mar16].



## Notation Remarks

Through the paper a clear notation is used to clarify the use of equation to the reader. All scalar values are denoted with italic letters. The vectors and matrixes are denoted with bold and capital letters. Any italic subscript letter denotes a count index which is typically used within the summation. The regular subscript is used to specify the quantity.

The entire work assumes a time harmonic dependence of the form  $e^{j\omega t}$  for the electromagnetic field and surface currents. The integral equations are treated in frequency domain only.

## List of Constants

$\mu_0$	permeability of free space [ $4\pi \cdot 10^{-7}$ Vs/Am]
$\epsilon_0$	permittivity of free space [ $8.854 \cdot 10^{-12}$ As/Vm]
$c_0$	speed of light in vacuum [ $2.9979 \cdot 10^8$ m/s]
$Z_{F0}$	characteristic impedance of free space [ $120\pi\Omega \approx 377\Omega$ ]

## List of Latin Symbols

$a_n$	weighting coefficient [ $A\sqrt{\Omega}$ ]
$B_{in}$	characteristic input susceptance of a feeding port [ $\Omega$ ]
$b_n$	normalized coefficient [dimensionless]
$BW$	bandwidth [Hz]
$BW_{rel}$	relative bandwidth potential [dimensionless]
$C$	capacitance [F]
$c^\pm$	centers of the observed triangles $T^\pm$ [m]
$\mathbf{E}$	electric field strength [V/m]
$\mathbf{E}^i$	impressed electric field strength [V/m]
$\mathbf{E}^S$	scattered electric field strength [V/m]
$f$	frequency [Hz]
$\mathbf{f}(\mathbf{r})$	RWG function [dimensionless]
$f_{low}$	lower frequency [Hz]
$f_{res}$	resonance frequency [Hz]
$f_{up}$	upper frequency [Hz]
$G$	Green's function [1/m]
$G_{in}$	characteristic input conductance of a feeding port [ $\Omega$ ]
$\mathbf{H}$	magnetic field strength [A/m]



HP	half power at the eigenresonance of the characteristic mode [W]
$\mathbf{J}$	vector of the surface current density on the surface [A/m]
$j$	imaginary number [dimensionless]
$\mathbf{J}_n$	eigencurrent, eigenvector, characteristic current mode [ $1/\text{m}\sqrt{\Omega}$ ]
$k$	wave number [1/m]
$L$	inductance [H]
$L(\mathbf{J})$	operator (linked $\mathbf{J}$ to $\mathbf{E}^S$ ) [V/m]
$L_{\text{Det}}$	detector inductance [H]
$L_{\text{ESD}}$	electro-static discharge inductance [H]
$L_p$	parallel inductance [H]
$L_s$	series inductance [H]
$l_u$	edge length of the triangles $T^\pm$ [m]
$\mathbf{m}$	electric dipole moment [Am]
$M$	weight operator (diagonalize $Z$ into $\mathbf{J}_n$ ) [ $\Omega\text{m}^2$ ]
$MS_n$	modal significance [dimensionless]
$n$	$n^{\text{th}}$ characteristic current mode [dimensionless]
$\hat{\mathbf{n}}$	unit vector [dimensionless]
$P_{\text{abs,in}}$	absolute power delivered to the antenna [W]
$P_{\text{complex}}$	complex power [W]
$P_{\text{rad}}$	radiation power [W]
$P_{\text{reac}}$	reactive power [W]
$Q_{\text{eig}}$	(eigenvalue) quality factor [dimensionless]
$Q_{\text{rad}}$	(radiation) quality factor [dimensionless]

$\mathbf{r}$	radial coordinate [m]
$R_{\text{in}}$	characteristic input resistance of a feeding port [ $\Omega$ ]
$S^{\infty}$	surface enclosing the whole radiating structure [ $\text{m}^2$ ]
$s_{ij}$	scattering parameters [dimensionless]
$T^{\pm}$	area of the triangles [ $\text{m}^2$ ]
$u$	$u^{\text{th}}$ RWG edge element [dimensionless]
$\mathbf{V}$	excitation vector [Vm]
$V^{\infty}$	volume enclosing the whole radiating structure [ $\text{m}^3$ ]
$V^i$	excitation coefficient [Vm]
$W_{\text{el}}$	time-average electric energy [Ws]
$W_{\text{mag}}$	time-average magnetic energy [Ws]
$W_{\text{net}}$	net stored energy [Ws]
$x, y, z$	cartesian coordinates [m]
$X_{\text{in}}$	input reactance of a feeding port [ $\Omega$ ]
$Y_{\text{in}}$	input admittance of a feeding port [ $\Omega$ ]
$Z$	symmetric complex impedance operator [ $\Omega\text{m}^2$ ]
$Z_0$	reference source impedance [ $\Omega$ ]
$Z_{\text{in}}$	input impedance of a feeding-port [ $\Omega$ ]
$\Delta f$	fractional bandwidth [Hz]

## List of Greek Symbols

$\nabla$	vector differential operator [1/m]
$\delta$	dirac delta function [dimensionless]
$\delta_{nm}$	Kronecker delta [dimensionless]
$\varepsilon$	permittivity [As/Vm]
$\phi$	phase angle [rad]
$\eta_{\text{rad}}$	radiation efficiency [dimensionless]
$\eta_{\text{tot}}$	total efficiency [dimensionless]
$\eta'_{J_n}$	normalized modal power coefficient [dimensionless]
$\eta'$	normalized power coefficient [dimensionless]
$\lambda_n$	modal eigenvalue [dimensionless]
$\mu$	permeability [Vs/Am]
$\rho_{ij}$	cross-correlation [dimensionless]
$\theta$	elevation angle [rad]
$\omega$	angular frequency [1/s]

# List of Abbreviations

3D	Three Dimensional
4G	Fourth Generation
ABC	Absorbing Boundary Condition
ATC	American Technical Ceramics
CCE	Capacitive Coupling Element
CE	Coupling Element
CFCE	Capacitive Feed Coupling Element
CP	Capacitive Probe
Det	Detector
EBG	Electromagnetic Band Gap
EFIE	Electric Field Integration Equations
EM	Electro-Magnetic
EMC	Electro-Magnetic Compatibility
ESD	Electro-Static Discharge
E-UTRA	Evolved UMTS Terrestrial Radio Access
FDTD	Finite-Difference Time-Domain
FF	Form Factor
FN	Feeding Network
FR4	Flame Retardant 4

HB	High-Band
HCE	Hybrid Coupling Element
ICE	Inductive Coupling element
IEEE	Institute of Electrical and Electronic Engineers
IP	Inductive Probe
LB	Low-Band
Li-Ion	Lithium Ion
LTE	Long Term Evolution
LTE-A	Long Term Evolution - Advanced
MIMO	Multiple Input Multiple Output
MN	Matching Network
MoM	Method of Moments
OB	Operation Band
PCB	Printed Circuit Board
PD	Power Divider
PEC	Perfectly Electric Conductivity
PS	Phase Shifter
RF	Radio Frequency
RFM	Radio Frequency Module
RWG	Rao Wilton Glisson
TCM	Theory of Characteristic Modes
UMTS	Universal Mobile Telecommunications System
WE	Würth Elektronik



# Chapter 1

## Introduction

### 1.1 Background

The demand for high speed communications in the wireless standards such as LTE, LTE-Advanced, IEEE 802.16 (WiMAX) and IEEE 802.11 increases the demand of efficient antenna systems, both, on the mobile and the base station side of the radio access network [SHe08, Vau87, Li10, Man16]. Importantly, many of these standards may be required to operate simultaneously. Especially the design of broadband and multiple antennas in mobile (cellular) radio handsets becomes quite challenging due to the physical limitations. These limitations are related to the form factor, i.e. the shape and size of the mobile handset [Van02, Lop04, Stu07, Bes06]. On the other hand, the space occupied by the antenna systems tends to decrease due to the demand of computer-like handheld devices. Especially in this content, the consumer wants to have a thin device with a large display, low power consumption and a good camera technology which determine mainly the thickness of the casing. In contrast, all of these needs restrict the available volume and location of the antenna or multiple antenna system drastically.

For the realization of the desired high data rates, for example, the long term evolution (LTE) and the IEEE 802.11n standards require the integration of multiple antenna systems to enable a multiple-input–multiple-output (MIMO) technology in mobile terminals. In order to address the associated sub-channels de-correlated antenna elements need to be integrated into the small terminal device with a tight form-factor [GCa08, Shu13, Zha13, Mie13]. For reducing the mutual coupling between closely spaced antenna elements the

use of electromagnetic band gap (EBG) structures or suspended lines is reported in literature [Yan06, Dia06]. The authors in [Kar04] propose to modify the shape and/or insert some slits in the printed circuit board (PCB) between two antenna elements in order to achieve a significant reduction of mutual coupling within the operating frequency band. Such modifications of the PCB are unlikely possible in practical applications.

Typically, in small terminal applications the antenna concept is chosen such that it uses the chassis of the terminal as a counterpoise for the antenna element. In [Van02] it has already been proven that the most effective antenna is the metallic chassis of the mobile terminal itself, including the PCB and EMC (Electro-Magnetic Compatibility) shieldings etc. Consequently, results in [Man11\_2, Mar10\_1, Mar10\_2] show that the correlation of two elements is significantly affected by the electrical size of the chassis and the location of the elements on the chassis. All of these effects can be utilized to excite chassis modes in a specific way, enabling a multi-port or broadband antenna system. This thesis concentrates on the design of such antennas.

### 1.2 Objective of this work

This thesis gives a physical insight into the design of multiple and broadband antennas for mobile terminals based on the TCM (Theory of the Characteristic Modes). The main objective shows that the theory helps to understand how characteristic modes behave. In addition, it shows how this knowledge can efficiently be used for the controlling of the dimensions of the terminal or the mode coupling mechanism.

Main issues in this thesis are the following:

- Determination of the modal parameters based on the TCM.
- Determination of an evaluation parameter in order to find the optimal excitation and location of the given modes to control the impedance matching and radiation.
- Determination of the chassis modes on small mobile terminals.
- Systematic study of the selective mode excitation and their required coupling mechanism on small mobile terminals.
- Systematic study of the common mode excitation and their required coupling mechanism on small mobile terminals.



- Analysis and evaluation of non- and self-resonant coupling structures for the optimal selective and common mode coupling.
- Analysis of the influence of the capacitive coupling element shapes and their self-resonances on the absolute power delivered to the antenna and the bandwidth potential.
- Systematic application of the inductive, capacitive and their hybrid coupling elements for broadband and MIMO antenna systems.

### **1.3 Contents and organization of the thesis**

In this thesis compact antennas are studied based on the systematic analysis of the characteristic modes on a mobile terminal. The specific excitation of the modes and the power contribution of the modes related to the radiated power are in focus. The experimental studies in this thesis are based on the electromagnetic (EM) field and circuit simulations. Prototyping and measurements underline the simulation results. The main scientific contributions of the thesis are presented in the publications [I-VIII]. The thesis collects all of the results providing additional references to other relevant scientific research made in the related field.

Chapter 2 shows a review of the TCM and its related parameters in order to bring insight into the radiation phenomenon of radiating structures (e.g. small terminal). This chapter can be seen as introduction of the theory to better understand and deal with radiated and scattered electromagnetic fields.

A review of the RWG (Rao Wilton Glisson) edge elements is shown in chapter 2. It shows how the radiation structure can be excited and how that is related to the TCM parameters. Different parameters, like the modal admittance, impedance and power, will be determined.

The eigenvalues, the modal significances, the radiating bandwidths and the quality factor of the first two modes of a generic PEC (Perfectly Electric Conductive) strip are studied in chapter 3. The width and the length of the PEC strip are used to show how this affects the derived modal parameters. In addition, a simple planar dipole antenna is analyzed to understand how the structure and the feeding mechanism affects the radiated power, the

absolute power delivered to the antenna and the matching. A normalized power coefficient and its modal decomposition are derived based on the parameters of the TCM. This new parameter will be used to evaluate efficient coupling concepts for small mobile terminals.

Chapter 5 studies the selective excitation of desired modes on the small mobile platform by using the terminal itself as an antenna. It shows the advantages and disadvantages of the selective inductive and capacitive excitation [I, II, IV]. A detailed characteristic mode analysis shows which modes are excited and which are not excited [V]. A preliminary study of different non-matched coupling elements have shown which elements are able to excite the modes selectively without contributing too much to the radiation [III]. The last sections of this chapter evaluate the realistic implementations of the non-resonant coupling structures distributed in optimal locations with respect to the desired modes. This implementation study can be utilized to optimize the antenna performance (bandwidth potential, radiated power, absolute power delivered to the antenna etc.) in different operation frequencies [IV, V].

By a contrast, chapter 6 studies the excitation of multiple modes with the same exciter on the small mobile platform [VI, VII, VIII]. It shows the advantages and disadvantages of the common excitation of multiple characteristic modes. A preliminary characteristic mode analysis shows which multiple modes can be excited and which modes cannot be excited [V]. A detailed study of off-ground capacitive coupling elements (CCEs) shows how the structure and the location of the feeding point can be utilized to optimize the single antenna performance (bandwidth potential, radiated power, absolute power delivered to the antenna etc.) [VI, VII, VIII]. It shows how the behavior of the characteristic modes and the CCE resonances can be used to design an efficient dual-broadband CCE antenna.

Different applications of the small antenna design based on the efficient coupling concepts are presented in chapter 7. The selective inductive excitation can be used to design an efficient multiple antenna system by using three pairs of ICEs (Inductive Coupling Elements) or is used to implement one pair of ICEs (second antenna) in a given CCE antenna design [I, II, III, IV, V]. Another small antenna design concept shows the modified antenna geometry of a CCE antenna in order to achieve a broadband matched system by exciting several modes [VI, VII]. The optimal location of self-resonant diversity elements based on

the given CCE antenna is also discussed and addressed in [VII, VIII].

## 1.4 Main scientific merits

The scientific results obtained in this thesis are related to different methods of the optimal characteristic mode coupling. Both the selective and the common excitation of different modes are discussed by different coupling concepts and compared to each other. In addition, different implemented broadband and/or multiple antenna prototypes are developed. Each of them exhibiting e.g. a high EM isolation, an optimal broadband matching, an efficient broadband potential, a high total efficiency in the field of handset antennas in general. Regarding the contribution of the thesis to the scientific antenna design community, the highlights of the thesis can be summarized in following points:

1. A new normalized power coefficient is derived and consists of the absolute power delivered to the antenna related to the radiated power of the system. The modal components of the normalized coefficient can be used for the evaluation of the percentage power contribution of the excited modes. It contains the excitation and the eigenvalues of the characteristic modes and the matching of the entire antenna system. This decomposition provide physical background of the antenna system and helps to understand how the system works.
2. A systematic analysis and evaluation of the selective excitation of the characteristic modes on a small terminal is shown. Both the inductive and the capacitive excitation concepts are compared to each other. Different unmatched coupling elements are evaluated and implemented for the desired mode excitation. The inductive coupling shows clearly better performance with respect to the selective excitation of the modes over the observed frequency range.
3. A systematic analysis and evaluation of the common excitation of the characteristic modes on the small terminal is shown. Both the inductive and the capacitive excitation concepts are compared to each other. The capacitive coupling shows clearly better performance with respect to the common excitation of the modes over the observed frequency range.

4. A design strategy of a 3-port antenna system based on the selective excitation of first three orthogonal chassis modes is derived and evaluated. This provides a simple and easy method to design an efficient multiple antenna structure and can be extended easily to more antenna ports.
5. A broadband-antenna structure design for small mobile terminals is evaluated. It combines an unsymmetrical CCE (Capacitive Coupling Element) with an additional inductive loop track and can be seen as a HCE (Hybrid Coupling Element). This antenna is designed in such a way that it excites all available modes of the structure. It operates with a measured efficiency of  $\eta_{\text{total}} \geq 50\%$  across the low frequency range 0.69GHz - 0.96GHz and a measured efficiency of  $\eta_{\text{total}} \geq 75\%$  across the higher frequencies 1.71GHz - 2.60GHz.
6. A multi-antenna structure design consisting of a main antenna and a diversity antenna is designed. The frequency reconfigurable main antenna operates at the low band (here: 0.69GHz - 0.96GHz) and the high band (1.71GHz - 2.60GHz). A characteristic mode analysis of the main antenna shows which modes are excited and which are less excited. The second antenna consisting of two distributed ICEs (Inductive Coupling Elements) is designed to excite modes with low contribution of the main antenna at the frequency range of 2.5GHz - 2.7GHz. The concept shows an EM-isolation of  $|S_{ij}| \geq 30\text{dB}$ , an efficiency of both antennas of  $\eta_{\text{total}} \geq 60\%$  and an envelope correlation of 3D radiation pattern of  $|\rho_{ij}| \leq 0.064$  at the operating frequency 2.6GHz.

A non-matched CCE antenna (main antenna) which is tunable and can be broadband matched to any E-UTRA band up to 2.7GHz is designed. A systematic application of the TCM helped to find out the optimal locations of self-resonant diversity elements based on the given location of the main antenna on the same terminal. The novel systematic design strategy is based on avoiding excitation of those characteristic modes, which are excited by the broadband CCE antenna. The optimal locations of both CFCEs (Capacitive Feed Coupling Elements) yield a high EM isolation of  $|S_{ij}| \geq 21\text{dB}$  in the E-UTRA bands 2 and 7.

# Chapter 2

## The Theory of Characteristic Modes

The TCM (Theory of Characteristic Modes) was first developed and published by Garbacz in 1968 [Gar68] and extended in 1971 [Gar71] as a tool to better understand and deal with radiated and scattered electromagnetic fields. The entire theory was refined in 1971 by Harrington and Mautz [Har68, Har71\_1, Har71\_2] and further applied to topics such as controlling of radar scattering [Har72], pattern synthesis for antenna arrays [Mau73] and reactively loaded aperture antenna arrays [Luz78].

The aim of this chapter is to provide an introduction and review of the TCM in order to bring physical insight into the radiating phenomena of any arbitrarily-shaped structures. It shows how the TCM can be used to analyze and enhance the radiation performance of a given radiating structure. The quantities derived in this chapter will be utilized in the later chapters 4 - 7 to design antennas by providing independent control of those characteristic modes.

### 2.1 The impedance operator and the generalized eigenvalue problem

The theory of the characteristic modes is derived over the scattering problem of a perfectly conducting body, defined by a surface  $S$ , illuminated by an electric field  $\mathbf{E}^i$  [Har68, Har71\_1, Har71\_2]. Fig. 2-1 (left) shows an arbitrary surface  $S$  with respect to the cartesian coordinate system  $(x, y, z)$  and the spherical coordinate system  $(r, \theta, \varphi)$ .

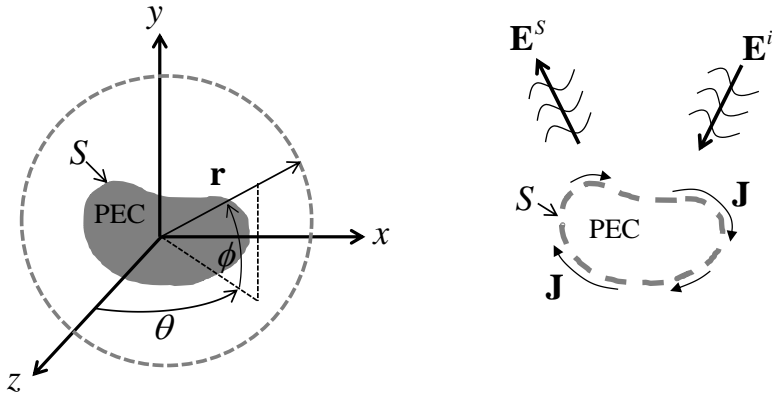


**Fig. 2-1** The perfectly electric conducting (PEC) body of the original problem (left) and the equivalent surface problem (right).

Fig. 2-1 (right) represents the perfectly conducting body in an impressed field  $\mathbf{E}^i$  produced by external source. The surface current  $\mathbf{J}$  is induced on the surface  $S$ , producing a scattered field  $\mathbf{E}^s$ . This scattered field can be found in terms of  $\mathbf{J}$  by the integral method:

$$\mathbf{E}^s = \frac{1}{j\omega\epsilon} \iiint_V \mathbf{J}(\mathbf{r}') \cdot (\nabla' \nabla' + k^2) G(\mathbf{r}, \mathbf{r}') dv. \quad (2.1)$$

The surface current density  $\mathbf{J}$  has the unit [A/m] and the electric field has the unit [V/m]. In (2.1), the volume integral is evaluated over an enclosure of the scatterer. The  $\omega$  is the angular frequency [1/s],  $\epsilon$  is the permittivity [As/Vm],  $k$  the wave number [1/m] and  $\nabla$  is the vector differential operator [1/m].  $G(\mathbf{r}, \mathbf{r}')$  denotes the Green's function at the point of observation.

According to the boundary condition on the perfectly conducting surface

$$\hat{\mathbf{n}} \times \mathbf{E}^s = \hat{\mathbf{n}} \times \mathbf{E}^i \quad (2.2)$$

the tangential component of the electrical fields vanishes

$$\left[ \mathbf{E}^i + \mathbf{E}^s \right]_{\tan} = 0 \quad (2.3)$$

on the surface  $S$ .

Defining the operator [Har68]

$$[L(\mathbf{J})]_{\text{tan}} = [\mathbf{E}^i]_{\text{tan}} \quad (2.4)$$

the scattering formulation can be written as

$$L(\mathbf{J}) = -\mathbf{E}^s \quad (2.5)$$

where the  $[\ ]_{\text{tan}}$  means the tangential components of the bracketed quantity on  $S$ . The linear operator  $L$  links the surface current density  $\mathbf{J}$  to the electric field and is defined in the frequency domain [Har71\_2] and has the unit [V/m].

The general eigenvalue equation of the characteristic mode analysis is formulated

$$\mathbf{Z}\mathbf{J}_n = \nu_n \mathbf{M}\mathbf{J}_n. \quad (2.6)$$

where  $\nu_n = 1 + j\lambda_n$  and  $\mathbf{J}_n$  denote the eigenfunctions.  $\mathbf{Z}$  denotes a symmetric complex operator and is direct related to the eigenfunctions.

The weight operator  $\mathbf{M}$  diagonalizes  $\mathbf{Z}$  into eigenfunctions  $\mathbf{J}_n$ . If  $\mathbf{M} = \mathbf{R}$  is chosen, the eigenfunctions become orthogonal to each other and we obtain:

$$\begin{aligned} \mathbf{R}\mathbf{J}_n + j\mathbf{X}\mathbf{J}_n &= \nu_n \mathbf{R}\mathbf{J}_n, \\ \mathbf{R}\mathbf{J}_n + j\mathbf{X}\mathbf{J}_n &= (1 + j\lambda_n) \mathbf{R}\mathbf{J}_n, \\ \mathbf{X}\mathbf{J}_n &= \lambda_n \mathbf{R}\mathbf{J}_n. \end{aligned} \quad (2.7)$$

Based on the real symmetric operators  $\mathbf{R}\mathbf{J}_n$  and  $\mathbf{X}\mathbf{J}_n$ , all eigenvalues  $\lambda_n$  and eigenfunctions  $\mathbf{J}_n$  are consequently real as well.

## 2.2 Orthogonal properties of the characteristic modes

Based on the definition in [Har71\_1], the eigenfunctions  $\mathbf{J}_n$  shall be called *characteristic modes* or *eigencurrents* of the conducting body. Each of them is normalized to radiate a unit power.

$$P_{\text{rad},n} = \frac{1}{2} \langle \mathbf{J}_n^*, \mathbf{R}\mathbf{J}_n \rangle = \frac{1}{2} \iint \mathbf{J}_n^* \cdot \mathbf{R}\mathbf{J}_n dS = 1 \quad (2.8)$$

We recognize in the same manner the orthogonality of all characteristic modes with the

## 2. The Theory of Characteristic Modes

---

given normalization. For the definition of the orthogonal property we generalize the orthogonality relationships for all index values  $m$  and  $n$  as follows:

$$\frac{1}{2} \langle \mathbf{J}_m^*, \mathbf{R}\mathbf{J}_n \rangle = \frac{1}{2} \oint \mathbf{J}_m^* \cdot \mathbf{R}\mathbf{J}_n dS = \delta_{mn}, \quad (2.9)$$

$$\frac{1}{2} \langle \mathbf{J}_m^*, \mathbf{X}\mathbf{J}_n \rangle = \frac{1}{2} \oint \mathbf{J}_m^* \cdot \mathbf{X}\mathbf{J}_n dS = \lambda_n \delta_{mn}, \quad (2.10)$$

$$\frac{1}{2} \langle \mathbf{J}_m^*, \mathbf{Z}\mathbf{J}_n \rangle = \frac{1}{2} \oint \mathbf{J}_m^* \cdot \mathbf{Z}\mathbf{J}_n dS = (1 + j\lambda_n) \delta_{mn} = \nu_n \delta_{mn}, \quad (2.11)$$

where the  $\delta_{mn}$  denotes the Kronecker delta

$$\delta_{mn} = \begin{cases} 1 & \text{if } m = n \\ 0 & \text{if } m \neq n \end{cases}. \quad (2.12)$$

In this thesis the characteristic modes are assumed to be normalized.

### 2.3 Orthogonal properties of the modal eigenfields

The complex power  $P_{\text{complex}}$  for any modal current  $\mathbf{J}$  on the surface  $S$  can be expressed by the complex Poynting theorem as follows [Bal89]:

$$P_{\text{complex}} = \underbrace{\frac{1}{2} \oint_{S^\infty} (\mathbf{E} \times \mathbf{H}^*) \cdot d\mathbf{S}}_{\text{radiated power in [W]}} + j\omega \underbrace{\frac{1}{2} \iiint_V (\mu |\mathbf{H}|^2 - \varepsilon |\mathbf{E}|^2) dV}_{\text{reactive power in [W]}} \quad (2.13)$$

$S^\infty$  and  $V^\infty$  denote the surface and the volume enclosing the whole structure.

The complex power  $P_{\text{complex},n}$  for the  $n^{\text{th}}$  characteristic mode  $\mathbf{J}_n$  on the surface  $S$  can be equivalently expressed as follows:



$$\begin{aligned}
 P_{\text{complex},n} &= \underbrace{\frac{1}{2} \oiint_{S^\infty} (\mathbf{E}_m \times \mathbf{H}_n^*) \cdot d\mathbf{S}}_{\text{radiated power} = \delta_{mn}} \\
 &+ j\omega \underbrace{\frac{1}{2} \left( \iiint_V (\mu \mathbf{H}_m \cdot \mathbf{H}_n^*) dV - \iiint_V (\varepsilon \mathbf{E}_m \cdot \mathbf{E}_n^*) dV \right)}_{\text{stored magnetic energy } W_{\text{mag},n} \text{ and electric energy } W_{\text{el},n} = \frac{\lambda_n}{\omega} \delta_{mn}} \\
 &= (1 + j\lambda_n) \delta_{mn}.
 \end{aligned} \tag{2.14}$$

In the far field,  $\mathbf{E}_n$  and  $\mathbf{H}_n$  are orthogonal to each other on the direction of propagation

$$\mathbf{E}_n = Z_{F0} \mathbf{H}_n \times \hat{\mathbf{n}}, \tag{2.15}$$

$$\mathbf{H}_n = \frac{1}{Z_{F0}} \hat{\mathbf{n}} \times \mathbf{E}_n. \tag{2.16}$$

$Z_{F0}$  denotes the characteristic impedance of free space with the unit  $[\Omega]$ . Adding the radiating power in (2.13) to its complex conjugate with the index values  $m$  and  $n$  leads to the following two expressions

$$\frac{1}{2Z_{F0}} \oiint_{S^\infty} \mathbf{E}_m \cdot \mathbf{E}_n^* dS = \delta_{mn}, \tag{2.17}$$

$$\frac{Z_{F0}}{2} \oiint_{S^\infty} \mathbf{H}_m \cdot \mathbf{H}_n^* dS = \delta_{mn}, \tag{2.18}$$

and shows directly the orthogonal property of the eigenfields.

Due to the general orthogonal relationship in (2.9) – (2.11), which associate the complex power with the  $m^{\text{th}}$  an  $n^{\text{th}}$  eigencurrent the expression in (2.14) can be similarly expressed as decomposition of the complex power:

$$\begin{aligned}
 P_{\text{complex},n} &= \frac{1}{2} \langle \mathbf{J}_m^*, Z\mathbf{J}_n \rangle = \frac{1}{2} \langle \mathbf{J}_m^*, R\mathbf{J}_n \rangle + j \frac{1}{2} \langle \mathbf{J}_m^*, X\mathbf{J}_n \rangle \\
 &= P_{\text{rad},n} + jP_{\text{react},n}
 \end{aligned} \tag{2.19}$$

in its related real and reactive power.

## 2.4 Modal field energies and eigenvalues

The previous section showed that the characteristic electric and magnetic far fields are orthogonal to each other which also imply the orthogonality of the eigenfields itself. If we evaluate the reactive part of the complex Poynting theorem in (2.14) in order to redefine the time-avarage electric energy  $W_{\text{el},n}$  [Ws] and magnetic energy  $W_{\text{mag},n}$  [Ws], the net stored energy  $W_{\text{net},n}$  of each mode can be obtained [Bal89]:

$$\begin{aligned}
 P_{\text{reac},n} &= \omega \frac{1}{2} \left( \underbrace{\iiint_V (\mu \mathbf{H}_m \cdot \mathbf{H}_n^*) dV - \iiint_V (\varepsilon \mathbf{E}_m \cdot \mathbf{E}_n^*) dV}_{\text{net stored energy} = \bar{W}_{\text{net},n} = \frac{\lambda_n}{\omega} \delta_{mn}} \right) = \lambda_n \delta_{mn} \\
 &= \omega W_{\text{net},n} = \lambda_n \quad ; \text{ for } m = n
 \end{aligned} \tag{2.20}$$

This redefined expression allows an interpretation of the relevant modal quantities, which is based on the relation of the reactive power  $P_{\text{reac},n}$  to the radiated power  $P_{\text{rad},n}$

$$\lambda_n = \frac{\omega W_{\text{net},n}}{P_{\text{rad},n}} = \frac{2\omega (W_{\text{mag},n} - W_{\text{el},n})}{P_{\text{rad},n}} = \frac{P_{\text{reac},n}}{P_{\text{rad},n}} = \frac{\frac{1}{2} \langle \mathbf{J}_n^*, \mathbf{XJ}_n \rangle}{\frac{1}{2} \langle \mathbf{J}_n^*, \mathbf{RJ}_n \rangle}. \tag{2.21}$$

Here, the eigenvalue of a characteristic mode can be used for a physical interpretation, as shown in (2.22).

$$\lambda_n \begin{cases} > 0 & \text{inductive eigencurrent} \\ < 0 & \text{capacitive eigencurrent} \\ = 0 & \text{externally resonant eigencurrent} \\ \rightarrow \pm \infty & \text{internally resonant eigencurrent} \end{cases} \tag{2.22}$$

So called *inductive modes* predominantly store magnetic energy, whereas so called *capacitive modes* predominantly store electric energy. A zero of the eigenvalue indicates an external resonance of the respective modes, which means that no net-energy will be stored in the near field ( $W_{\text{net},n} = 0$ ). If the eigenvalue of the related characteristic mode approaches infinity, the structure does not radiate anymore.

## 2.5 Modal solution of the characteristic modes and characteristic fields

The current  $\mathbf{J}$  induced on the specific surface can be defined as linear superposition of the characteristic modes  $\mathbf{J}_n$

$$\mathbf{J} = \sum_{n=1}^N a_n \mathbf{J}_n, \quad (2.23)$$

where  $a_n$  denote the  $n^{\text{th}}$  modal weighting coefficient. Due to the normalization in (2.8) the weighting coefficient has the unit  $[A\sqrt{\Omega}]$  and the unit of the characteristic modes is given by  $[1/m\sqrt{\Omega}]$ .

These coefficients can be determined by substituting (2.23) into the operator formulation (2.4). Based on the linearity of the operator  $L$  (2.23) can then be extended into

$$L\left(\sum_{n=0}^N a_n \mathbf{J}_n\right) = [\mathbf{E}^i]_{\text{tan}}. \quad (2.24)$$

Therefore, by using the linear operator which is combined with the conjugate complex eigencurrent  $\mathbf{J}_m^*$  the equation (2.24) can be set to [Har68]

$$\sum_{n=0}^N a_n \langle \mathbf{J}_m^*, \mathbf{Z}\mathbf{J}_n \rangle - \langle \mathbf{J}_m^*, \mathbf{E}_{\text{tan}}^i \rangle = 0 \quad \text{with } m = 1, 2, \dots \quad (2.25)$$

Based on the definition of the orthogonal property in (2.9) – (2.11) we generalize (2.25) to

$$2a_n (1 + j\lambda_n) = \langle \mathbf{J}_n^*, \mathbf{E}_{\text{tan}}^i \rangle \quad \text{with } m = n \quad (2.26)$$

and obtain the modal excitation coefficient

$$V_n^i = \langle \mathbf{J}_n^*, \mathbf{E}_{\text{tan}}^i \rangle = \oiint_S \mathbf{J}_n^* \cdot \mathbf{E}_{\text{tan}}^i ds. \quad (2.27)$$

This excitation coefficient indicates the degree of coupling between tangentially excited electric fields and the  $n^{\text{th}}$  characteristic mode.

## 2. The Theory of Characteristic Modes

---

Furthermore, if we summarize the expressions (2.26) and (2.27) we obtain the weighting coefficient depending on the excitation coefficient and the respective eigenvalue of the  $n^{\text{th}}$  characteristic mode

$$a_n = \frac{\langle \mathbf{J}_n^*, \mathbf{E}_{\text{tan}}^i \rangle}{2(1 + j\lambda_n)} = \frac{V_n^i}{2(1 + j\lambda_n)} . \quad (2.28)$$

It can be interpreted so that for maximizing the  $n^{\text{th}}$  weighting coefficient the excitation coefficient should be maximized, whereas the term  $(1+j\lambda_n)$  should be minimized. This means that the eigenvalue  $\lambda_n$  of the  $n^{\text{th}}$  characteristic mode must be close to zero (close to its own resonance).

If we substitute the  $a_n$  into (2.26) the modal solution for the current  $\mathbf{J}$  on the surface  $S$  can be obtained

$$\mathbf{J} = \sum_{n=1}^N \frac{\langle \mathbf{J}_n^*, \mathbf{E}_{\text{tan}}^i \rangle}{2(1 + j\lambda_n)} \mathbf{J}_n = \sum_{n=1}^N \frac{V_n^i}{2(1 + j\lambda_n)} \mathbf{J}_n . \quad (2.29)$$

The fields are linearly related to the currents as shown in [Har71\_1]. Therefore, the fields can also be expressed as a linear superposition

$$\mathbf{E} = \sum_{n=1}^N \frac{V_n^i}{2(1 + j\lambda_n)} \mathbf{E}_n , \quad (2.30)$$

$$\mathbf{H} = \sum_{n=1}^N \frac{V_n^i}{2(1 + j\lambda_n)} \mathbf{H}_n . \quad (2.31)$$

### 2.6 Modal solution of the complex power

The total radiated power can be calculated by using the real part of the expression (2.11). Therefore, the radiated power reduces to the summation of the squared weighting coefficients of the characteristic modes:

$$\begin{aligned}
 P_{\text{rad}} &= \text{Re} \left\{ \frac{1}{2} \langle \mathbf{J}^*, \mathbf{ZJ} \rangle \right\} \\
 &= \text{Re} \left\{ \frac{1}{2} \left\langle \sum_{m=1}^M a_m^* \mathbf{J}_m^*, \mathbf{Z} \left( \sum_{n=1}^N a_n \mathbf{J}_n \right) \right\rangle \right\} \\
 &= \text{Re} \left\{ \sum_{m=1}^M a_m^* \sum_{n=1}^N a_n \frac{1}{2} \langle \mathbf{J}_m^*, \mathbf{ZJ}_n \rangle \right\}_{m=n} \quad (2.32) \\
 &= \text{Re} \left\{ \sum_{n=1}^N |a_n|^2 (1 + j\lambda_n) \right\} \\
 &= \sum_{n=1}^N |a_n|^2 = \sum_{n=1}^N P_{\text{rad},n}
 \end{aligned}$$

Based on this expression the individual contribution of the  $n^{\text{th}}$  characteristic mode can be expressed as

$$P_{\text{rad},n} = |a_n|^2 = \left| \frac{V_n^i}{2(1 + j\lambda_n)} \right|^2 \quad (2.33)$$

which shows the direct relation of the excitation coefficient and the respective eigenvalue to the radiated power. This expression plays a dominant role for the design of antennas based on characteristic modes and will be further used in this thesis.

In terms of the reactive power the imaginary part of the expression (2.11) must be used:

$$\begin{aligned}
 P_{\text{reac}} &= \text{Im} \left\{ \frac{1}{2} \langle \mathbf{J}^*, \mathbf{ZJ} \rangle \right\} \\
 &= \sum_{n=1}^N |a_n|^2 \lambda_n = \sum_{n=1}^N P_{\text{reac},n}. \quad (2.34)
 \end{aligned}$$

where the individual contribution of each characteristic mode can be separated to:

$$P_{\text{reac},n} = |a_n|^2 \lambda_n = \left| \frac{V_n^i}{2(1 + j\lambda_n)} \right|^2 \lambda_n. \quad (2.35)$$

It shows that the reactive power of each modes can be expressed as the squared weighting

## 2. The Theory of Characteristic Modes

---

coefficient multiplied by the eigenvalue of the respective characteristic modes itself. Compared to the radiated power the reactive power is directly related to the non-squared eigenvalue, which results in an additional contribution to the energies of each mode.

The summation of the complex power of all modes and the complex power of each characteristic mode are shown in the expressions

$$\begin{aligned} P_{\text{complex}} &= \sum_{n=1}^N P_{\text{complex},n} \\ &= \sum_{n=1}^N |a_n|^2 (1 + j\lambda_n) \\ &= \frac{1}{4} \sum_{n=1}^N \left| \frac{V_n^i}{(1 + j\lambda_n)} \right|^2 (1 + j\lambda_n). \end{aligned} \tag{2.36}$$

The derived contributions of the  $n^{\text{th}}$  characteristic mode to the radiated and reactive power will be used in section 3.4 and section 4.3.1 to derive a new normalized power coefficient of radiated structures.

# Chapter 3

## The RWG Edge Elements and its Relation to the TCM

In order to calculate a surface problem (Fig. 2-1) in a simple and efficient numerical procedure the Method of Moment (MoM) can be used [Har69]. The MoM solves the electric field integral equations (EFIE) by discretizing the domain in which the solvable quantity is defined [Mark02, Har69]. In our case the unknown quantity is the surface current which results from the incident field (see Fig. 2-1) or from a source defined somewhere on the surface itself (see Fig. 3-3). In order to solve such electromagnetic problems expansion functions are needed to discretize the entire domain. Triangular patch expansion functions are used based on the surface-type problems in this thesis. Such functions are known as RWG (Rao-Wilton-Glissson) edge elements [RWG82, Mark02].

The aim of this chapter is to provide a review of the RWG edge elements. It will introduce how a radiating structure can be excited by an external source (incident field) or how an internal source is defined on the surface  $S$  and how that is related to the TCM. Different quantities such as the input impedance or admittance and the modal power will be determined based on the RWG edge elements.

### 3.1 RWG edge elements

The current density  $\mathbf{J}$  on the surface  $S$  of a PEC structure can be calculated by the expansion of RWG edge elements [RWG82].

### 3. The RWG Edge Elements and its Relation to the TCM

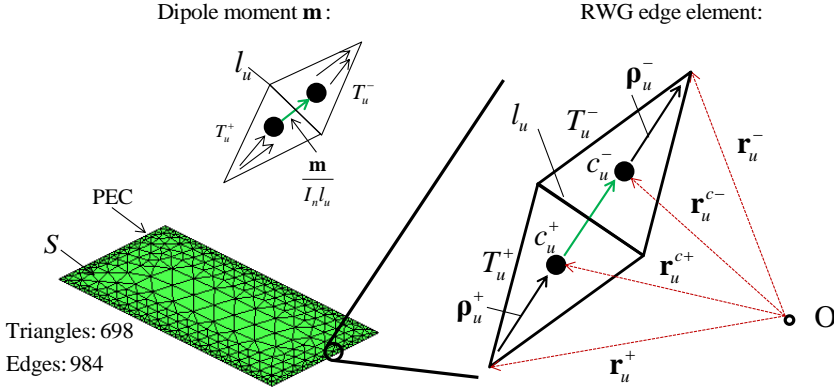


**Fig. 3-1** Equivalent surface problem, here a rectangular plate, is expanded by RWG edge elements.

As an example, a rectangular plate is divided into 698 triangles as shown in Fig. 3-1. Each pair of adjacent triangles  $T_u$  have a common edge  $l_u$  and constitute the corresponding  $u^{\text{th}}$  RWG edge element [Mark02]. The triangular patch expansion functions are defined as

$$\mathbf{f}_u(\mathbf{r}) = \begin{cases} \frac{l_u}{2A_u^+} \boldsymbol{\rho}_u^+(\mathbf{r}), & \mathbf{r}_u \text{ in } T_u^+ \\ \frac{l_u}{2A_u^-} \boldsymbol{\rho}_u^-(\mathbf{r}), & \mathbf{r}_u \text{ in } T_u^- \\ 0, & \text{otherwise} \end{cases} \quad (3.1)$$

One of the triangles  $T_u^\pm$  has a plus and the other a minus sign, which are directly related to the vectors  $\boldsymbol{\rho}_u^\pm$  (see Fig. 3-1). Furthermore,  $l_u$  and  $A_u^\pm$  denote the edge length and the area of the triangles  $T_u^\pm$  of the respective RWG edge element. Each element corresponds directly to a finite electric dipole, also called dipole moment

$$\mathbf{m} = \int_{T_u^+ + T_u^-} I_u \mathbf{f}_u(\mathbf{r}_u) dS = I_u l_u (\mathbf{r}_u^{c-} - \mathbf{r}_u^{c+}), \quad (3.2)$$

where  $c^\pm$  denotes the centers of the observed triangles  $T_u^\pm$ . Based on the division of the rectangular plate into RWG edge elements, the sum of each elementary dipole current corresponds directly to the surface current  $\mathbf{J}$ . Therefore, the calculation of the current density  $\mathbf{J}$  on the surface  $S$  of the PEC structure can then be expressed as a sum of all RWG edge elements with the unknown weighting expansion coefficient  $I_u$  [Mark02]:



$$\mathbf{J}(\mathbf{r}) = \sum_{u=1}^U I_u \mathbf{f}_u(\mathbf{r}) \cdot \quad (3.3)$$

The weighting expansion coefficients  $I_u$  are the elements of the moment equation and can be expressed as a linear system of equations in form of the vector  $\mathbf{I}$ . The product  $I_u \mathbf{f}_u$  is associated with the current of the dipole moment at the  $u^{\text{th}}$  edge element  $l_u$ , whereas the length of the finite dipole is given by  $|\mathbf{r}_u^{c-} - \mathbf{r}_u^{c+}|$  as shown in Fig. 3-1 and in (3.2).

In the far field the following relation of the total electric and magnetic field at any point  $\mathbf{r}$  can be obtained as the sum over all elements [Mark02]:

$$\mathbf{E}(\mathbf{r}) = \sum_{u=1}^U \mathbf{E}_u \left( \mathbf{r} - \frac{1}{2} (\mathbf{r}_u^{c+} + \mathbf{r}_u^{c-}) \right), \quad (3.4)$$

$$\mathbf{H}(\mathbf{r}) = \sum_{u=1}^U \mathbf{H}_u \left( \mathbf{r} - \frac{1}{2} (\mathbf{r}_u^{c+} + \mathbf{r}_u^{c-}) \right). \quad (3.5)$$

### 3.2 Modal excitation concepts

We assume a scattering problem, here defined by a perfectly conducting plate illuminated by the electric field  $\mathbf{E}^i$  as shown in Fig. 3-2. The tangential component of the incident electric field can be expressed as an equivalent voltage excitation  $V_u^i$  over each  $u^{\text{th}}$  edge element on the discretized surface  $S$  [Mark02].

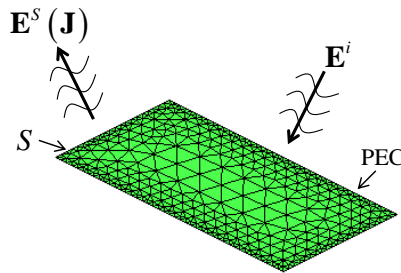


**Fig. 3-2** Equivalent surface problem, here a rectangular plate, illuminated by the electric field.

Based on this problem the equivalent voltage excitations  $V_u^i$  over each  $u^{\text{th}}$  edge element is defined as

### 3. The RWG Edge Elements and its Relation to the TCM

$$\begin{aligned} \langle \mathbf{f}_u, \mathbf{E}^{i,c_u^\pm} \rangle &= \iint_{T_u^+} \mathbf{E}^{i,c_u^+} \cdot \frac{l_u}{2A_u^+} \boldsymbol{\rho}_u^{c_u^+}(\mathbf{r}_u) dA + \iint_{T_u^-} \mathbf{E}^{i,c_u^-} \cdot \frac{l_u}{2A_u^-} \boldsymbol{\rho}_u^{c_u^-}(\mathbf{r}_u) dA \\ \langle \mathbf{f}_u, \mathbf{E}^{i,c_u^\pm} \rangle &= \frac{l_u}{2} \left( \boldsymbol{\rho}_u^{c_u^+}(\mathbf{r}_u) \cdot \mathbf{E}^{i,c_u^+} + \boldsymbol{\rho}_u^{c_u^-}(\mathbf{r}_u) \cdot \mathbf{E}^{i,c_u^-} \right) = V_u^i \end{aligned} \quad (3.6)$$

where the tangential component of each is given by

$$\mathbf{E}^{i,c_u^\pm} = \mathbf{E}^i(\mathbf{r}_u^{c_u^\pm}). \quad (3.7)$$

The related voltage excitation vector for all elements can be written as

$$\mathbf{V} = \begin{pmatrix} \langle \mathbf{f}_1, \mathbf{E}^{i,c_1^\pm} \rangle \\ \dots \\ \langle \mathbf{f}_u, \mathbf{E}^{i,c_u^\pm} \rangle \end{pmatrix}. \quad (3.8)$$

In order to implement a source defined somewhere on the surface a feed model based on a driving RWG edge element is used [Mak02, Wen13]. The feed model is commonly called “delta function generator” or “feeding edge model” and the overall principle is shown in Fig. 3-3.

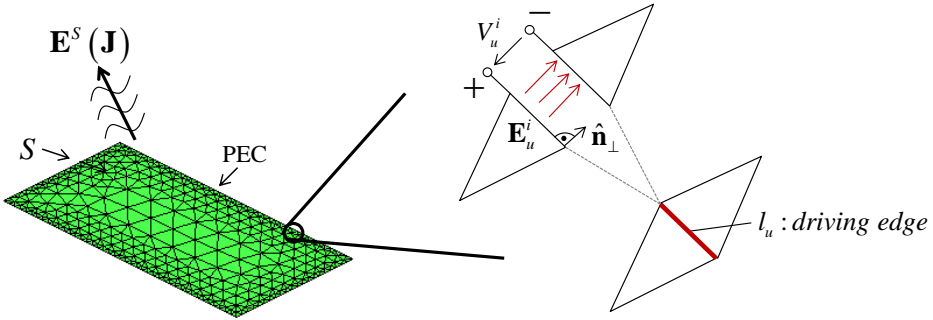


**Fig. 3-3** Equivalent surface problem with pre-located delta-gap excitation over a driving edge element.

As an example, the feed model consists of one “small gap” at the driving RWG edge element on the surface of the structure. This gap can be used to place a voltage generator between the two triangles  $T_u^\pm$ . Based on the voltage a uniform electric field can be impressed over the driving edge as follows [Mark02, Joh90, Eth14]:

$$\mathbf{E}_u^i = \frac{V_u^i}{\Delta} \hat{\mathbf{n}}_{\perp}. \quad (3.9)$$

The  $1/\Delta$  in (3.9) denotes the gap separation which can be replaced by a Dirac delta function and results to

$$\mathbf{E}_u^i \approx V_u^i \delta \hat{\mathbf{n}}_{\perp}. \quad (3.10)$$

The Dirac delta function is defined [Mar02]

$$\delta(x) = \begin{cases} +\infty, & x = 0 \\ 0, & x \neq 0 \end{cases} \quad (3.11)$$

and results in the integral to

$$\int_{-\infty}^{+\infty} \delta(x) dx = 1. \quad (3.12)$$

Multiplying this function with the applied voltage means that the integral of the electric field over the gap is equal to the applied voltage. Thus, the impressed electric field will be zero everywhere except for the  $u^{\text{th}}$  driving edge. Based on this special problem the voltage excitation vector can be expressed by each excitation by

$$\begin{aligned} \langle \mathbf{f}_u, \mathbf{E}_u^i \rangle &= \iint_{T_u^+ + T_u^-} \mathbf{f}_u \cdot \mathbf{E}_u^i dA \\ &= \iint_{T_u^+ + T_u^-} \mathbf{f}_u \cdot V_u^i \delta \hat{\mathbf{n}}_{\perp} dA \end{aligned} \quad (3.13)$$

which results to

$$\begin{aligned} V^i &= V_u^i \iint_{T_u^+ + T_u^-} \delta \mathbf{f}_u \cdot \hat{\mathbf{n}}_{\perp} dA \\ &= V_u^i l_u \end{aligned} \quad (3.14)$$

on the driving edge and

$$V^i = V_{u \neq u}^i \iint_{T_u^+ + T_u^-} \delta \mathbf{f}_u \cdot \hat{\mathbf{n}}_{\perp} dA = 0 \quad (3.15)$$

everywhere else on the structure.

The characteristic modes are defined by their modal surface current density. Therefore, it is natural to expand the coefficient  $I_u$  related to the  $n^{\text{th}}$  characteristic mode. Due to the orthogonal properties of the characteristic modes, the surface current density based on each  $u^{\text{th}}$  location  $\mathbf{J}(\mathbf{r})$  can be expressed as follows [Mark02, Yee73]:

$$\begin{aligned} \mathbf{J}(\mathbf{r}) &= \sum_{u=1}^U I_u \mathbf{f}_u(\mathbf{r}) \text{ with } I_u = \sum_{n=1}^N a_n I_{u,n} \\ &= \sum_{u=1}^U \sum_{n=1}^N a_n I_{u,n} \mathbf{f}_u(\mathbf{r}) \\ &= \sum_{u=1}^U \sum_{n=1}^N a_n \mathbf{J}_{u,n}(\mathbf{r}) . \end{aligned} \quad (3.16)$$

The main outcome of these formulations is the dependency of the characteristic modes related to the specific  $u^{\text{th}}$  RWG edge element. This means that each characteristic mode depends also on the localized modal excitation coefficient at the  $u^{\text{th}}$  edge element

$$V_n^i = \sum_{u=1}^U l_u V_u^i I_{u,n} . \quad (3.17)$$

The input current at the  $u^{\text{th}}$  driving edge is therefore defined by

$$I_{\text{in}} = I_u l_u = \sum_{n=1}^N a_n I_{u,n} l_u . \quad (3.18)$$

In (3.16) - (3.18),  $I_{u,n}$  denotes the characteristic mode current coefficient at the  $u^{\text{th}}$  driving edge element. Thus, this coefficient is a real scalar and directly related to the real characteristic modes  $\mathbf{J}_{u,n}(\mathbf{r})$  at that position.

### 3.3 Input admittance and impedance

If we expand (3.18) with the modal solution (2.28) and the internal excitation (3.17) the input current of the feed port can be obtained in a general formulation

$$I_{\text{in}} = \frac{1}{2} \sum_{n=1}^N \frac{V_n^i}{1 + j\lambda_n} I_{u,n} l_u = \frac{1}{2} \sum_{u=1}^U \sum_{n=1}^N \frac{V_u^i}{1 + j\lambda_n} (I_{u,n})^2 (l_u)^2. \quad (3.19)$$

Furthermore, the related input admittance of the driving edge can be obtained by

$$Y_{\text{in}} = \frac{I_{\text{in}}}{V_u^i} = \frac{1}{2} \sum_{u=1}^U \sum_{n=1}^N \frac{(I_{u,n})^2 (l_u)^2}{1 + j\lambda_n}, \quad (3.20)$$

which shows the direct link of the characteristic modes by the coefficient  $I_{u,n}$  [Eth10, Mar02, Eth14].

The real and imaginary parts can be separated to the modal conductance  $G_{\text{in}}$  and susceptance  $B_{\text{in}}$

$$\begin{aligned} Y_{\text{in}} &= G_{\text{in}} + jB_{\text{in}} \\ &= \frac{1}{2} \sum_{u=1}^U \sum_{n=1}^N \frac{(I_{u,n})^2 (l_u)^2}{1 + \lambda_n^2} + j \frac{1}{2} \sum_{u=1}^U \sum_{n=1}^N \frac{(I_{u,n})^2 (l_u)^2 (-\lambda_n)}{1 + \lambda_n^2}. \end{aligned} \quad (3.21)$$

If the eigenvalue  $\lambda_n$  of a specific characteristic mode, which is based on this excitation configuration becomes very large the respective modal admittance  $Y_{\text{in},n}$  of this mode approaches to zero and will have a negligible contribution to the input admittance. If the eigenvalue  $\lambda_n$  of a mode becomes small the respective modal admittance  $Y_{\text{in},n}$  becomes significant large and will contribute to the overall input admittance.

The input impedance is naturally the inverse of the input admittance:

$$\begin{aligned} Z_{\text{in}} &= (Y_{\text{in}})^{-1} \\ &= \frac{1}{\frac{1}{2} \sum_{u=1}^U \sum_{n=1}^N \frac{(I_{u,n})^2 (l_u)^2}{1 + j\lambda_n}} \\ &= R_{\text{in}} + jX_{\text{in}} \end{aligned} \quad (3.22)$$

where  $R_{\text{in}}$  and  $X_{\text{in}}$  denote the resistance and reactance of the input impedance at the driving edges.

### 3.4 Modal complex power including the modal excitation

Section 2.6 has shown that due to the orthogonal properties the radiated power in (2.32) reduces to the summation of the squared magnitudes of the weighting coefficients, whereas the reactive power in (2.34) reduces to the radiated power multiplied by the eigenvalue of the respective characteristic mode itself. Both can be combined to the resultant complex power as shown in (2.36).

With the knowledge of the localized driving edge elements the complex power of the characteristic modes can be expressed as

$$P_{\text{complex}} = \frac{1}{4} \sum_{n=1}^N \left| \frac{\sum_{u=1}^U l_u V_u^i I_{u,n}}{1 + j\lambda_n} \right|^2 (1 + j\lambda_n) \quad (3.23)$$

where the weighting coefficient can be separated out:

$$a_n = \frac{\sum_{u=1}^U l_u V_u^i I_{u,n}}{2(1 + j\lambda_n)}. \quad (3.24)$$

The weighting coefficient of the mode shows that both the eigenvalue and the internal driving edge location play a dominant role for the power control of the structure and can be used in the antenna design approach based on the TCM. Both parameters will be further evaluated and discussed in the following chapters.

Based on the complex power in (3.23) the radiated power and reactive power can be decomposed to

$$P_{\text{rad}} = \sum_{n=1}^N \left| \frac{1}{2} \frac{\sum_{u=1}^U l_u V_u^i I_{u,n}}{1 + j\lambda_n} \right|^2 \quad (3.25)$$

and

$$P_{\text{react}} = \sum_{n=1}^N \left| \frac{1}{2} \frac{\sum_{u=1}^U V_u^i I_{u,n}}{1 + j\lambda_n} \right|^2 \lambda_n. \quad (3.26)$$

The radiated power in (3.25) will be further used in subsection 4.3.1 to derive the power coefficient depending on the internal location of the source on the radiation structure and its relation to the modes.





# Chapter 4

## Modal Analysis of Simple Radiation Structures

By the definitions of the previous sections, orthogonal characteristic modes can be decomposed out of the surface current distribution of arbitrarily shaped conductive bodies. Therefore, a modal analysis of simple conducting bodies helps to understand the physical background of these conductive structures by using the TCM [Liu90, Gar82, Har60].

The aim of this chapter is to show the attractiveness of the characteristic mode analysis in antenna design processes and to derive which are the main modal parameters for antenna designers [She08, CFa07, Aus98].

The chapter consists of three main parts. It starts with a numerical analysis of a generic PEC strip. The eigenvalues, the modal significances, the radiating bandwidths and their quality factors of the first two modes will be analyzed. The second part is a numerical analysis of a few generic rectangular structures based on a parameter study. The width and the length of the strip will be used to show how this affects the derived modal parameters. The last part will analyze simple planar dipole antennas in order to understand how the dimensions and the internal source on the radiating structure (feed point) affects the power contribution of the modes. The decomposition of the normalized power coefficient shows the power contribution of each mode delivered to the antenna and the radiation.

The quantities derived and outlined in this chapter will be utilized in later chapters for a better understanding of more complex structures.

### 4.1 Modal analysis of a small rectangular strip

Fig. 4-1 shows a PEC strip having the dimensions of  $a = 10\text{mm} \times b = 120\text{mm}$ :

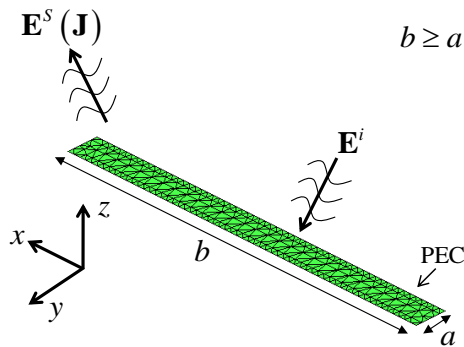


**Fig. 4-1** Scattering problem of a generic PEC strip.

#### 4.1.1 Analysis of the eigenvalues, the eigenfields and the current distributions

The characteristic modes  $\mathbf{J}_n$  and their respective eigenvalues  $\lambda_n$  are calculated.

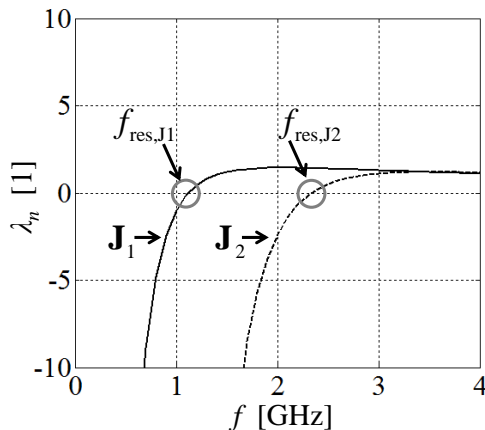


**Fig. 4-2** Eigenvalue analysis of the investigated small rectangular strip.

The physical interpretation can be made over the modal complex power balance. Both modes start from the large negative values ( $\lambda_n \ll 0$ ) below resonance ( $\lambda_n = 0$ ) and become small positive values above the resonances. Furthermore,  $\mathbf{J}_1$  and  $\mathbf{J}_2$  are resonating at  $f_{\text{res},J1} = 1.1\text{GHz}$  and  $f_{\text{res},J2} = 2.35\text{GHz}$  and their specific current distribution at these resonance frequency points are shown in Fig. 4-3.

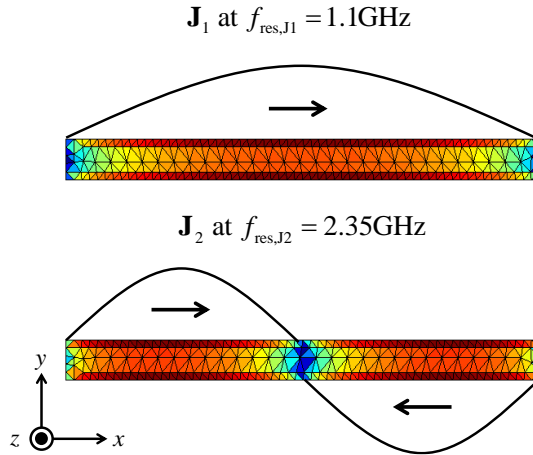


**Fig. 4-3** The normalized surface current distribution of the characteristic modes  $\mathbf{J}_1$  and  $\mathbf{J}_2$  at their resonance frequencies (magnitude plots).

Fig. 4-3 shows that both characteristic modes are mainly characterized by a sinusoidal current behavior on the strip

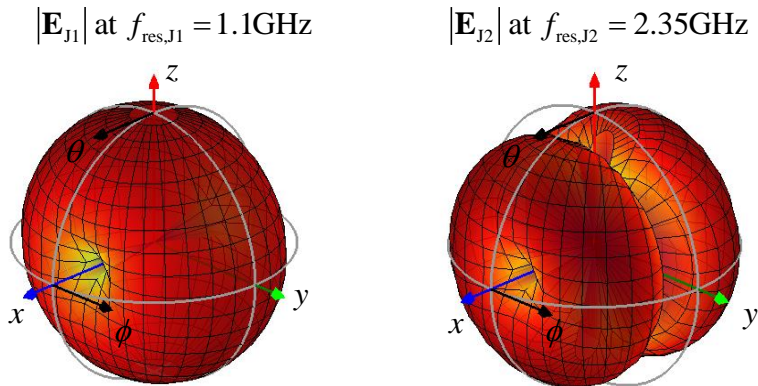


**Fig. 4-4** Calculated 3D radiation pattern of the two investigated modes at their resonance frequency in a logarithmic scale.

$\mathbf{J}_1$  and  $\mathbf{J}_2$  represent current distributions of a half and a full wavelength along the major axis ( $x$ -axis). Fig. 4-4 shows the related 3D radiation patterns of the two modes in Fig. 4-3 in a logarithmic scale and show typical radiation patterns of a half and full wavelength dipole. According to (2.30) the complex field are orthogonal to each other [Gar71, Har71\_1, Har71\_2].

### 4.1.2 Modal significance

As shown in the previous sections, the eigenvalues of the modes are very useful for analyzing structures about the power balance in (2.21).

In addition the so called modal significance

$$|MS_n| = \left| \frac{1}{1 + j\lambda_n} \right| \quad (4.1)$$

can be separated out of the weighting coefficient (2.28) [Aus98, Eth10]. The  $MS_n$  of the  $n^{\text{th}}$  mode depends on the physical shape, the frequency and size of the investigated radiation structures only, excluding the effect of the excitation.

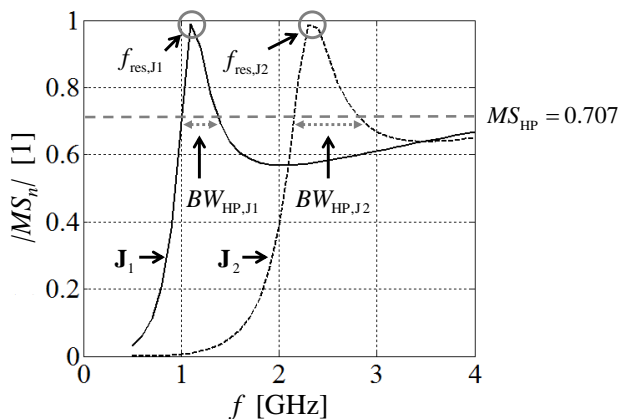


**Fig. 4-5** Modal significance analysis of the generic rectangular strip.

The  $MS_n$ 's of the two investigated characteristic modes  $J_1$  and  $J_2$  are shown in Fig. 4-5. The modal resonances coincide with the maxima of the  $MS_n$  curves, where no energy will be stored in the near field and the contribution of each mode to the radiation reaches a maximum. This can be proven by considering the derived modal solution of the complex power (see section 2.6) and its decomposition in the radiated power (2.33) and reactive power (2.35).

If a perfect excitation of the mode in its modal resonance ( $\lambda_n = 0$ ) is assumed the respective excitation coefficient is  $V_n^i = 1$ . That indicates a maximum degree of mode coupling with

$$P_{\text{rad},n}^{\text{max}} = \underset{=1}{|MS_n|^2 |V_n^i|^2} = |MS_n|^2, \quad (4.2)$$

$$P_{\text{reac},n} = \underset{=1}{|MS_n|^2} \underset{=0}{|V_n^i|^2} \lambda_n = 0. \quad (4.3)$$

In that case the radiated power of each mode is in its maximum and the reactive power is zero. In other words, the squared modal significance determines how significantly a particular mode contributes to the radiation and how efficiently a given mode can be used for antenna operation if it can be purely excited [Eth10].

### 4.1.3 Modal radiating bandwidth and quality factor analysis

In order to determine the radiation of each characteristic mode the radiation bandwidth potential can be obtained by analyzing the modal significance curves nearby their maxima [CFa07\_2]. Here we assume that the degree of coupling between the excitation and the respective characteristic mode is in a maximum, as already discussed in the previous section.

Therefore, the fractional half power bandwidth potential  $BW_{\text{HP},J_n}$  around the resonance of each mode can be determined by the terms [CFa07\_2]:

$$\text{HP}_{J_n} = \frac{P_{\text{rad},n}^{\text{max}}}{2} = \frac{|MS_n|^2}{2} = \left| \frac{MS_n}{\sqrt{2}} \right|^2, \quad (4.4)$$

where the modal significance threshold is

$$MS_{\text{HP}} = \frac{1}{\sqrt{2}} = 0.707. \quad (4.5)$$

The upper and lower limits in relation to the respective resonance frequencies of each mode are given by

$$BW_{\text{HP},J_n} = \frac{f_{\text{up},J_n} - f_{\text{low},J_n}}{f_{\text{res},J_n}}, \quad (4.6)$$

which are also marked in Fig. 4-5. Furthermore, based on (4.6) the modal quality factor

of each mode can be determined as

$$Q_{\text{rad},J_n} = \frac{1}{BW_{\text{HP},J_n}} \text{ if } Q_{\text{rad},J_n} \gg 1. \quad (4.7)$$

Values of the resonance frequency, the upper and lower frequency, the fractional radiating bandwidth and the quality factors of the generic structure are summarized in Table 4-1.

**Table 4-1** Resonance frequency, upper and lower frequency, modal radiation bandwidth and quality factor of the two investigated modes of the small rectangular strip.

Mode	$f_{\text{res},n}$ [GHz]	$f_{\text{up},n}$ [GHz]	$f_{\text{low},n}$ [GHz]	$BW_{\text{HP},J_n}$ [1]	$Q_{\text{rad},J_n}$ [1]
<b>J<sub>1</sub></b>	1.10	1.40	1.00	0.364	2.75
<b>J<sub>2</sub></b>	2.35	2.82	2.15	0.285	3.51

The accuracy of this modal quality factor approach (4.7) has been proven in [CFa07\_2] and compares the modal quality factors of the Foster reactance theorem in [Wen00, And07, Wen07, Bes04, Bes03] and the Harrington and Mautz approaches in [Har72]. As a result, all alternative definitions of the quality factor are equivalent and provide very similar values to each other.

## 4.2 Modal analysis based on a parameter study of a small generic plate

A parameter study is presented to illustrate how the eigenvalues and the modal significance are effected by the dimensions of the structure. Here the lengths of minor axis  $a$  and major axis  $b$  (see Fig. 4-1) will be varied. Only the first two characteristic modes **J<sub>1</sub>** and **J<sub>2</sub>** representing a half and full wavelength along the major axis (here the  $x$ -axis as shown Fig. 4-3) will be used for a comparison in the parameter study.

### 4.2.1 Variation example of the minor axis

Three examples are investigated where the minor axis length  $a$  of the structure varies while the length  $b$  of the major axis is fixed, as shown in Table 4-2. The first example

## 4.2 Modal analysis based on a parameter study of a small generic plate

( $a = 10\text{mm}$ ) is already investigated in section 4.1 and will be used as a reference in order to explain the changes of the modal parameters: eigenresonance, eigenvalue, modal significance and radiating bandwidth. The resonance frequencies in Table 4-2 show that the resonance of mode J1 is stable if the width  $a$  becomes larger, whereas for mode J2 the resonance shifts up in frequency and therefore shows a clear dependency on the width (see example 3).

**Table 4-2** Resonance frequencies of the first two investigated characteristic modes of the small rectangular strip by increasing the parameter  $a$ .

Example	$a$ [mm]	$b$ [mm]	$f_{\text{res},J1}$ [GHz]	$f_{\text{res},J2}$ [GHz]
1	10	120	1.1	2.35
2	30	120	1.1	2.35
3	60	120	1.1	2.6

As a result the eigenvalue analysis of the calculated mode  $J_1$  and  $J_2$  is illustrated in Fig. 4-6 left and right. In all three cases the slope of the eigenvalue curve around the resonances change due to the lower eigenvalues above the modal resonances. This can be interpreted in such a way that the larger the dimension ratio  $a/b$ , the lower the eigenvalues after the modal resonance of the respective modes and the more efficient the modes contribute to the radiation if excited, as explained in (4.2).

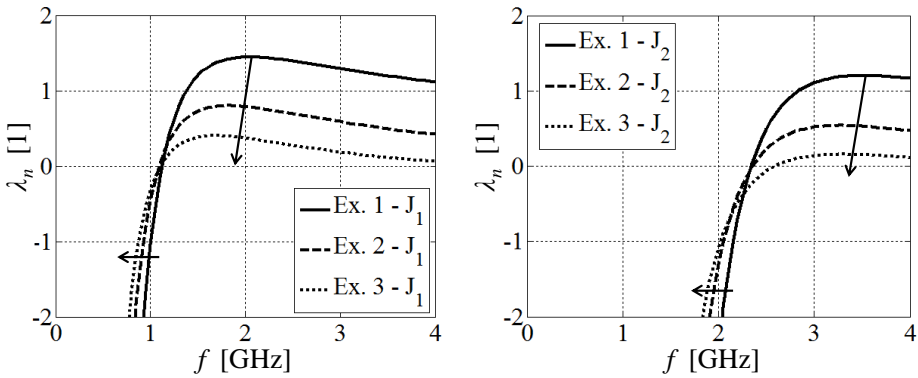


**Fig. 4-6** Eigenvalue analysis of the investigated structures of the characteristic modes  $J_1$  (left) and  $J_2$  (right).

#### 4. Modal Analysis of Simple Radiation Structures

It can be observed that the eigenvalues of both modes become  $|\lambda_n| < 1$  above the eigenresonance of both examples 2 and 3 (Fig. 4-6 left and right) if the rectangular plate becomes wider over the variation of the diameter  $a$ . In that case the net-energy  $W_{\text{net},n}$  decreases due to the decreased magnetic energy  $W_{\text{mag},n}$  and the respective mode becomes more significant (see section 2.4).

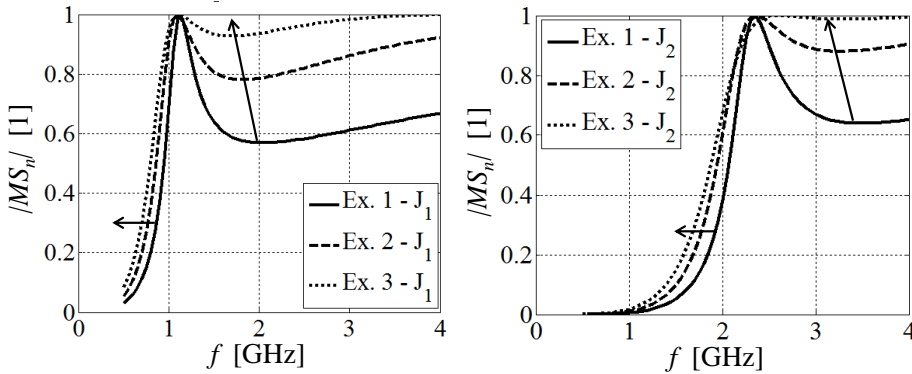


**Fig. 4-7** Modal significance of the investigated structures of the characteristic modes  $J_1$  (left) and  $J_2$  (right).

In addition, the modal significance of the modes  $J_1$  and  $J_2$  are calculated and illustrated in Fig. 4-7, which shows that the modal significance  $|MS_n|$  stays at a higher level ( $|MS_{\text{HP},n}| > 0.707$ ) after the resonance frequencies ( $|MS_n| = 1$ ) when  $a$  is increased. Due to the direct relation in (4.2), the radiation can be maximized if the respective mode with a large  $|MS_n|$  in a higher frequency range is excited.

As shown in Fig. 4-7, the higher the relation of the diameters ratio  $a/b$ , the broader the absolute bandwidth of each mode becomes and the modal radiation  $Q$  approach, shown in (4.7), cannot be used. Therefore, a new approach for the modal  $Q$  factor depending on the eigenvalue and model significance of each mode is needed.

#### 4.2.2 Modal radiation $Q$

In [Har72] an interpretation of the modal  $Q$  in terms of the frequency dependent eigenvalues of each mode is derived:



$$Q_{\text{eig},n} = \frac{\omega_0}{2} \left| \frac{d\lambda_n}{d\omega} \right|. \quad (4.8)$$

It contains the information about the frequency-dependent mode energies (see (2.21)). Furthermore, as shown in (4.1), the modal significance  $|MS_n|$  only depends on the physical shape and size of the investigated structure and is directly related to the radiated power of each mode, see (4.2). Therefore, if we derive the eigenvalue out of the  $|MS_n|^2$  we obtain:

$$|\lambda_n| = \sqrt{\frac{1 - |MS_n|^2}{|MS_n|^2}} = \sqrt{\frac{1 - P_{\text{rad},n}^{\text{max}}}{P_{\text{rad},n}^{\text{max}}}}. \quad (4.9)$$

If the degree of coupling reaches a maximum (see (4.2)) the term can be reformulated including the radiated power of each mode.

The following redefined formulation for the modal  $Q$  can be determined by substituting (4.9) into the Harrington formulation (4.8):

$$Q_{\text{eig},n} = \frac{\omega_0}{2} \frac{\left| d \left( \sqrt{\frac{1 - |MS_n|^2}{|MS_n|^2}} \right) \right|}{|d\omega|}, \quad (4.10)$$

which shows the direct relation of the frequency dependent  $|MS_n|^2$  of each mode.

The  $Q_{\text{eig},n}$  can be separated in the two individual contributions of magnetic and electric energies around the resonance of the mode

$$\begin{aligned} \lambda_n < 0: & \quad Q_{\text{eig},n}^{\text{el}} \quad \text{if } W_{\text{el},n} > W_{\text{mag},n} \\ \lambda_n > 0: & \quad Q_{\text{eig},n}^{\text{mag}} \quad \text{if } W_{\text{el},n} < W_{\text{mag},n} \end{aligned} \quad (4.11)$$

It separates the  $Q$  below and above the eigenresonance of the respective mode. This means the curve of the modal significance  $|MS_n|^2$  (see Fig. 4-8 left) can be explained based on the direct relation of the predominantly stored magnetic and electric energy around the mode resonance. In this resonance point no net energy  $W_{\text{net},n}$  will be stored and the associated

characteristic mode contributes to the radiation efficiently. The interesting part in that observation is the  $Q$  around this internal resonance (see Fig. 4-8 right). Both, the modal electric and magnetic contributions (see 4.11) to the energies, will be analyzed with same fractional bandwidth  $\Delta f = f_{el,up} - f_{el,low} = f_{mag,up} - f_{mag,low}$  by using (4.11). The fractional bandwidth should be chosen as small as possible due to the different slopes around the internal resonance, as shown in Fig. 4-8 (right). This approach allows us to describe the  $Q$  factor of perfectly conductive structures around the modal resonance of each mode. Summarizing both calculated contributions, the  $Q_{eig,n}$  should have nearly the same value by calculating it with the overall fractional bandwidth of ( $\Delta f' = f_{mag,up} - f_{el,low}$ ), as shown Fig. 4-9 (right).

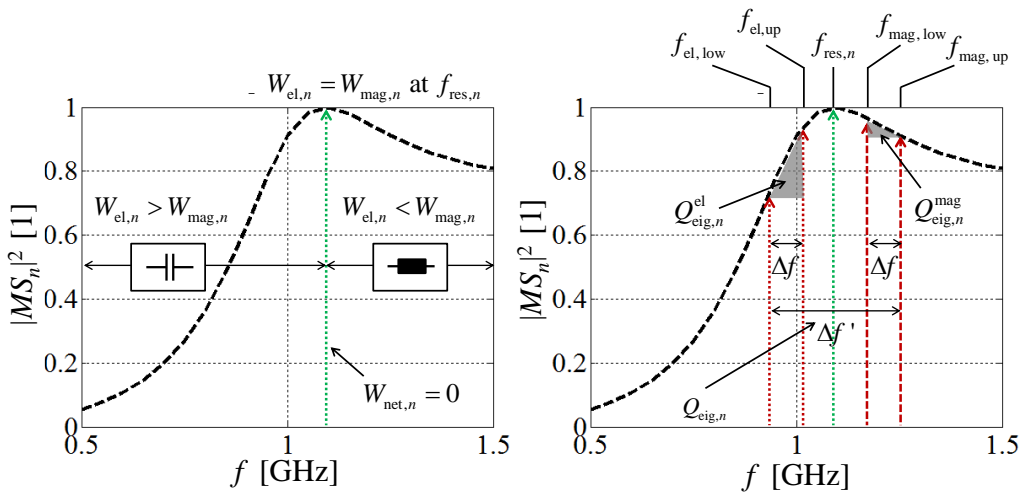


**Fig. 4-8** Modal significance dependency to the electric and magnetic energies (left) and the related electric and magnetic  $Q$  factors (right).

The advantage of this approach is the direct link to the frequency dependent modal significance  $|MS_n|^2$  curve and the radiation, as shown in (4.2). The separated  $Q$  factor will be used in chapter 0 for the modal analysis of a chassis with a typical mobile chassis dimension ratio of  $a/b = 0.5$  as same as in example 3 (see Table 4-2).

### 4.3 Modal analysis of simple dipole antennas

It must be noticed the whole perfectly conductive structure of an antenna has a dominant effect on the resonant frequencies of the characteristic modes. But by knowing the modal properties of the simplified structures, as shown in the previous sections, it becomes easier

to design an antenna system that utilizes the rectangular plate or a PCB (Printed Circuit Board) as a chassis. Depending on the frequency, the chassis can be used as the main radiator and thus the main contributor on the characteristic modes.

In order to understand the radiation of an antenna the following subsections will derive a normalized power coefficient which can be decomposed in a summation of delivered modal power contributions. Simple planar dipoles will be later used for the evaluation. The normalized power coefficient will be composed of the modal radiated power based on formulation (3-25) and the absolute power delivered to the antenna.

#### 4.3.1 Modal power coefficient based on the characteristic mode analysis

As shown in section 2.6, the total radiated power is the summation of the radiation power of all modes and can be reduced in a summation of the squared weighting coefficients, as shown in (2-32). This expression allows us to determine the amount of radiated power by the  $n^{\text{th}}$  mode depending on the  $u^{\text{th}}$  feed-point location (see (3-25)). If we normalize the summation of the squared weighting coefficients to the total radiated power we get the definition of the summation of the normalized coefficients [Aus98, Saf12, Saf13]:

$$\sum_{n=1}^N |b_n|^2 = \frac{\sum_{n=1}^N |a_n|^2}{P_{\text{rad}}} = 1. \quad (4.12)$$

The formulation (4.12) can be equated with the radiation efficiency

$$\eta_{\text{rad}} = \sum_{n=1}^N |b_n|^2 = \frac{\sum_{n=1}^N |a_n|^2}{P_{\text{rad}}}. \quad (4.13)$$

in which the terms

$$|b_n|^2 = \frac{|a_n|^2}{P_{\text{rad}}} \leq 1 \quad (4.14)$$

are equal to the percentage each mode contributes to the radiated power [Saf13].

By applying the expression (4.12) a reformulation including the  $u^{\text{th}}$  feed-point location and

#### 4. Modal Analysis of Simple Radiation Structures

---

modal significances  $|MS_n|^2$  can be derived

$$\frac{\sum_{n=1}^N \left| \frac{1}{2} \frac{\sum_{u=1}^U l_u V_u^i I_{u,n}}{1 + j\lambda_n} \right|^2}{P_{\text{rad}}} = \frac{\frac{1}{4} \sum_{n=1}^N |MS_n|^2 \left| \sum_{u=1}^U l_u V_u^i I_{u,n} \right|^2}{P_{\text{rad}}} = 1 \quad (4.15)$$

and decomposed in its modal terms

$$\frac{\frac{1}{4} |MS_n|^2 \left| \sum_{u=1}^U l_u V_u^i I_{u,n} \right|^2}{P_{\text{rad}}} \leq 1. \quad (4.16)$$

It shows how efficiently we direct the power into a specific characteristic mode of the radiating structure depending on a feed-point location.

If we extend the formulation (4.16) with the term of the delivered power to the antenna a new normalized power coefficient

$$\begin{aligned} \eta' &= \frac{\frac{1}{4} \sum_{n=1}^N |MS_n|^2 \left| \sum_{u=1}^U l_u V_{in,u} I_{u,n} \right|^2}{P_{\text{rad}}} (1 - |s_{uu}|^2) \\ &= \frac{P_{\text{abs},u}}{P_{\text{rad}}} \end{aligned} \quad (4.17)$$

can be used to evaluate lossless antenna systems including the power reflection at the port  $u$ . It shows that the absolute power delivered to the antenna  $P_{\text{abs},u}$  is direct related to the entire radiated power  $P_{\text{rad}}$  of the system. The power coefficient can also be decomposed into a set of modal components

$$\eta' = \sum_{n=1}^N \eta'_{Jn} \quad (4.18)$$

illustrating how each mode contributes to the delivered power at the feeding port  $u$ .

As a conclusion of this section, an additional parameter for radiation evaluation of lossless

and mismatched antennas including the feed point location is given. It shows that the eigenvalue and the reflection coefficient  $s_{uu}$  at the  $u^{\text{th}}$  port mainly determine the radiation performance. Both parameters are of general interest in the design of radiating structures based on the TCM.

### 4.3.2 Numerical analysis of dipole antennas based on the characteristic mode analysis

For the numerical validation of the normalized power coefficient  $\eta'$  (4.18), four examples with increasing complexity are discussed. In the first three examples simple dipoles with a fixed length  $b = 120$  mm, different widths  $a$  (here:  $a = 10$  mm,  $a = 30$  mm and  $a = 60$  mm) and a symmetric feed-point location in the middle of the structure are used for evaluation, as shown in Fig. 4-9 a-c. The fourth example in Fig. 4-9 d has the same dimensions as the example in Fig. 4-9 c, but the internal feed-point location is shifted to the outer edge of the major axis and results in an unsymmetrical excitation.

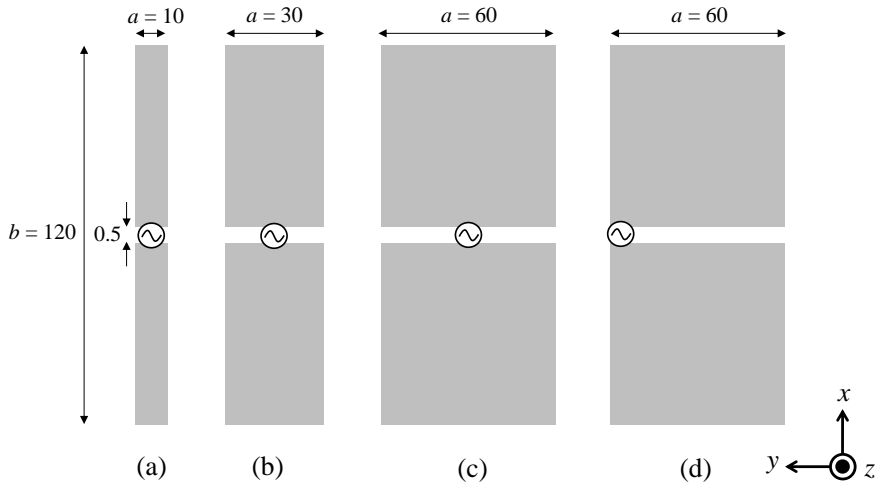


**Fig. 4-9** Illustration of four dipole with different dimensions and feed-point locations. Dimensions are in [mm].

All excitations are realized by the internal voltage feed gap explained in section 3.2.

The investigation begins with the smallest dipole (Fig. 4-9-a). It can be shown that this structure has only three relevant characteristic modes in the observed frequency range, shown in Fig. 4-10. All three modes are capacitive modes due to negative eigenvalues

#### 4. Modal Analysis of Simple Radiation Structures

below the respective resonance frequencies (here  $f_{\text{res},J_1} = 1.1\text{GHz}$ ,  $f_{\text{res},J_2} = 2.3\text{GHz}$  and  $f_{\text{res},J_3} = 3.5\text{GHz}$ ). Above the eigenresonances the modes have eigenvalues  $|\lambda_n| > 1$  (low  $|MS_n| < 0.707$ ) and therefore result in less effective radiation even if excited.

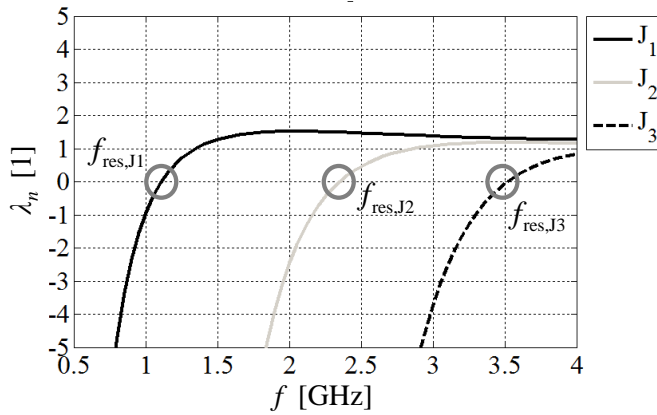


**Fig. 4-10** Eigenvalue analysis of the dipole from Fig. 4-9 (a).

The current distributions of the respective modes at their resonance frequency are illustrated in Fig. 4-14 showing that mode  $J_1$  has a length of a half-wave, mode  $J_2$  a full-wave and mode  $J_3$  one-and-a-half wave along the major axis.

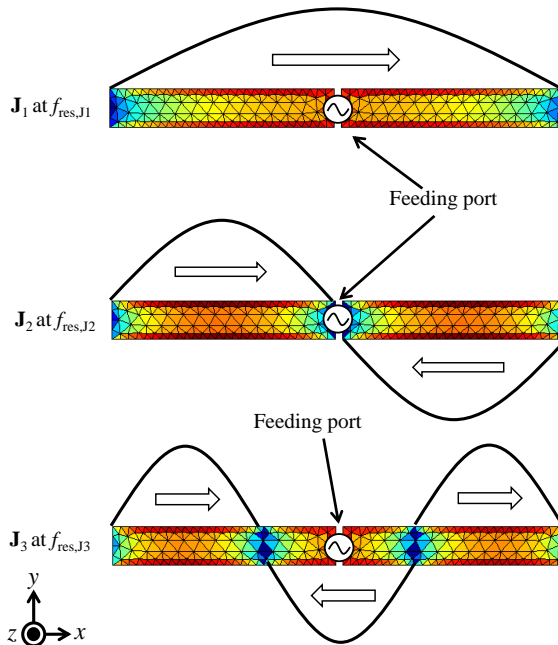


**Fig. 4-11** The first three normalized characteristic modes of the dipole from Fig. 4-9 (a).

As shown in Fig. 4-14, the feeding port is located in the current maximum of mode  $\mathbf{J}_1$  and in one of three current maxima of mode  $\mathbf{J}_3$ . In both cases the source imprint the currents directly in the current maximum of the mode and result in a mode excitation. In the case of mode  $\mathbf{J}_2$  the internal feeding port is located in a current minimum and should not excite the mode. In order to prove that prediction, the normalized power coefficient and its decomposition in the modal contributions are calculated and presented in Fig. 4-12.

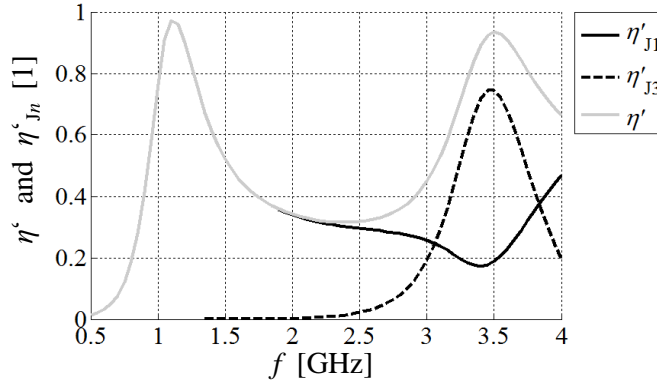


**Fig. 4-12** The calculated power coefficient and modal contributions of the dipole from Fig. 4-9 (a).

The modal contributions of the delivered power show exactly what we expect.  $\mathbf{J}_1$  and  $\mathbf{J}_3$  are excited, which results in two efficient radiation regions around the modal resonances of the excited characteristic modes ( $f_{\text{res},\mathbf{J}_1} = 1.1\text{GHz}$  and  $f_{\text{res},\mathbf{J}_3} = 3.5\text{GHz}$ ). As shown in Fig. 4-12, in the lower frequency range only the mode  $\mathbf{J}_1$  significantly contributes to the total power while in the higher frequency range there is an additional contribution of mode  $\mathbf{J}_3$ . A comparison of the modal power contributions shows that mode  $\mathbf{J}_1$  is more efficiently excited than mode  $\mathbf{J}_3$ . If mode  $\mathbf{J}_3$  can be excited in all of the three current maxima (see Fig. 4-11 bottom) at the same time the modal excitation coefficient of mode  $\mathbf{J}_3$  can be drastically improved, in the region where  $|\lambda_3| \leq 1$  ( $|MS_3| \geq 0.707$ ). By doing this the modal excitation coefficient of mode  $\mathbf{J}_1$  will be decreased due to the weaker coupling of  $\mathbf{J}_1$ . The modal contribution of mode  $\mathbf{J}_2$  becomes zero and is neglected in Fig. 4-12.

If we increase  $a$  to 30mm (see Fig. 4-9-b) more modes ( $\mathbf{J}_4 - \mathbf{J}_6$  and  $\mathbf{J}_{01} - \mathbf{J}_{02}$ ) become relevant in the observed frequency range (see Fig. 4-13). The additional modes  $\mathbf{J}_4 - \mathbf{J}_6$  are also

#### 4. Modal Analysis of Simple Radiation Structures

characterized by their orthogonal current paths over the structure (modes  $\mathbf{J}_1 - \mathbf{J}_3$ ) and present a capacitive nature at low frequencies. However, the modes  $\mathbf{J}_{01} - \mathbf{J}_{02}$  are inductive modes ( $\lambda_n > 0$ ) due to the inductive nature of the currents forming loops over the structure. Such modes will be labeled with an additional zero in the indexes  $\mathbf{J}_{0n}$ .

The eigenvalue analysis in Fig. 4-13 shows that the resonances of the modes  $\mathbf{J}_1$  and  $\mathbf{J}_3$  shift down towards lower frequency due to the larger physical size of the radiating structure (here  $f_{\text{res},J_1} = 1.03\text{GHz}$  and  $f_{\text{res},J_3} = 3.25\text{GHz}$ ). The resonance of mode  $\mathbf{J}_2$  is stable at  $f_{\text{res},J_2} = 2.3\text{GHz}$ .

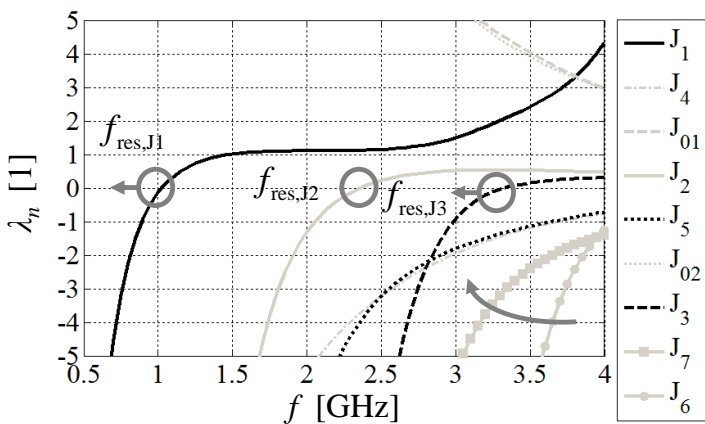


**Fig. 4-13** Eigenvalue analysis of the dipole from Fig. 4-9 (b).

The current paths of the modes need a longer way around the edges and the excitation slot in the middle of the structure (here shown for the dominant modes  $\mathbf{J}_1$  and  $\mathbf{J}_3$  in Fig. 4-14).

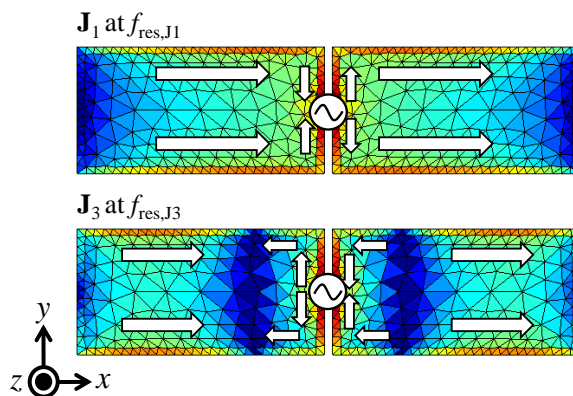


**Fig. 4-14** Two dominant characteristic modes of the dipole from Fig. 4-9 (b).



As shown in Fig. 4-14, the feeding port in this example is directly located in the maximum of the mode  $\mathbf{J}_1$  and in one of three maxima of mode  $\mathbf{J}_3$ . This indicates that this both modes are excited. In addition, the eigenvalue curves of both modes have a low slope after the modal resonances, which results in a broad efficient radiation region if these modes are excited.

The modal power contributions delivered to the antenna in Fig. 4-18 show that only mode  $\mathbf{J}_1$  (black curve),  $\mathbf{J}_3$  (dashed black curve) and a part of mode  $\mathbf{J}_5$  (dotted black curve) are excited within the observed frequency range. Both significant modes ( $\mathbf{J}_1$  and  $\mathbf{J}_3$ ) are depicted in Fig. 4-14.

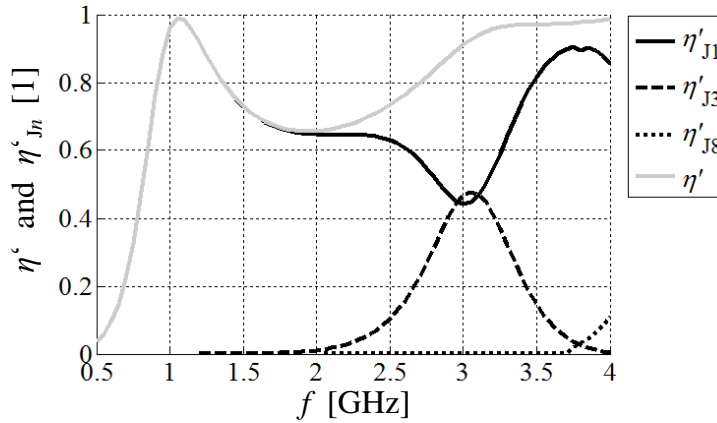


**Fig. 4-15** The calculated power coefficient and modal contributions of the dipole from Fig. 4-9 (b).

The power contribution of mode  $\mathbf{J}_1$  is  $\eta'_{J1} \geq 75\%$  in a broad region around  $f_{\text{res},J1} = 1.03\text{GHz}$  and in a higher frequency range at around  $f = 3.75\text{GHz}$  (see Fig. 4-15). Mode  $\mathbf{J}_3$  yields a strong excitation around its own resonance  $f_{\text{res},J3} = 3.3\text{GHz}$  and results in combination with the mode  $\mathbf{J}_1$  in an efficient radiation region in the high frequency range as well. Compared to the previously discussed small dipole case, the dominance of the excited mode  $\mathbf{J}_3$  reduces. The total normalized power coefficient results in a broader radiation bandwidth within the low and high frequency range as shown in Fig. 4-15. In conclusion,  $\eta' \geq 60\%$  can be achieved in a frequency range of  $0.8 \leq f [\text{GHz}] \leq 4$ .

For the dipole ( $a = 60\text{mm}$ ), as defined in Fig. 4-9-c, there are more than nine characteristic modes with a low eigenvalues available in the observed frequency range (see Fig. 4-16).

#### 4. Modal Analysis of Simple Radiation Structures

The eigenvalue of mode  $\mathbf{J}_1$  is deformed in such a way that the resonance is shifted below 1GHz based on the increased physical size. The current paths of the modes become longer due to the increased form factor of the structure itself. As previously shown only a couple of modes will be excited effectively due to the symmetrically located feed point (the three black marked curves in Fig. 4-16). Here only the modes  $\mathbf{J}_1$ ,  $\mathbf{J}_6$  and  $\mathbf{J}_8$  are excited and their current distribution at their resonances are illustrated in Fig. 4-17. The order of the modes in the indexes is based on the order of the resonances starting at lowest frequency.

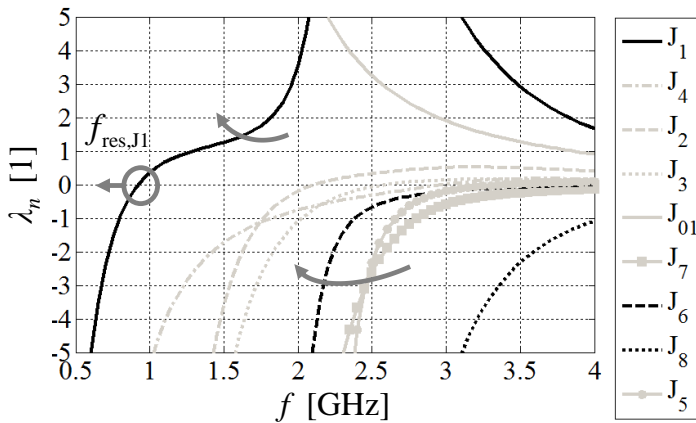


**Fig. 4-16** Eigenvalue analysis of the dipole from Fig. 4-9 (c).

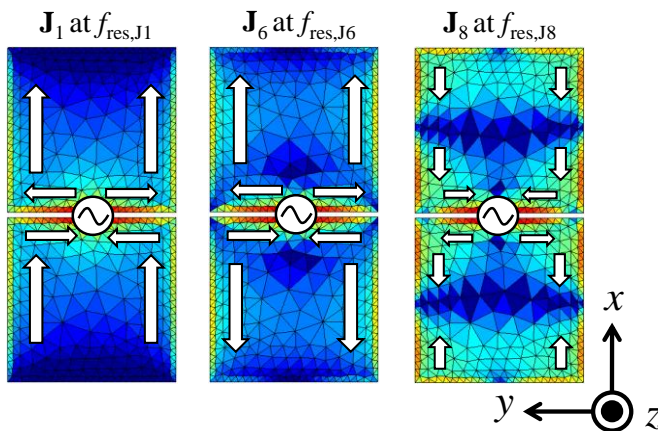
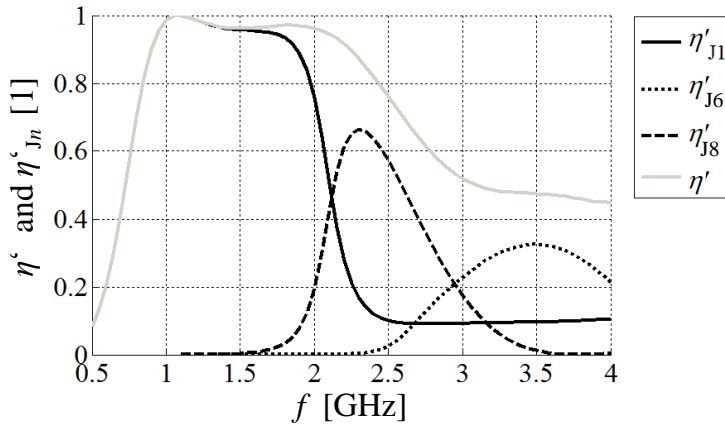


**Fig. 4-17** Three dominant characteristic modes of the dipole shown in Fig. 4-9 (c).

The current distribution in Fig. 4-17 shows that the path of the current becomes dominant with respect to the current paths around the edges and the slot itself. Due to the vicinity of

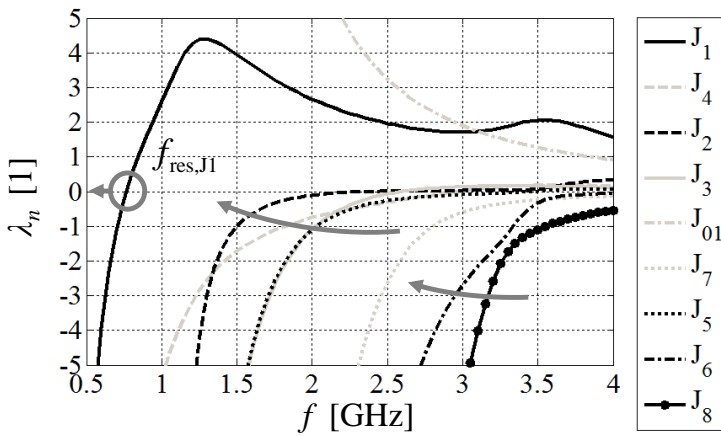
the slot the current paths go in opposite directions and cancel each other in the far-field as it will be shown later shown in the chapter 6.4.2.

Fig. 4-18 shows the calculated power contribution of the structure and confirms the excitation of the mode  $\mathbf{J}_1$ ,  $\mathbf{J}_6$  and  $\mathbf{J}_8$ . The excitation has a heavy effect on the normalized power coefficient, reaching  $\eta' = 75\%$  or more in a range of  $0.75 \leq f [\text{GHz}] \leq 2.75$ . A clear indicator of such a broadband radiation performance lies in the strong excitation of mode  $\mathbf{J}_1$  and its slope of the eigenvalue curve around the eigenresonance. In the higher frequency range the power coefficient  $\eta' \geq 45\%$  due to the excitation of the modes  $\mathbf{J}_6$  and  $\mathbf{J}_8$ , while the contribution of mode  $\mathbf{J}_1$  decays.



**Fig. 4-18** The calculated power coefficient and modal contributions of the dipole from Fig. 4-9 (c).

In case of an unsymmetrical structure, e.g. the dipole shown in Fig. 4-9 d, the current paths with respect to physical length become much longer than in the three previously discussed cases. That means that more characteristic modes with low eigenvalues shift downwards in the observed frequency range (see Fig. 4-19). For reducing the complexity of the analysis only nine modes with eigenvalues  $|\lambda_n| \leq 5$  related to this unsymmetrically dipole are considered. As shown in Fig. 4-19, the modal resonance of mode  $\mathbf{J}_1$  is shifted to  $f_{\text{res},\mathbf{J}_1} = 0.75\text{GHz}$  and results in a high slope of the eigenvalue curve around that point. This indicates that if mode  $\mathbf{J}_1$  is excited the bandwidth potential around that point becomes small (see chapter 4.1.3). In the higher frequency region the slopes of the other modes are mostly low derivative and should result in a broad but less efficient radiation.



**Fig. 4-19** Eigenvalue analysis of the dipole from Fig. 4-9 (d).

The power coefficient analysis in Fig. 4-20 shows that only five modes affects the radiation with  $\eta'_{Jn} \geq 20\%$ . The analysis can be discussed deeper at the points 1, 2, 3 and 4. The strongest contribution at point 1 and 2 is based on the modal power contributions of the excited modes  $J_1$  and  $J_2$  respectively. At points 3 and 4 the modes  $J_5$  and  $J_6$  strongly increase the power coefficient. At all of these points the eigenvalues of the excited modes are low and the slope of the curves are changed drastically. A comparison with the previous dipole shows that due to the shift of the internal feeding port the power contribution and the amount of the excited modes can be manipulated.

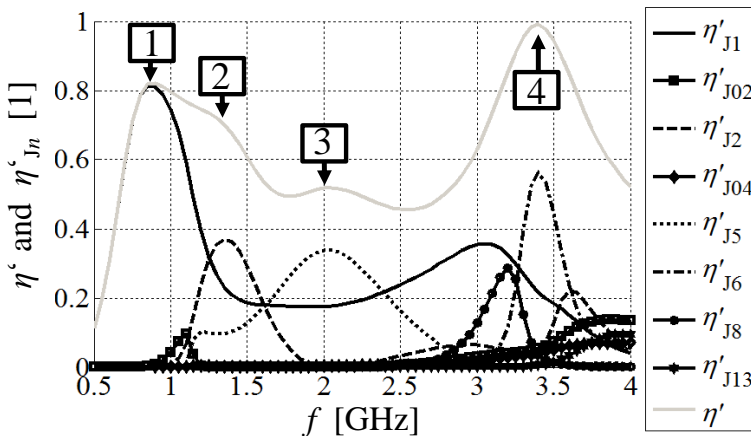


**Fig. 4-20** The calculated power coefficient and modal contributions of the dipole from Fig. 4-9 (d).

Summarized, Fig. 4-19 shows that modes  $\mathbf{J}_1$  and  $\mathbf{J}_2$  affect the radiation in the low frequency range, the modes  $\mathbf{J}_1$  and  $\mathbf{J}_5$  affect the radiation in the middle frequency range and modes  $\mathbf{J}_1$ ,  $\mathbf{J}_6$  and  $\mathbf{J}_8$  affect the radiation in the high frequency range. This results in a normalized power coefficient of the system with  $\eta' \geq 60\%$  in the low ( $0.7 \leq f [\text{GHz}] \leq 1.5$ ),  $\eta' \geq 45\%$  in the middle ( $1.5 \leq f [\text{GHz}] \leq 3$ ) and  $\eta' \geq 60\%$  in the high frequency range ( $3 \leq f [\text{GHz}] \leq 3.85$ ).

The normalized current distributions of the five dominant modes including the current directions are illustrated in Fig. 4-21 and show how complex the current paths over the unsymmetrical radiation structure are. Here the maxima and the minima of the current distributions occur at different locations over the edge of the structure. The strong current around the slot will be canceled in the far field due to the vicinity of opposite currents.

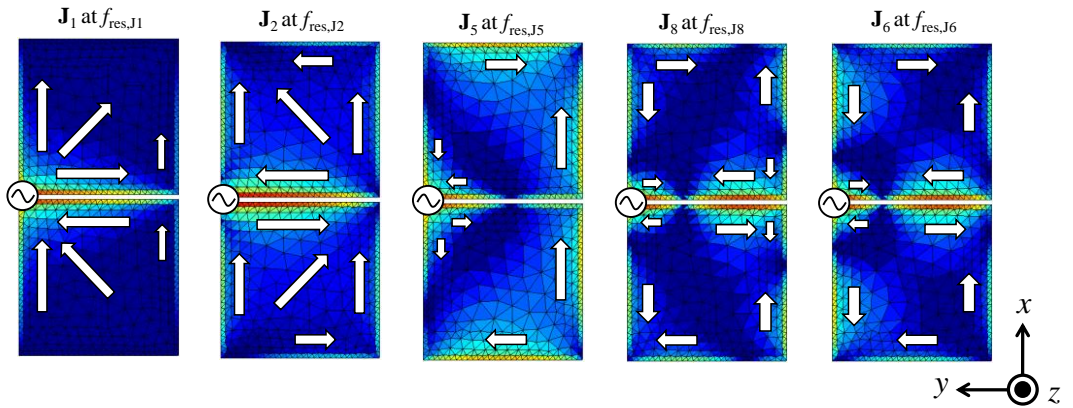


**Fig. 4-21** Five dominate characteristic modes of the dipole from Fig. 4-9 (d).

The investigations of the four different dipoles show that the physical outer dimensions can be used to change the energy distribution between the characteristic modes. It means that the structure itself can be used to form the eigenvalue behavior and the modal radiation across the frequency range of interest. The location of the feed-point in a given system can be used to excite the characteristic modes in a selective and/or common way. It has also been shown that by increasing the complexity of the structure (here the slot and the width  $a$ ) the current distribution of the respective modes become more complex. To enhance the radiation the best location of the feed-point must be additionally investigated.

#### 4. Modal Analysis of Simple Radiation Structures

Furthermore, one non-negligible key parameter for antenna designers is the reflection coefficient of the  $u^{\text{th}}$  feeding-point

$$S_{uu} = \frac{Z_{\text{in},u} - Z_0}{Z_{\text{in},u} + Z_0}, \quad (4.19)$$

which describes how well the power is transferred from the source to the antenna [Poz11, Gus12].  $Z_0$  denotes the reference impedance of the source at the feed-point  $u$  and is assumed to be equal to  $50\Omega$ .  $Z_{\text{in},u}$  denotes the input impedance (see section 3.3) of the driving edge  $u$  and depends on the contribution of all excited characteristic modes at that feed-port location. Fig. 4-22 shows the calculated reflection coefficients of all the dipole configurations.

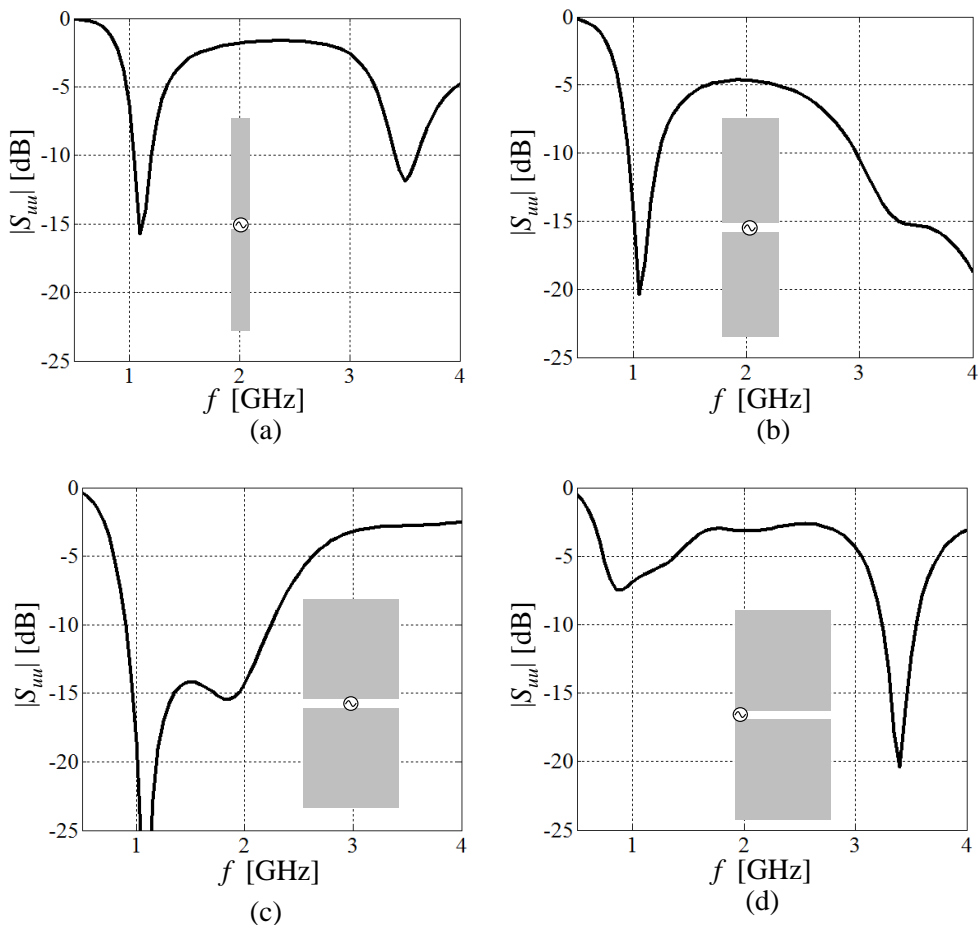


**Fig. 4-22** The calculated reflection coefficients of the of the dipoles from Fig. 4-9 (a-d).

The normalized power coefficients of the dipoles (see Fig. 4-12, Fig. 4-15, Fig. 4-18 and Fig. 4-20) can be maximized exactly where the maximized power transfer of the input port  $u$  occurs, since  $\eta_{\text{rad}} = 1$  by definition (4.12) and (4.13). The modal power contributions are directly related to the power delivered to the antenna structure by the term  $(1 - |s_{uu}|^2)$ , as shown in (4.18).





# Chapter 5

## Selective Excitation of the Characteristic Modes of the Small Rectangular Plate

The first approach to use the chassis of a small mobile handheld device as the principal main radiator was developed and published by Vainikainen et al. [Van02, Van00]. He described the characteristic modes as resonating wave modes on the chassis and derived an equivalent resonant circuit model which combined the radiation and the coupling behavior of the chassis and the antenna element itself. Furthermore, Vainikainen suggested to reduce the size of the mobile terminal by using essentially non-resonant coupling elements which efficiently excite the dominating characteristic modes either by magnetic or electric field coupling [PVa00]. Based on this idea several researchers have determined the optimal feeding location and configuration of such elements on the chassis and investigated which modes are strongly excited [CFa07, Dav08, Rah07, Fam07, Son11, Cha08, Cha10, Sch06].

The aim of this chapter is to present the selective excitation of desired characteristic modes on small mobile platforms by using the terminal itself as an antenna. Using a terminal-size rectangular plate as platform, the advantages and disadvantages of the selective magnetic and electric coupling of three different characteristic modes will be studied. Distributed inductive and capacitive probes are used as exciters [I, II, V]. A systematic characteristic mode analysis will show which modes are excited and which are not excited. By contrast, chapter 6 will present a study on excitation of multiple modes with the same exciter [IV, VI, VII]. The idea behind the selective excitation is to facilitate the use of multiple-antenna

## 5. Selective Excitation of the Characteristic Modes of the Small Rectangular Plate

---

systems with low mutual coupling [Mar\_12, IV, V, VIII], while the common mode excitation of modes can be utilized to optimize the single antenna system (matched bandwidth, radiated and delivered power) [VI, Mar\_14, Ilv14].

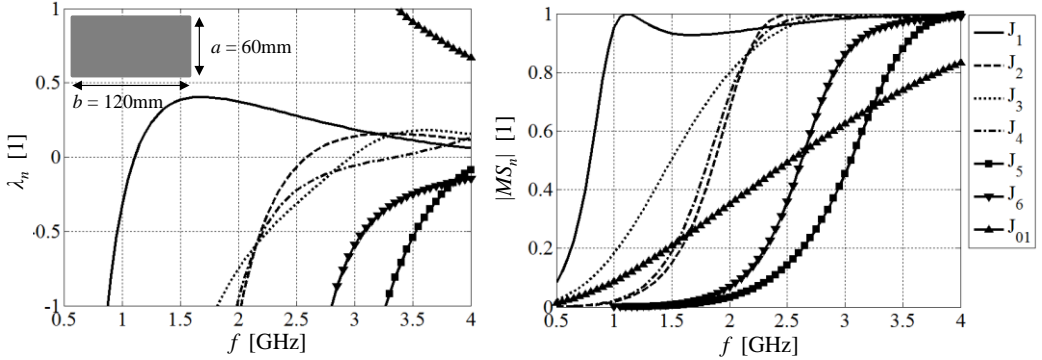
This chapter is composed of five sections. As first, section 5.1 starts with a modal analysis of a chassis, which has a typical dimension ratio as a commonly used PCBs in small handheld devices. Three characteristic modes with low eigenvalues in the observed frequency range are chosen for the selective excitation. Section 5.2 investigates optimal locations for a selective inductive and capacitive excitation of the desired modes. Here, sets of non-resonant inductive (IP) and capacitive (CP) probes are used to evaluate the selective excitation of the desired modes if these sets are distributed in optimal locations on the chassis. For a realistic implementation different non-resonant coupling structures are investigated in order to find the best candidate for the selective inductive or capacitive excitation of the desired modes (section 5.3). The last two sections, 5.4 and 5.5, evaluate the selective inductive and capacitive excitation by using the previously discussed non-resonant coupling elements distributed in the optimal locations with respect to desired modes. As a conclusion, the concepts are compared to each other.

### 5.1 Modal analysis of a small rectangular plate

From the EM point of view a simple possible chassis on a small handheld device is a perfectly conducting plate representing the Printed Circuit Board (PCB) itself. This assumption is based on neglecting the influences of the RF (Radio Frequency) front-end parts, the RF-shielding, the housing, the display and the battery. Such assumptions are commonly used nowadays for designing antennas for handheld devices [Mie13, Hui14, KKi13, KKi14].

As shown in sub-section 4.3.2, the TCM is a useful tool to calculate the characteristic mode  $\mathbf{J}_n$  of such a rectangular plate through applying the generalized eigenvalue problem. By solving the equivalent problem the eigenvalue  $\lambda_n$  and the modal significance  $|MS_n|$  of a complete set of characteristic modes  $\mathbf{J}_n$ , can be obtained. In our case the chassis under investigation has the dimensions of  $a = 60\text{mm}$  and  $b = 120\text{mm}$  (diameter ration  $a/b = 0.5$ ),

as shown in Fig. 5-1. The same size of the plate was used in the parameter study to investigate the  $Q_{\text{eig},n}$  and the eigenresonances of the first two modes in section 4.2. The used dimensions are comparable with the chassis dimensions of commercial phones on the market, for example, Apple iPhone 5S ( $a = 58.6\text{mm} \times b = 123.8\text{mm}$ ) or Nokia Lumia 800 ( $a = 61.2\text{mm} \times b = 116.5\text{mm}$ ).



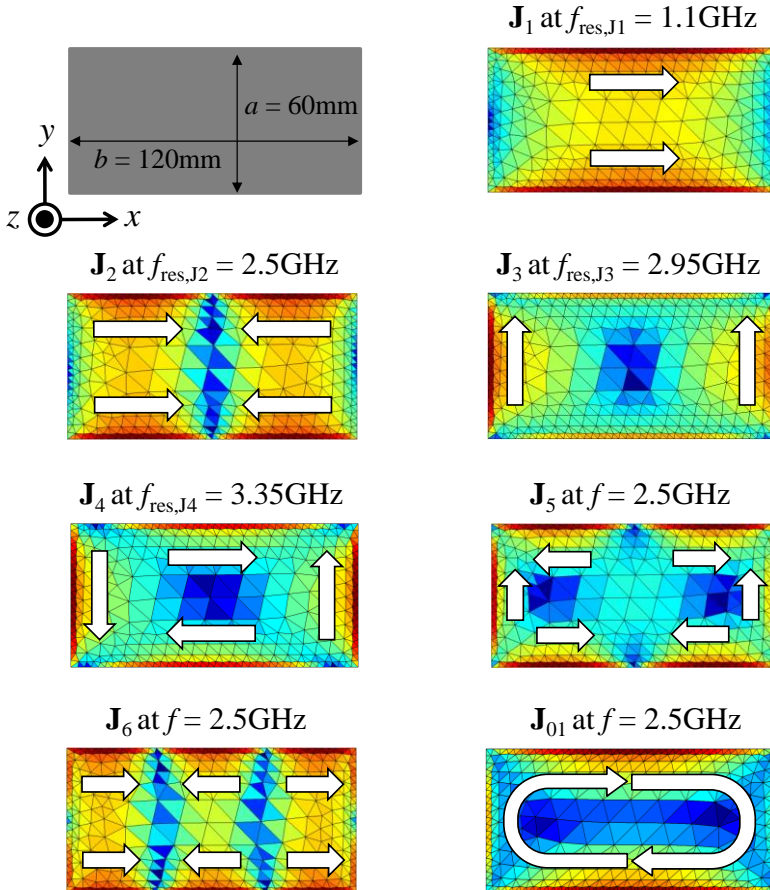
**Fig. 5-1** Calculated eigenvalues (left) and modal significances (right) of a generic rectangular plate with the dimensions of  $a \times b$  (60mm  $\times$  120mm).

Fig. 5-1 a shows the calculated eigenvalues  $\lambda_n$  of the first seven characteristic modes  $\mathbf{J}_n$  in a range of  $|\lambda_n| \leq 1$ . The frequency range is  $0.5 \leq f [\text{GHz}] \leq 4$ . For the graphical interpretation the eigenvalue range ( $\lambda_n = \pm 1$ ) is chosen as small as possible in order to enlarge the slopes of each curve. It can be observed that the characteristic modes  $\mathbf{J}_1$ ,  $\mathbf{J}_2$ ,  $\mathbf{J}_3$  and  $\mathbf{J}_4$  have their eigenresonances within the observed frequency range, whereas  $\mathbf{J}_5$ ,  $\mathbf{J}_6$  and  $\mathbf{J}_{01}$  resonate at higher frequencies. Furthermore, as explained in sub-section 4.1.3, the depicted modal significances reach  $|MS_n| \geq 0.707$  at different frequency ranges. This means that the closer the  $|MS_n|$  curve is to its maximum value, the more efficiently the associated mode contributes to the radiation if excited. Here the value  $|MS_n| = 0.707$  ( $|\lambda_n| = 1$ ) gives the half power contribution to the radiation and can be used as a radiation evaluation factor. It indicates the radiation potential of the chassis modes.

Fig. 5-2 illustrates the normalized current distributions of the modes  $\mathbf{J}_1$ ,  $\mathbf{J}_2$ ,  $\mathbf{J}_3$  and  $\mathbf{J}_4$  at their respective eigenresonances. Due to the non-resonant behavior within the observed frequency range the current distribution of the modes  $\mathbf{J}_{01}$ ,  $\mathbf{J}_5$  and  $\mathbf{J}_6$  are shown at  $f = 2.5\text{GHz}$ . Each mode has different current schematics. The modes  $\mathbf{J}_1$ ,  $\mathbf{J}_2$ ,  $\mathbf{J}_3$ ,  $\mathbf{J}_4$ ,  $\mathbf{J}_5$  and

## 5. Selective Excitation of the Characteristic Modes of the Small Rectangular Plate

$\mathbf{J}_6$  are characterized by their current paths over the structure representing a capacitive nature, whereas  $\mathbf{J}_{01}$  is characterized by an inductive current which is forming a closed loop over the plate (inductive nature).



**Fig. 5-2** Normalized current distribution and schematics of the first seven characteristic modes of the generic rectangular plate.

The current distributions of the modes have mainly sinusoidal magnitude distributions along the edges of the observed rectangular plate based on the edge condition of the surface currents.  $\mathbf{J}_1$  and  $\mathbf{J}_3$  represent current distributions of half a wavelength along the major and minor edges of the PCB respectively, whereas  $\mathbf{J}_2$  presents a current distribution of a full wavelength along the major edges. Mode  $\mathbf{J}_6$  represents one-and-a-half wavelength and can be seen as a higher order mode based on the eigenresonance out of the observed frequency range. Modes  $\mathbf{J}_4$  and  $\mathbf{J}_5$  represent a superposition of out-of-phase current distributions

along the outer edges. Here, mode  $\mathbf{J}_4$  is characterized by two half wavelength's on the major and minor edges, which are  $180^\circ$  out-of-phase two each other. The mode  $\mathbf{J}_5$  is characterized by the superposition of a full wavelength on the major edges and a half wavelength on the minor edges. The current distribution path of mode  $\mathbf{J}_{01}$  flows around the plate with an in-phase direction at all edges.

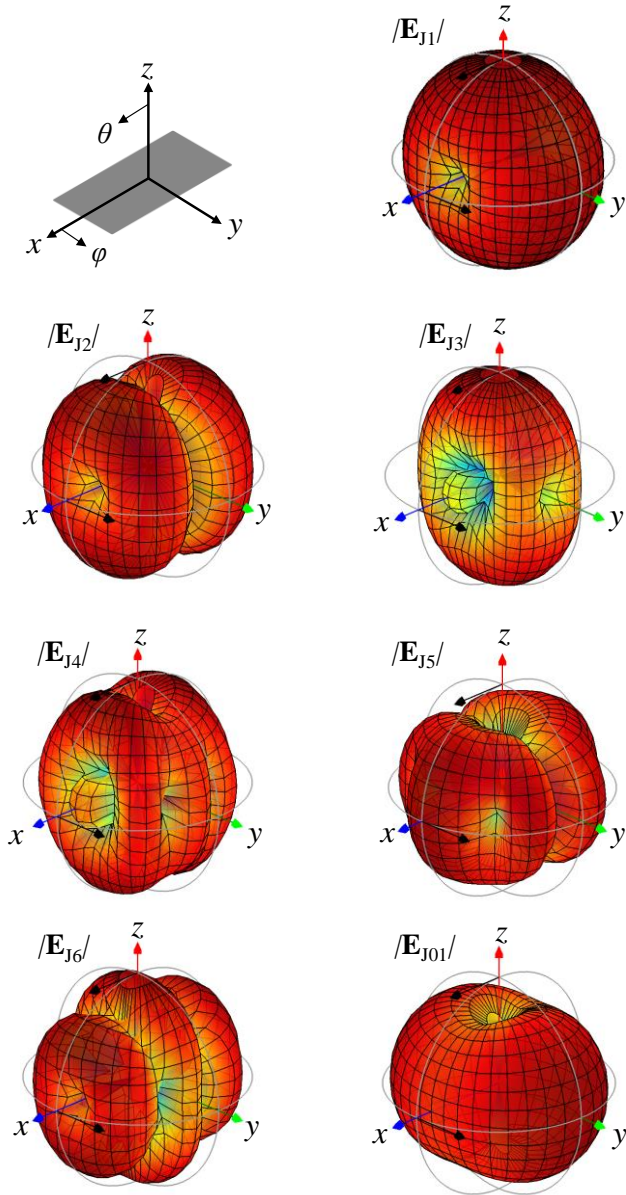


**Fig. 5-3** 3D radiation pattern of the first seven characteristic modes of the generic rectangular plate shown in Fig. 5-1.

## 5. Selective Excitation of the Characteristic Modes of the Small Rectangular Plate

Fig. 5-3 shows the three-dimensional (3D) radiation patterns of the seven modes of Fig. 5-2. According to the TCM these radiation patterns are orthogonal to each other (see section 2.3).  $|\mathbf{E}_{J1}|$  and  $|\mathbf{E}_{J2}|$  represent the absolute values of typical radiation patterns of a half and one wavelength dipole along the major axis ( $x$ -axis). Additionally,  $|\mathbf{E}_{J3}|$  represents the absolute values of the radiation pattern of a half-wavelength current along the minor edges ( $y$ -axis) of the PCB. The patterns of  $|\mathbf{E}_{J4}|$ ,  $|\mathbf{E}_{J5}|$  and  $|\mathbf{E}_{J6}|$  are mostly super-positioned grating lobes as the order of the mode increases. The radiation pattern  $|\mathbf{E}_{J01}|$  of the mode  $\mathbf{J}_{01}$  presents a nearly omni-directional 3D radiation characteristic in the  $xy$ -plane.

It should be noted that the actual radiation patterns of the observed modes are a complex angular dependent representation of the field vectors. For the later calculation the entire information is taken into account, while phase and polarization information is omitted from Fig. 5-3. Each polarization is directly related to the orientation of the current distribution of the modes on the PCB. Here, e.g. the polarizations of modes  $\mathbf{J}_1$  and  $\mathbf{J}_2$  are orientated in  $x$ -direction and that of mode  $\mathbf{J}_3$  is orientated in  $y$ -direction. The three radiation patterns correspond to the current distributions shown in Fig. 5-2.

**Table 5-1** Calculated eigenresonances and quality factors of the generic rectangular plate from Fig. 5-1.

Mode	$f_{res,n}$ [GHz]	$Q_{eig,n}^{el}$ [1]	$Q_{eig,n}^{mag}$ [1]	$Q_{eig,n}$ [1]
$\mathbf{J}_1$	1.10	2.13	0.80	1.46
$\mathbf{J}_2$	2.60	1.11	0.56	0.83
$\mathbf{J}_3$	2.95	0.98	0.77	0.88
$\mathbf{J}_4$	3.35	0.30	0.38	0.34

Table 5-1 shows the eigenresonances and the corresponding quality factors of the first four modes  $\mathbf{J}_1$  -  $\mathbf{J}_4$ . The investigated fractional frequency range around the eigenresonances is given by  $\Delta f'' = 300\text{MHz}$  and can be used to calculate the modal electric and magnetic contribution of the modal radiation  $Q_{eig,n}$  below and above the modal resonance as

well. It can be shown for the first three low-order modes ( $\mathbf{J}_1 - \mathbf{J}_3$ ) that the modal electric  $Q_{\text{eig},n}^{\text{el}}$  are higher than the modal magnetic  $Q_{\text{eig},n}^{\text{mag}}$ . This can be explained by the slope of the eigenvalues curve around the resonances, as shown in Fig. 5-1 (left). The curves below the resonance have a higher derivative as above the resonance which results mostly in  $Q_{\text{eig},n}^{\text{el}} > Q_{\text{eig},n}^{\text{mag}}$ . This means below and in the resonance the radiation efficiency can be high, but results in a narrower radiation bandwidth. However, above the resonance the radiation bandwidth becomes broader.

The slope of eigenvalue curve  $\mathbf{J}_4$  has nearly the same low derivative around the modal resonance (see Fig. 5-1 right) and results to  $Q_{\text{eig},4}^{\text{el}} \approx Q_{\text{eig},4}^{\text{mag}}$ . Comparing the quality factors to each other, the  $Q_{\text{eig},n}^{\text{el}}$  decreases with higher mode order, whereas  $Q_{\text{eig},n}^{\text{mag}}$  is different and no characteristic behavior can be detected. The trend of the resultant  $Q_{\text{eig},n}$  shows that the high-order modes have lower values compared to low-order modes and should result in a broader radiation bandwidth. This postulation will be discussed in following sections based on the selective excitation of the first three modes.

## 5.2 Coupling probes for the selective excitation of characteristic modes

As shown in Fig. 5-2, the modal current distributions of the characteristic modes on the rectangular plate are predominantly concentrated along the edges and mainly characterized by a sinusoidal magnitude behavior. The selective excitation of the modes will be implemented on the first three characteristic modes of the PCB. Only the outer edges of the PCB should be used, keeping in mind the practical implementation of antennas on a small handheld device and with a limited form factor [Kiv04].

Fig. 5-4 illustrates the outer edge current distributions of the characteristic modes  $\mathbf{J}_1$ ,  $\mathbf{J}_2$  and  $\mathbf{J}_3$  along the minor and major axes. It shows that each characteristic mode has its current maxima at specific positions in-phase or out-of-phase over the plate. In addition to the

## 5. Selective Excitation of the Characteristic Modes of the Small Rectangular Plate

current distribution, the electric field distribution along the edges are considered. The maxima of the electric field has a phase difference of  $90^\circ$  compared to the maxima of the current. The electric field distribution has its nulls at the peak of the current distribution and vice versa (see Fig. 5-4) [IV, V].

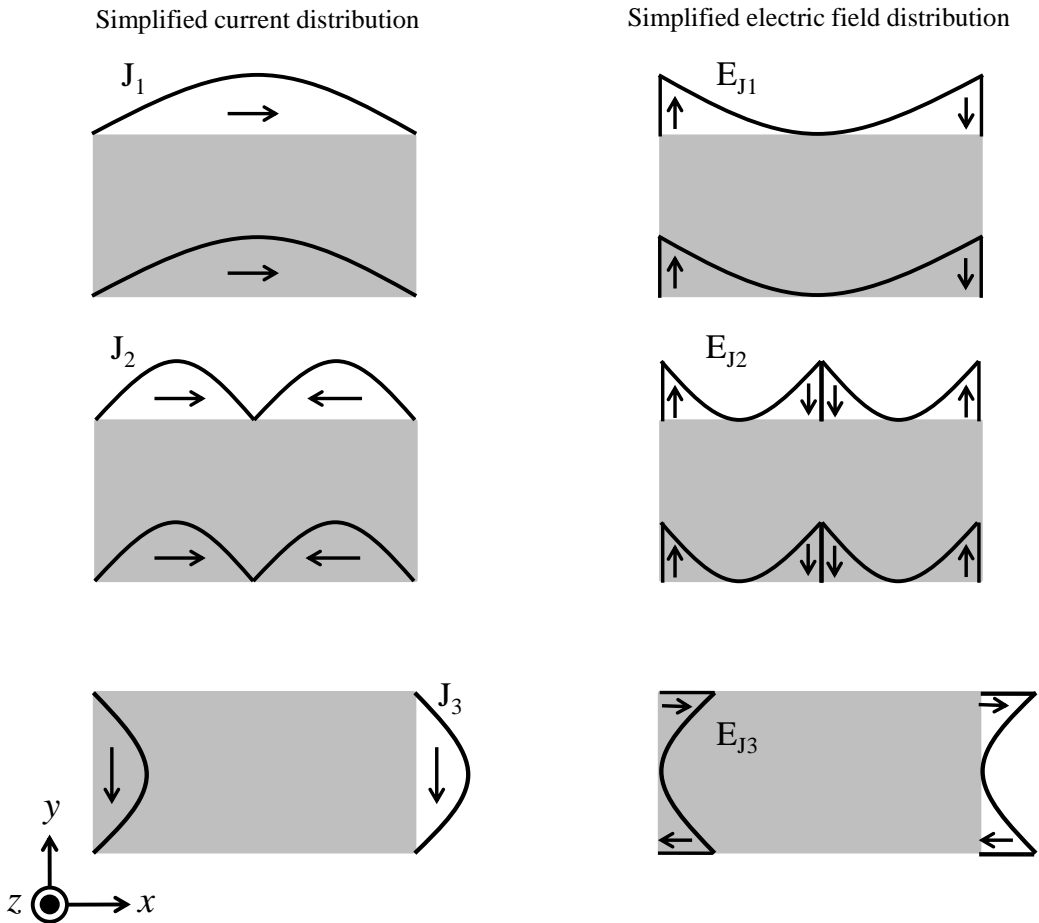


**Fig. 5-4** Simplified current (left) and electric (right) field distribution of mode  $J_1$  (top),  $J_2$  (middle) and  $J_3$  (bottom) of the generic rectangular plate from Fig. 5-1.

It has been shown that a desired mode can be excited by imprinting inductive currents at the maxima of the modal current distribution or by a capacitive coupling in the maxima of the modal electric field distribution [New79, Rah07, Fam07, Van02, IV, V].

All excitations methods will be utilized by using the delta gap excitation over a driving edge as explained in section 3.2 (see Fig. 3-3). Two canonical excitation probes are



## 5.2 Coupling probes for the selective excitation of characteristic modes

needed, having a small form factor (FF). By their small size they are not contributing themselves to the radiation [I, Rah06]. As shown in Fig. 5-5, the inductive probe (IP) can be directly implemented into the PCB structure and can be driven over a given edge element  $l_u$ . On the other side the capacitive probe is designed as a quite small patch (FF:  $8 \text{ mm}^3$ ) on the PCB including the driving edge  $l_u$ . As shown in Fig. 5-5, the IP is indicated with the symbol of an inductance, whereas the CP is represented by a capacitance symbol based on the inductive and the capacitive coupling characteristics of the probes. The arrows close to the symbols show the direction of the imprinted currents over the driving edge  $l_u$ .

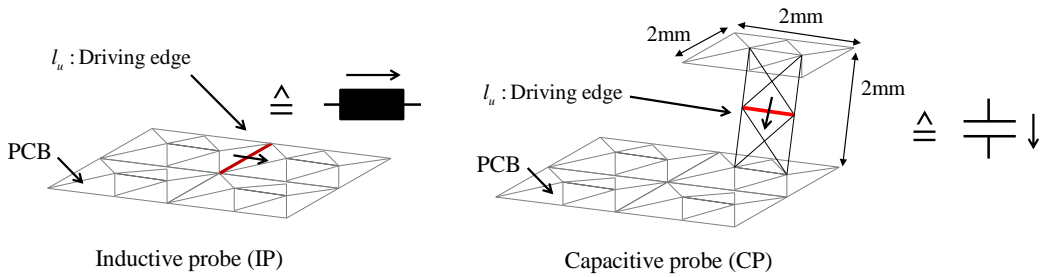


**Fig. 5-5** Definition of the inductive probe IP (left) and the capacitive probe CP (right) for the selective excitation of the characteristic modes.

Based on field distributions in Fig. 5-4, different sets of distributed IP's and CP's are placed at maxima as shown in Fig. 5-6. The CP's are distributed in the electric field maxima, whereas the IP's are distributed in the current maxima of the desired modes [Van02, Vil06, V]. Both concepts guarantee an efficient selective excitation of the given characteristic modes [Van00, Rah06, IV].

Starting with the selective inductive excitation, two inductive probes (IP's) at the current maxima are needed for the desired selective excitation of the modes  $\mathbf{J}_1$  and  $\mathbf{J}_3$ , whereas mode  $\mathbf{J}_2$  needs four IP's to excite the mode selectively. In comparison, four capacitive probes (CP's) at the electric field maxima are needed for the desired selective excitation of the modes  $\mathbf{J}_1$  and  $\mathbf{J}_3$ . However, mode  $\mathbf{J}_2$  needs six CP's to excite the mode in a selective manner.

Additionally to the predefined positions each probe should be driven with the correct amplitude and phase to guarantee the selective excitation of the desired modes as depicted in

## 5. Selective Excitation of the Characteristic Modes of the Small Rectangular Plate

Fig. 5-6. Based on that, Table 5-2 and Table 5-3 shows the required distribution of amplitudes and phases of each configuration that can be employed to excite the desired characteristic modes selectively. The excitation phases depend on the current and electric field distribution in the maxima of the desired mode, as shown in Fig. 5-4. The required excitation amplitudes of the probes can be changed by reducing the amplitudes of terms  $V_u^i$  in the voltage vector  $\mathbf{V}$  (see section 3.2) depending on how many probes are needed. The required phase can be changed by the orientation of the unit vector  $\hat{\mathbf{n}}_{\perp}$  in the required edge elements (see section 3.2).

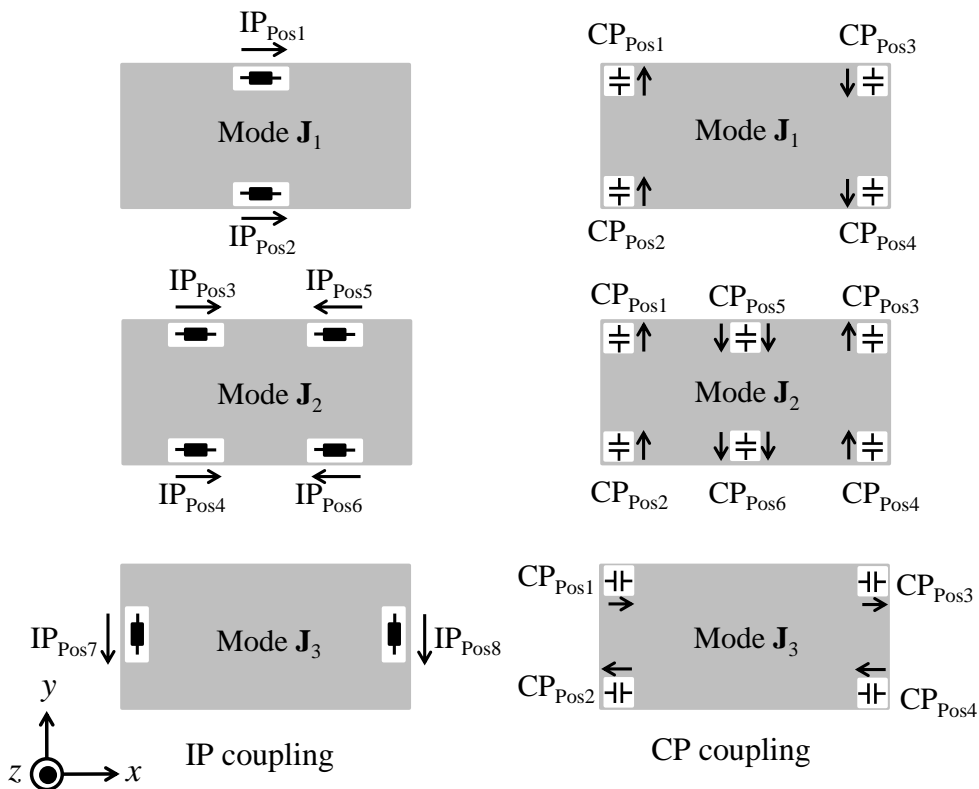


**Fig. 5-6** Selective inductive probe (IP) and capacitive probe (CP) coupling of the mode  $\mathbf{J}_1$  (top),  $\mathbf{J}_2$  (middle) and  $\mathbf{J}_3$  (bottom) of the generic rectangular plate from Fig. 5-1.

As illustrated in Fig. 5-6 the selective inductive excitation of mode  $\mathbf{J}_1$  should be achieved by driving both IP's in position 1 ( $\text{IP}_{\text{pos1}}$ ) and 2 ( $\text{IP}_{\text{pos1}}$ ) in-phase. For the inductive excitation of mode  $\mathbf{J}_2$  two of the four probes have to be simultaneously driven in-phase ( $\text{IP}_{\text{pos3}}$  and  $\text{IP}_{\text{pos4}}$ ) and the other two probes have to be driven  $180^\circ$  out-of-phase ( $\text{IP}_{\text{pos5}}$  and  $\text{IP}_{\text{pos6}}$ ).

## 5.2 Coupling probes for the selective excitation of characteristic modes

Mode  $\mathbf{J}_3$  will be excited by driving both inductive probes ( $\text{IP}_{\text{pos7}}$  and  $\text{IP}_{\text{pos8}}$ ) in-phase together.

**Table 5-2** Feeding configuration of the selective inductive coupling of the modes  $\mathbf{J}_1$ ,  $\mathbf{J}_2$  and  $\mathbf{J}_3$ .

	$\text{IP}_{\text{Pos1}}$	$\text{IP}_{\text{Pos2}}$	$\text{IP}_{\text{Pos3}}$	$\text{IP}_{\text{Pos4}}$	$\text{IP}_{\text{Pos5}}$	$\text{IP}_{\text{Pos6}}$	$\text{IP}_{\text{Pos7}}$	$\text{IP}_{\text{Pos8}}$
$\mathbf{J}_1$	$\frac{1}{2}/0^\circ$	$\frac{1}{2}/0^\circ$	-	-	-	-	-	-
$\mathbf{J}_2$	-	-	$\frac{1}{4}/0^\circ$	$\frac{1}{4}/0^\circ$	$\frac{1}{4}/180^\circ$	$\frac{1}{4}/180^\circ$	-	-
$\mathbf{J}_3$	-	-	-	-	-	-	$\frac{1}{2}/0^\circ$	$\frac{1}{2}/0^\circ$

**Table 5-3** Feeding configuration of the selective capacitive coupling of the modes  $\mathbf{J}_1$ ,  $\mathbf{J}_2$  and  $\mathbf{J}_3$ .

	$\text{CP}_{\text{Pos1}}$	$\text{CP}_{\text{Pos2}}$	$\text{CP}_{\text{Pos3}}$	$\text{CP}_{\text{Pos4}}$	$\text{CP}_{\text{Pos5}}$	$\text{CP}_{\text{Pos6}}$
$\mathbf{J}_1$	$\frac{1}{4}/0^\circ$	$\frac{1}{4}/0^\circ$	$\frac{1}{4}/180^\circ$	$\frac{1}{4}/180^\circ$	-	-
$\mathbf{J}_2$	$\frac{1}{6}/0^\circ$	$\frac{1}{6}/0^\circ$	$\frac{1}{6}/0^\circ$	$\frac{1}{6}/0^\circ$	$\frac{1}{6}/180^\circ$	$\frac{1}{6}/180^\circ$
$\mathbf{J}_3$	$\frac{1}{4}/0^\circ$	$\frac{1}{4}/180^\circ$	$\frac{1}{4}/0^\circ$	$\frac{1}{4}/180^\circ$	-	-

In contrast to the inductive coupling, due to more electric field maxima the capacitive coupling needs more locations for the selective excitation, as visualized in Fig. 5-6. Table 5-3 shows the excitation of mode  $\mathbf{J}_1$  and  $\mathbf{J}_3$  where two of the four probes CP's have to be driven in-phase ( $\mathbf{J}_1$ :  $\text{CP}_{\text{Pos1}}$  and  $\text{CP}_{\text{Pos2}}$ ,  $\mathbf{J}_3$ :  $\text{CP}_{\text{Pos1}}$  and  $\text{CP}_{\text{Pos3}}$ ) and the other two probes have to be driven in  $180^\circ$  out-of-phase ( $\mathbf{J}_1$ :  $\text{CP}_{\text{Pos3}}$  and  $\text{CP}_{\text{Pos4}}$ ,  $\mathbf{J}_3$ :  $\text{CP}_{\text{Pos2}}$  and  $\text{CP}_{\text{Pos4}}$ ). In general the mode  $\mathbf{J}_2$  normally needs for the selective excitation 8 CP's (see Fig. 5-4), but two of the probes in the middle of the major edge (see Fig. 5-6) can be combined to one probe ( $\text{CP}_{\text{Pos5}}$  and  $\text{CP}_{\text{Pos6}}$ ) driven  $180^\circ$  out-of-phase together. Here the phases of the electric field maxima in the middle of the edges coincide and can be therefore combined to one coupling

## 5. Selective Excitation of the Characteristic Modes of the Small Rectangular Plate

location (compare Fig. 5-4 and Fig. 5-6). The four outer probes ( $CP_{Pos1} - CP_{Pos4}$ ) should be driven in-phase together.

In order to evaluate how purely the desired modes can be excited the normalized coefficients of each mode  $|b_n|^2$  (4.14) are calculated and the percentage contribution to the total radiation power is evaluated.

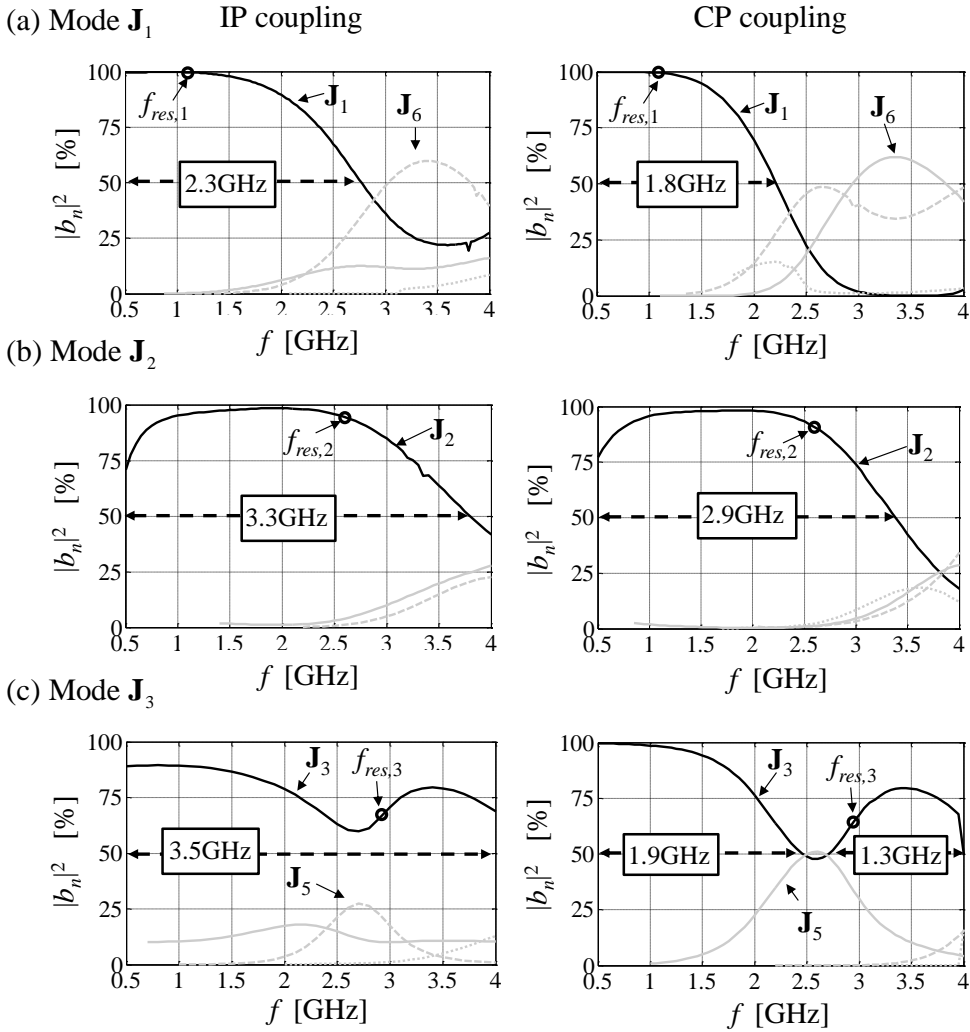


**Fig. 5-7** Percentage contribution by the selective IP coupling (left) and CP coupling (right) of the characteristic modes  $J_1$  (a),  $J_2$  (b) and  $J_3$  (c).

Fig. 5-7 shows the related contributions of the desired mode excitation (black curves) in all configurations and visualizes the differences between the selective inductive (left side)

and capacitive (right side) coupling. The excitation of the desired modes will be analyzed by the half-power contribution ( $|b_n|^2 \geq 50\%$ ) to the total radiation as a figure of merit.  $\Delta_{IP}$  and  $\Delta_{CP}$  denote the achieved half-power contribution bandwidth. Excited modes with less than  $|b_n|^2 \leq 10\%$  power contribution are neglected in the investigation. Please notice, this coefficient does not include the power delivered to the antenna (mismatch losses) and does not reveal anything about the achievable radiation bandwidth, but gives a fair measure about how purely a single mode can be excited.

Fig. 5-7 shows that the desired modes can be excited separately either by the inductive or the capacitive probes. In addition, we are able to show that the three sets of inductive probes offer advantages over the capacitive probes in terms of the selective coupling of specific characteristic modes. The percentage power contribution of the selective inductive coupling of mode  $\mathbf{J}_1$ ,  $\mathbf{J}_2$  and  $\mathbf{J}_3$  can be enhanced up to  $\Delta_{IP,1} = 2.3\text{GHz}$ ,  $\Delta_{IP,2} = 3.3\text{GHz}$  and  $\Delta_{IP,3} = 3.5\text{GHz}$  frequency ranges respectively. While the percentage power contribution of the selective capacitive coupling results in smaller frequency ranges. An additional result is that an inductive coupling offers advantages over the capacitive coupling in exciting the desired modes far from their eigenresonances  $f_{res,n}$ .

In order to show the ability of selective mode coupling we will evaluate concepts by using more practical coupling elements instead of the probes.

### 5.3 Evaluation of different coupling elements

A non-resonant coupling element at which we are looking should efficiently excite the desired characteristic mode on a PCB without contributing to the radiation in the observed frequency range of  $0.5 \leq f[\text{GHz}] \leq 4$ . Therefore, different non-resonant coupling elements are discussed in order to evaluate which element have heavy effect on the desired mode excitation. The predefined locations of the first three desired characteristic modes (see Fig. 5-6) and their previously discussed current and electric field distributions (see Fig. 5-4) are the basis of the coupling element discussion.

## 5. Selective Excitation of the Characteristic Modes of the Small Rectangular Plate

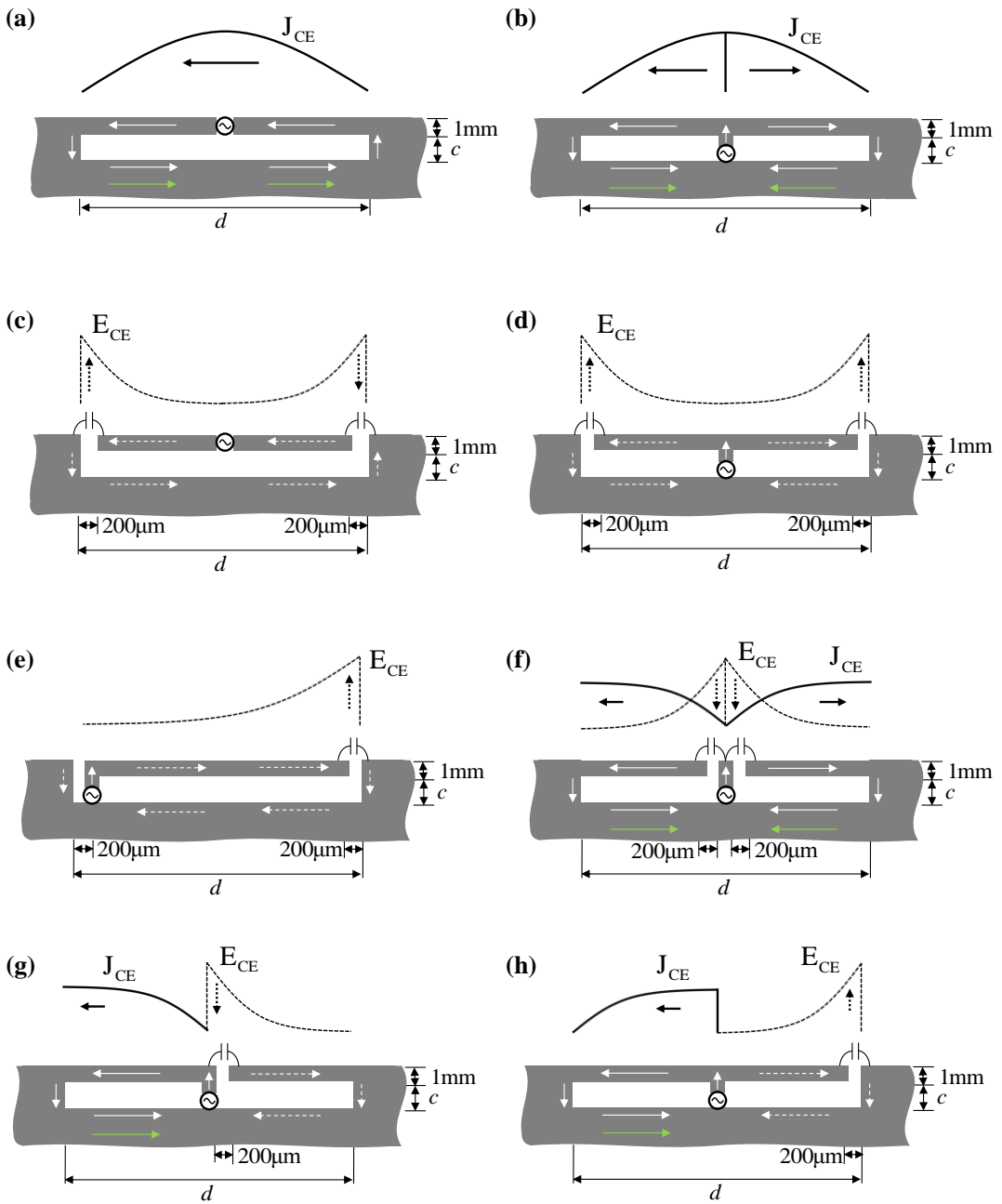


**Fig. 5-8** Eight different co-planar and integrated coupling elements at the edge of a half-infinite PCB. (Inductive element with one loop track (a) and two loop tracks (b), capacitive element with an out-of-phase (c) and in-phase coupling (d), inverted L-shape element (e), capacitive feed element (f), inductive loop element with capacitive feed location (g) and inverted F-shape element (h))

Several candidates for coupling elements are designed, with a few important criteria: All

elements should have the same overall dimensions (FF: form factor) to facilitate fair comparison, they should be integrable to the edges and/or corners of the PCB, and they should not be resonant in the observed frequency range. Since the goal of the investigation is to excite chassis modes only, resonant coupling element candidates will be discarded from further discussion.

Eight generic coplanar coupling element designs are shown in Fig. 5-8. All elements are implemented on the edge of a semi-infinite PCB in order to reduce the influence of the PCB dimensions and the excitation of the current and/or electric field distributions. Ideally, these boundary condition absorb all outgoing waves that hit the outer boundary [Gus06], as shown in Fig. 5-9. Therefore, only the physical behavior of the coupler itself will be tested, without the chassis influence.

As shown in Fig. 5-8, the widths of all outer tracks and/or folded arms are fixed to 1 mm and all small gaps in the structure are fixed to  $200\mu\text{m}$ . Only the overall distance  $d$  and the gap  $c$  between the outer track and the PCB are considered as variables. Furthermore, all estimated current and electric field distributions ( $J_{\text{CE}}$  and  $E_{\text{CE}}$ ) and imprinted currents on the PCB are schematically shown in the depicted generic coupling elements in Fig. 5-8.

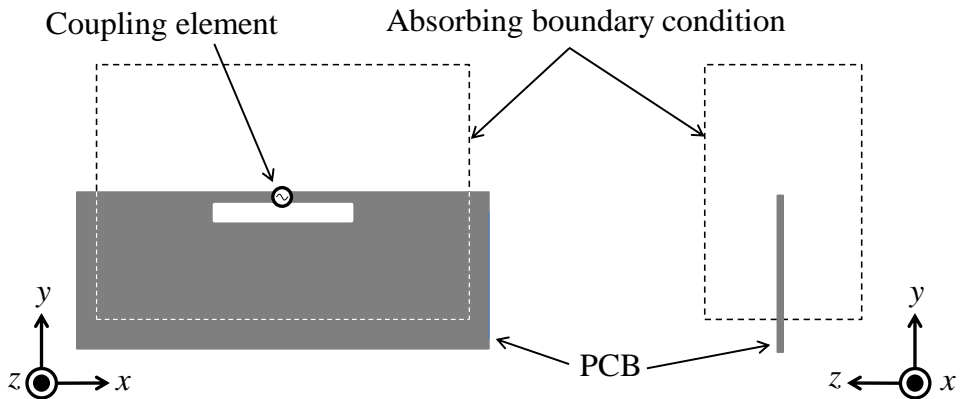










**Fig. 5-9** Semi-infinite PCB in an absorbing boundary condition (ABC).

In order to make a fair comparison of all elements four different form factors (FF's) depending on the fixed dimensions (see Fig. 5-8) and the two variable parameters  $c$  and  $d$  are calculated, as shown in Table 5-4. The resultant input impedance  $Z_{\text{in,CE}}$  of the coupling elements is decomposed into real and imaginary parts ( $\text{Re}\{Z_{\text{in,CE}}\}$  and  $\text{Im}\{Z_{\text{in,CE}}\}$ ) in order

## 5. Selective Excitation of the Characteristic Modes of the Small Rectangular Plate

to discuss the frequency-dependent impedance behavior based on the self-resonances of the structures ( $\text{Im}\{Z_{\text{in,CE}}\}=0$ ). For a clear understanding of the analysis the  $\text{Re}\{Z_{\text{in,CE}}\}$  are marked in black and  $\text{Im}\{Z_{\text{in,CE}}\}$  are marked in grey having different shading of the curve depending on the different form factors, as shown in Table 5-4.

**Table 5-4** Valuable parameter and their resultant form factor and legend keys.

$c$ [mm]	$d$ [mm]	area [mm <sup>2</sup> ]	$\text{Re}\{Z_{\text{in,CE}}\}$	$\text{Im}\{Z_{\text{in,CE}}\}$
1	20	FF-1 = 40		
2	20	FF-2 = 60		
1	30	FF-3 = 60		
2	30	FF-4 = 90		

### 5.3.1 Inductive loop and double loop coupling element

Fig. 5-8 a and b show a one-loop element and a double-loop element. The concept of these elements is based on the assumption that a current imprinted by the source on the loop paths are identical on both sides (the outer rod and the opposite part on the PCB) if the loops are electrically small compared to the operation wavelength, i.e.  $d \ll \lambda$ . Due to the close vicinity between the outer tracks and the plate ( $c \ll d$ ) the fields and currents around the slit cancel almost entirely at large distances. However, the imprinted current on the PCB spread wider on the plate and excite the modal distribution  $J_n$  in-phase (element a) or out-of-phase (element b) on the plate itself by the element currents  $J_{\text{CE}}$  (green arrows) [I, II, V]. This little current portion will contribute to the radiation fields at large distances by coupling with the characteristic modes  $J_n$ . The impedance behavior of these coupling structures are shown in Fig. 5-10 a and b. The input impedances of both elements underline the highly inductive behavior based on the high imaginary part ( $\text{Im}\{Z_{\text{in,CE}}\} > 0$ ) of the input-impedance  $Z_{\text{in,CE}}$ . As shown in Fig. 5-10 a and b, a non-resonant behavior with all four different form factors (FF-1 – FF-4) can be achieved over the observed frequency range. Comparing the elements with each other, by increasing the FF the elements results in a higher radiation resistance and starts to radiate for FF-3 and FF-4. The  $\text{Im}\{Z_{\text{in,CE}}\}$  also



increases because the current path around the element become electrically longer and results in a phase shift in high frequency.

Due to the direct inductive in-phase (a) and out-of-phase (b) current coupling loops, these elements can be seen as non-resonant *inductive coupling elements* (ICE) with an even (in-phase) and odd (out-of-phase) current mode character.

### 5.3.2 Dipole and T-shape coupling element

The concepts in Fig. 5-8 c and d are based on the assumption that an electric field distribution couples in an odd (out-of-phase) and even mode (in-phase) with the PCB respectively. Example c consist of a very small *PCB-integrated dipole* along the edges and generates an out-of-phase electric field distribution  $E_{CE}$  at the ends of the dipole rods (marked as capacitances). The element d is a *PCB-integrated T-shape element* and generates an in-phase electric field distribution  $E_{CE}$  at the ends of the T-shape rod (also marked as capacitances). Therefore, we expect that an equiphase electric field distribution  $E_n$  of the characteristic modes  $\mathbf{J}_n$  on the PCB can be excited by such coupling element structures. The calculated input impedances of the elements c and d at the frequency range of  $0.5 \leq f [\text{GHz}] \leq 4$  are presented in Fig. 5-10 c and d. It shows that both elements are highly capacitive ( $\text{Im}\{Z_{in,CE}\} < 0$ ).

It can be seen that the element c with the FF-1 – FF-3 and element d with the FF-1 - FF-2 are non-resonant and will not significantly contribute to the fields in large distances. Due to the electrically short dimensions both elements present a quite low radiation resistance (low  $\text{Re}\{Z_{in,CE}\}$ ) over the observed frequency range and will not radiate if these elements are used for the mode coupling. In addition, due to the lower slopes of the  $\text{Im}\{Z_{in,CE}\}$  curves the capacitive coupling of element d will be decreased at high frequency and become more inductive.

Due to the direct capacitive coupling having in-phase (d) and out-of-phase (c) behavior at the outer arms, these elements can be seen as non-resonant *capacitive coupling elements* (CCE) with an even (in-phase) and odd (out-of-phase) electric field character.

## 5. Selective Excitation of the Characteristic Modes of the Small Rectangular Plate

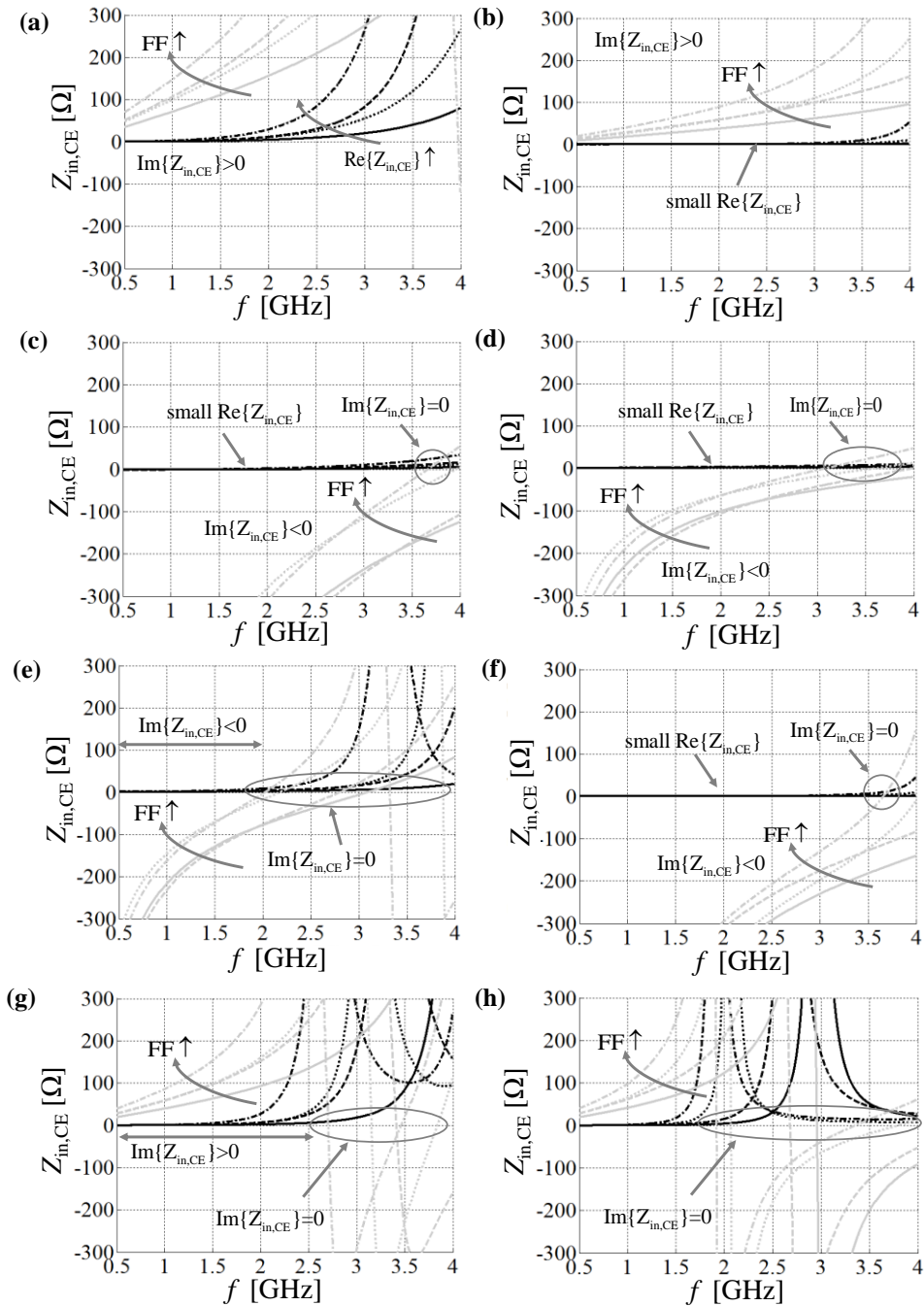


**Fig. 5-10** Input-impedance behaviors of the inductive element with one loop track (a) and two loop tracks (b), capacitive element with an out-of-phase (c) and in-phase coupling (d), inverted L-shape element (e), capacitive feed element (f), inductive loop element with capacitive feed location (g) and inverted F-shape element (h) investigated with four different form factors (FF-1-4). The legend is shown in Table 5-4.

### 5.3.3 Inverted-L coupling element

The resonant inverted-L antenna has been extensively analyzed in the literature, e.g. in [Fuj01, Kin60]. In this investigation we are looking for a non-resonant *PCB-integrated L-shape element*. The input impedance analysis of the investigated L-shaped coupling element (Fig. 5-10 e) has demonstrated that the element has a resonance within the observed frequency range for all investigated form factors. This element is therefore not suitable for examining the chassis mode coupling. In order to have such an element with acceptable properties, an additional inverted-L coupling element is created with half the length of FF-1, as shown in Fig. 5-11 (right). With shorter electrical length, i.e.  $d = 10\text{mm}$ , this structure with FF-0 is expected to be non-resonant in the observed frequency range. The simulated input-impedance is presented in Fig. 5-11 (right). As expected, a non-resonant behavior of the inverted-L shape element is achieved with highly capacitive impedance ( $\text{Im}\{Z_{\text{in,CE}}\} < 0$ ). This means the element is a good candidate for placing it in a maximum of the equiphase electric field distribution  $E_n$  of the characteristic modes  $\mathbf{J}_n$  on the PCB.

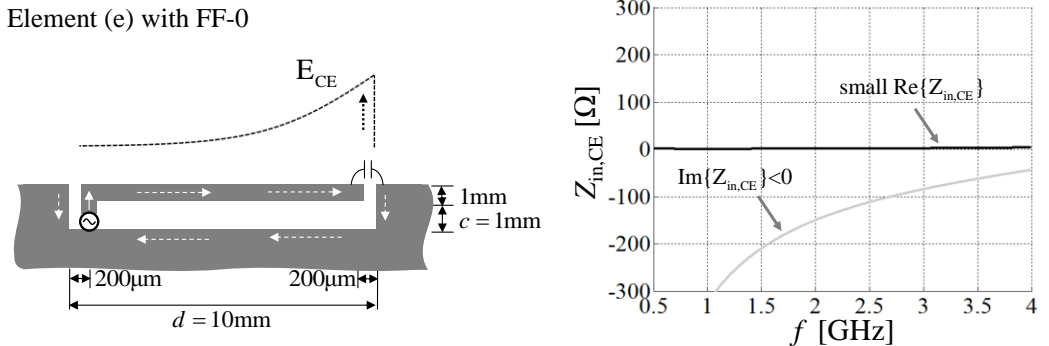


**Fig. 5-11** Input-impedance behavior of the inverted-L shape element (e) with FF-0 ( $d = 10\text{mm}$ ,  $c = 1\text{mm}$ ).

Due to the direct capacitive coupling of the inverted-L shape arm and the quite easy PCB implementation, this element can also be classified as a non-resonant *capacitive coupling element* (CCE).

### 5.3.4 Capacitive feed coupling element

The next element is a *PCB-integrated capacitive feed element* (see Fig. 5-8 f). This kind

## 5. Selective Excitation of the Characteristic Modes of the Small Rectangular Plate

---

of element consists of two symmetric folded arms directly oriented to the feed point and reacts as high capacitive load. In addition, such a capacitive load generates a high in-phase electric field distribution  $E_{CE}$  around the feed point itself. The gap between the arms and the short feed point is  $200\mu\text{m}$ . This value is highly sensitive to the antenna impedance and could be additionally used as a variable to optimize the impedance matching. But for a fair comparison to the other structures only the parameters  $c$  and  $d$  are used to tune the element performances with respect to the input impedance. It is shown in Fig. 5-10 f that only the element with the FF-4 goes into resonance. As predicted, the input impedance of the element shows a highly capacitive input reactance over the observed frequency confirming the capacitive behavior of the described element in Fig. 5-8 f. In addition, the small input resistance also indicates a non-resonant behavior of the elements (FF-1 - FF-3).

Due to the capacitive feed-point coupling this element can be seen as a non-resonant *capacitive feed coupling element* (CFCE) and expand the classification of the CCEs.

### 5.3.5 Loop element including a parasitic capacitive feed capacitance

Fig. 5-8 g shows a *PCB-integrated loop element with a parasitic feed capacitance*. This design is therefore a hybrid between the already explained elements b and f. For small form factors the resulting input impedances in Fig. 5-10 g mainly result in anti-resonances, which means that this element stores the energy in the structure itself. Only the element with the FF-1 shows non-resonant behavior over the observed frequency and is of general interest for further discussions for the characteristic modes excitation. The element itself consists of one loop track (left side) which generates an in-phase coupling with the modal distribution  $J_n$ , whereas the other track (right side) generates an electric field distribution  $E_{CE}$  around the feed point due to the optimized gap of  $250\mu\text{m}$ . Both together present (see FF-1) an inductive input reactance ( $\text{Im}\{Z_{in,CE}\} > 0$ ) with an increased input resistance compared to the elements b and f.

Due to the capacitive and inductive coupling this element can be seen as a non-resonant *hybrid coupling element* (HCE) and expand the classification of both the CCEs and ICEs.

### 5.3.6 Loop element including a capacitive track

The last element h is a *PCB-integrated small inverted-F element*. The classical inverted-F antenna has been extensively analyzed in the literature, e.g. in [Fuj01, Kin60]. Here, this element has been investigated as a hybrid between the already explained elements b and d. The element itself consists of one loop track (left side) which generates an in-phase coupling with the modal distribution  $J_n$ , whereas the other track (right side) generates an electric field distribution  $E_{CE}$  in the gap (200 $\mu\text{m}$ ) between the outer track and the PCB. In comparison to the elements b and d (see Fig. 5-10 b and d) the element h results in resonances and anti-resonance and heavily contributes to the radiation or store the energy in the element itself (see Fig. 5-10 h). The investigation of this hybrid shows that this kind of element is unsuitable for further discussions based on its own impedance behavior. For the practical antenna design, this element could be a good choice, but here the investigation concentrates on the selective excitation of the chassis modes, as previously mentioned.

But due to the capacitive and inductive coupling this element can be seen as a resonant *hybrid coupling element* (HCE).

### 5.3.7 Selection of the elements for the selective excitation of the desired modes

Next, we will include the rectangular plate with the familiar dimensions of 120  $\times$  60 mm<sup>2</sup> in the investigation. Based on the current distribution of the plate in Fig. 5-4, we can see that only the ICE (see Fig. 5-8 a) can be arranged in all maxima of the characteristic modes with correct phasing [I, II, V]. An additional feeding network is needed to deal with the desired phases at the distributed positions [III, V]. The out-of-phase inductive element b, as shown in Fig. 5-8 b, is not suitable for the selective excitation, because no out-of-phase modal current distribution occurs in observing current maxima of the first three modes as shown in Fig. 5-4 left.

By observing the respective electric field distributions of the modes  $E_n$  (see Fig. 5-4 right) it can be seen that the PCB-integrated L-shape element (see Fig. 5-11) will be the best candidate to distribute this element on the outer edges of the PCB where the maxima of the field distributions occur [II]. We should keep in mind to adjust the right phases of the elements in order to excite the electric field distributions of the respective modes as shown

## 5. Selective Excitation of the Characteristic Modes of the Small Rectangular Plate

---

in the canonical patch excitation (Fig. 5-6 right) [II, III]. The excitation of the combined equiphase electric field distribution of the mode  $\mathbf{J}_2$  (especially in the middle of the major edges) can be realized by using:

- i. two T-shape CCEs,
- ii. two CFCEs,
- iii. four L-shape CCEs.

The next two sections will show the results of the selective excitation and will prove how efficiently the power is directed into a specific mode of the rectangular plate based on the chosen elements at the predefined locations. Based on the non-resonant impedance behavior of the coupling element it is proven that additional matching circuits can tune the input-impedance to the desired operation frequency band.

### 5.4 Selective capacitive coupling of the characteristic modes by using non-resonant CCEs

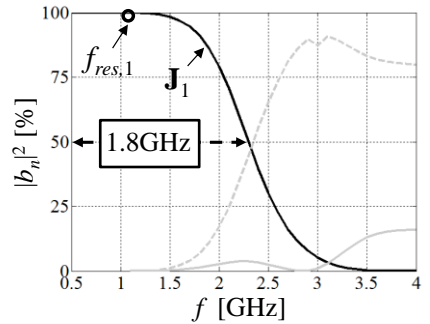
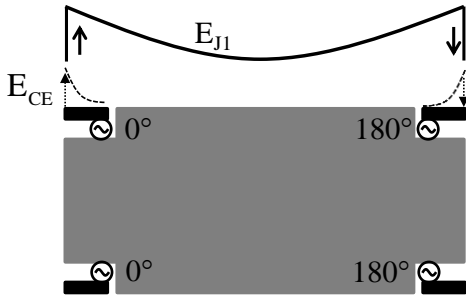
Based on the discussion in the previous section, the PCB-integrated L-shape element having the FF-0 (see Fig. 5-11) can be quite nicely used as a set of four distributed elements in order to excite the modes  $\mathbf{J}_1$ ,  $\mathbf{J}_3$  and  $\mathbf{J}_2$  (see Fig. 5-12) [II]. Each set of CCE's should be driven in the correct phases at the corners of the PCB at the electric field distribution maxima. The positions, the amplitudes and the phases of the CCE's are given by the capacitive probe investigation as shown in Table 5-2. As depicted in the Fig. 5-12 (left), for the selective excitation of mode  $\mathbf{J}_1$  and  $\mathbf{J}_3$  two of the four CCEs have to be driven in-phase ( $\mathbf{J}_1$ :  $\text{CCE}_{\text{Pos1}}$  and  $\text{CCE}_{\text{Pos2}}$ ,  $\mathbf{J}_3$ :  $\text{CCE}_{\text{Pos1}}$  and  $\text{CCE}_{\text{Pos3}}$ ) and the other two CCEs have to be driven in  $180^\circ$  out-of-phase ( $\mathbf{J}_1$ : the  $\text{CCE}_{\text{Pos3}}$  and  $\text{CCE}_{\text{Pos4}}$ ,  $\mathbf{J}_3$ :  $\text{CCE}_{\text{Pos2}}$  and  $\text{CCE}_{\text{Pos4}}$ ). The mode  $\mathbf{J}_2$  needs for the selective excitation eight CCEs, but as a reference the selective excitation of mode  $\mathbf{J}_2$  starts with four CCEs, one at each corner. All four CCE's have to be driven in-phase together ( $\text{CCE}_{\text{Pos1}} - \text{CCE}_{\text{Pos4}}$ ), as shown in Fig. 5-12 (left-middle).

In addition, the normalized coefficient of each mode  $|b_n|^2$  (see section 4.3.1) is calculated in order to evaluate the contribution of the desired mode coupling by the sets of CCEs.

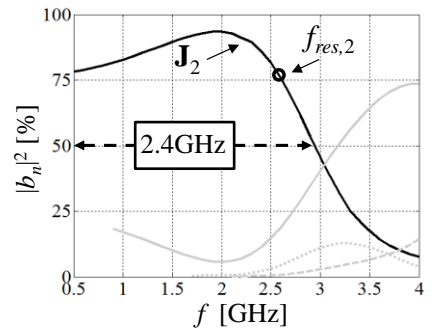
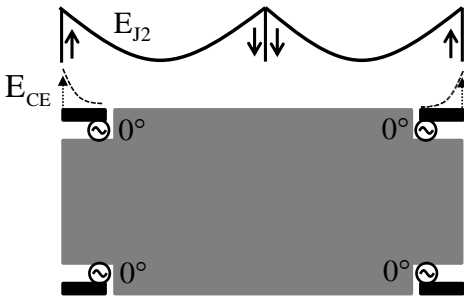
As previously explained, the excitation performance of the desired modes is analyzed by

the half power contribution bandwidth to the overall radiation. Excited modes with a coefficient of  $|b_n|^2 \leq 10\%$  power contribution over the observed frequency range are neglected due to their low relative contribution and are not illustrated in Fig. 5-12.

Mode  $J_1$  Excitation



Mode  $J_2$  Excitation



Mode  $J_3$  Excitation

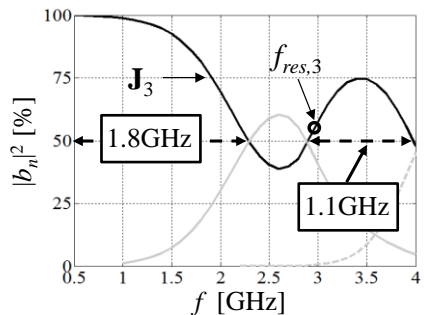
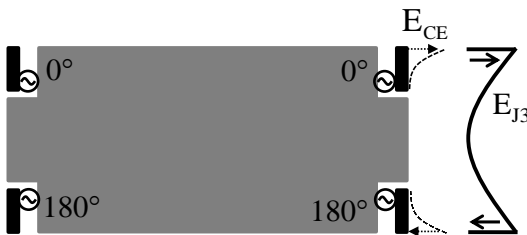


**Fig. 5-12** Configurations for the selective capacitive coupling and the resulting percentage contribution of the characteristic modes  $J_1$  (top),  $J_2$  (middle) and  $J_3$  (bottom).

A comparison of the selective coupling by using CPs (see Fig. 5-7) and by using CCEs

## 5. Selective Excitation of the Characteristic Modes of the Small Rectangular Plate

---

(see Fig. 5-12) reveals that essentially the same modes are excited with very similar results. In detail, the mode  $\mathbf{J}_1$  has the same and mode  $\mathbf{J}_3$  has nearly the same percentage power contribution to the overall radiation. The selective excitation of mode  $\mathbf{J}_2$  by only using four CCEs results to  $\Delta_{\text{CCE}} = 2.4\text{GHz}$  (see Fig. 5-12). This lies clearly under the power contribution range of the canonical coupling with  $\Delta_{\text{CP}} = 2.9\text{GHz}$  (see Fig. 5-7), where six CP's are used.

In order to improve the selective excitation of mode  $\mathbf{J}_2$  additional elements are used to distribute the additional elements  $\text{CP}_{\text{pos5}}$  and  $\text{CP}_{\text{pos5}}$  in the middle of the major axis. Based on the electric field distribution of mode  $\mathbf{J}_2$  in Fig. 5-4 (middle) it is clear that the excitation in the middle of the major edge needs to be symmetrical.

Here, the following elements will be used to enhance the desired power contribution of the mode  $\mathbf{J}_2$ :

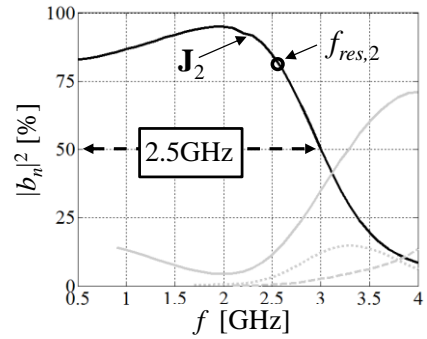
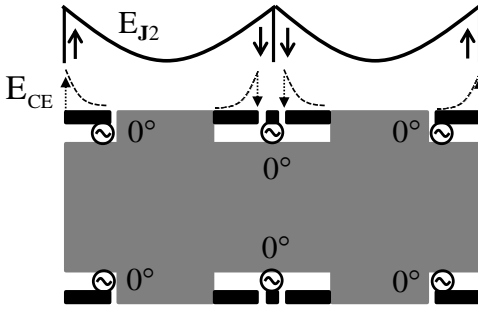
- i. Two capacitive feed elements with FF-1 are used, both CFCE are driven in-phase together (see Fig. 5-13 top).
- ii. Two T-shape coupling elements with FF-1 are used, both CCEs are driven out-of-phase together (see Fig. 5-13 middle).
- iii. Four L-shape elements with FF-0 are used, all CCEs are driven out-of-phase together (see Fig. 5-13 bottom).

As shown in Fig. 5-13 (right), all three cases increase the percentage power contribution of the selective mode  $\mathbf{J}_2$  coupling in the observed frequency range. Case ii with  $\Delta_{\text{CCE}} = 2.8\text{GHz}$  and case iii with  $\Delta_{\text{CCE}} = 2.75\text{GHz}$  are close to the half power contribution of the canonical case with  $\Delta_{\text{CC}} = 2.9\text{GHz}$  (see Fig. 5-7).

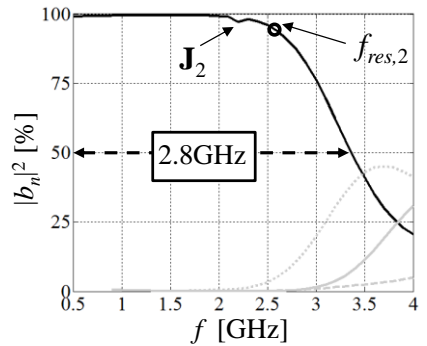
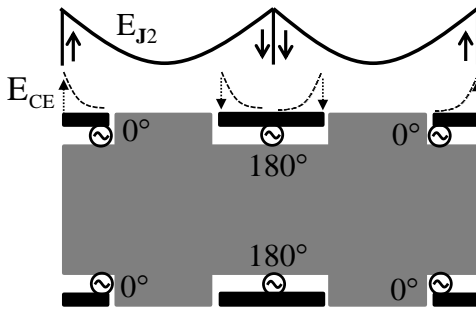
Comparing the selective excitation of all three desired modes by using distributed non-resonant capacitive coupling elements against the canonical capacitive excitation essentially the same effective power contribution to the radiation can be achieved.



Mode  $J_2$  Excitation – Case i



Mode  $J_2$  Excitation – Case ii



Mode  $J_2$  Excitation – Case iii

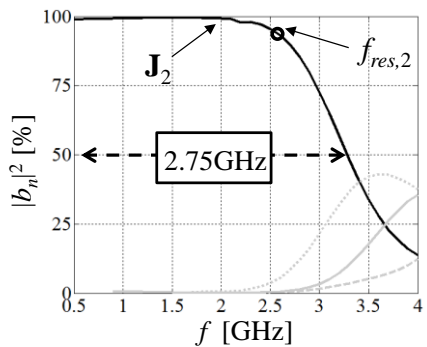
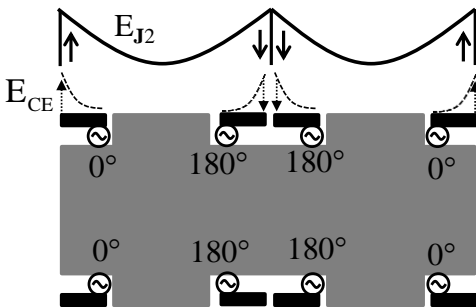


**Fig. 5-13** Configurations for the selective capacitive coupling and the resulting percentage contribution of the characteristic mode  $J_2$  using four CCEs plus two CFCE (top), by using six CCEs (middle) and by using eight CCEs (bottom).

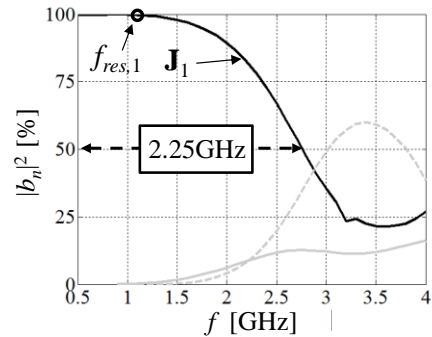
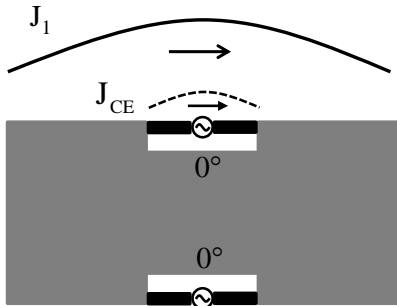
## 5.5 Selective inductive excitation of the characteristic modes by using non-resonant ICES

Based on the results of the canonical IP coupling (see Fig. 5-7), the ICE (Fig. 5-8 (a))

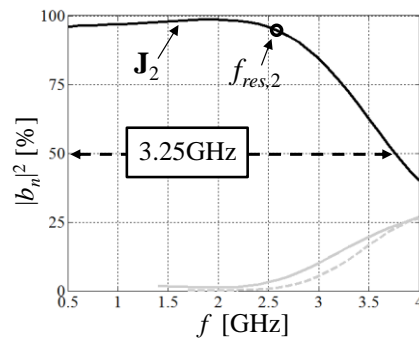
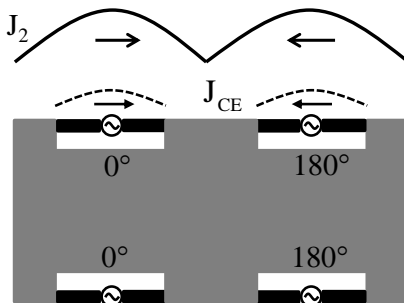
## 5. Selective Excitation of the Characteristic Modes of the Small Rectangular Plate

having the form factor of FF-1 for the selective inductive excitation of the modes  $\mathbf{J}_1$ ,  $\mathbf{J}_2$  and  $\mathbf{J}_3$  is used.

### Mode $\mathbf{J}_1$ Excitation



### Mode $\mathbf{J}_2$ Excitation



### Mode $\mathbf{J}_3$ Excitation

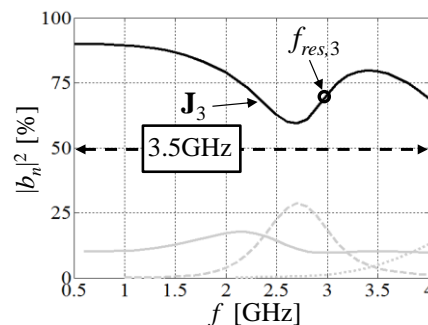


**Fig. 5-14** Configurations for the selective inductive coupling and the resulting percentage contribution of the characteristic modes  $\mathbf{J}_1$  (top),  $\mathbf{J}_2$  (middle) and  $\mathbf{J}_3$  (bottom).

The small PCB-integrated ICEs are mounted at the edges of the PCB at locations where the maxima of the current distributions appear. The used configurations are shown in Fig. 5-14. The excitation of mode  $\mathbf{J}_1$  is achieved by exciting both ICEs in-phase together. For

### 5.5 Selective inductive excitation of the characteristic modes by using non-resonant ICEs

the excitation of mode  $\mathbf{J}_2$  two of the four ICEs have to be excited in-phase and the other two have to be driven out-of-phase together. Mode  $\mathbf{J}_3$  is excited by driving both ICEs in-phase together.

In order to evaluate how purely the desired modes can be excited the normalized coefficient  $|b_n|^2$  of each mode is calculated in Fig. 5-14 (right). The results are very similar to those in Fig. 5-7 where the canonical excitation were used. The bandwidth of the half-power contribution is broad in both inductive coupling cases.

An important result obtained is that the selective inductive coupling by using ICEs offers clear advantages over the selective capacitive coupling by using CCEs (compare Fig. 5-12 to Fig. 5-14). The desired modes can be excited outside of their eigenresonance regions, as shown in Fig. 5-14. In addition, for the selective excitation of modes  $\mathbf{J}_1$  and  $\mathbf{J}_3$  only two ICEs and for the mode  $\mathbf{J}_2$  only four ICEs are needed, while four CCEs are required for the selective capacitive coupling. This suggests to utilize a set of ICEs at the maxima of the modal current distributions to excite the desired characteristic mode  $\mathbf{J}_n$ . This approach can easily be extended to higher order characteristic modes like  $\mathbf{J}_4$  -  $\mathbf{J}_6$  (Fig. 5-2).

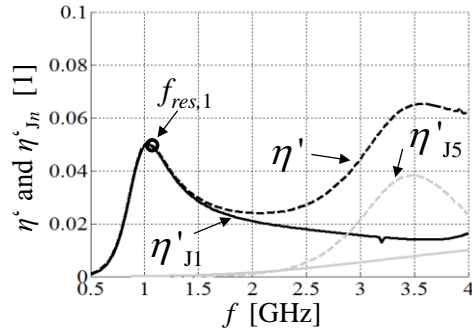
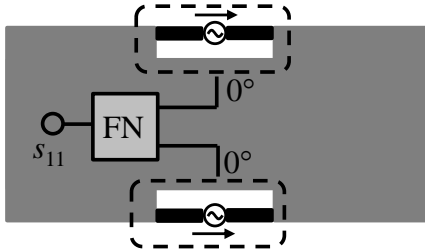
The respective power coefficients given by (4.17) are calculated to further illustrate the effect of the selective excitation. The modal power coefficients  $\eta'_{jn}$  show that the desired modes contribute significantly to the radiation in the observed frequency range. Furthermore, it can be observed that the maxima of the total power coefficient nearly coincide with the eigenresonances of the modes (see Fig. 5-15). The small frequency shifts in the maxima of  $\eta'$  can be explained by the modal  $Q_{\text{eig},n}^{\text{el}}$  and  $Q_{\text{eig},n}^{\text{mag}}$  factors (shown in Table 5-1). Here the slope of the eigenvalue  $|\lambda_n|$  curve plays an important role (see (4.8) - (4.10)). The modal electric quality factor is greater than the respective magnetic quality factors ( $Q_{\text{eig},n}^{\text{el}} > Q_{\text{eig},n}^{\text{mag}}$ ) around the eigenresonances, which results in a higher power coefficient below the resonance. Above the resonance the slope of the  $|\lambda_n|$  curve decreases, resulting in a broadband radiation region.

By using the distributed non-resonant ICE's the modal radiation results in low absolute power delivered to the antenna (less than 10%). This is due to the impedance mismatch,

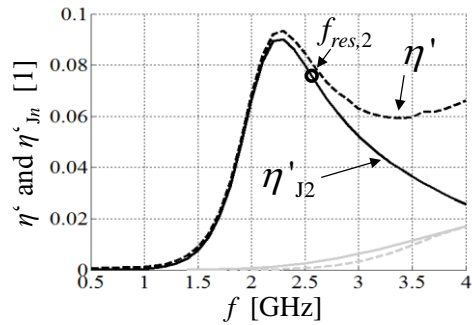
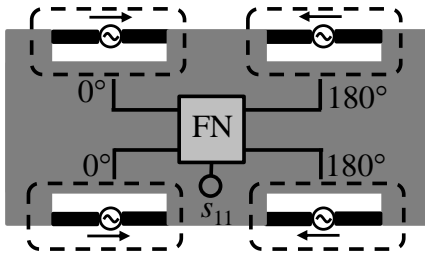
## 5. Selective Excitation of the Characteristic Modes of the Small Rectangular Plate

which results in high reflection coefficients  $|S_{11}|$  and therefore additional matching circuits are needed to match the three configurations to the desired source impedance  $Z_0 = 50\Omega$ .

### Mode $J_1$ Excitation



### Mode $J_2$ Excitation



### Mode $J_3$ Excitation

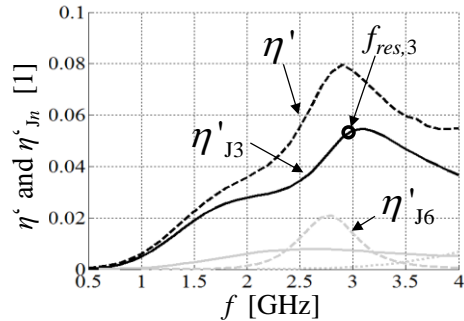
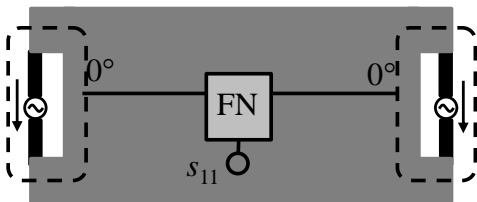


**Fig. 5-15** Configurations for the selective inductive coupling and the resulting power coefficients of the characteristic modes  $J_1$  (top),  $J_2$  (middle) and  $J_3$  (bottom).

The so called (relative) bandwidth potentials  $BW_{rel-J_n}$  can be used to investigate the matchability of the antenna configurations. The parameter expresses the achievable relative bandwidth of an (inherently unmatched) antenna through a lossless two-component 'L-

5.5 Selective inductive excitation of the characteristic modes by using non-resonant ICES section' matching circuit at each frequency [Vil06, Rah09, Val13]. Further bandwidth improvements could be obtained if higher order networks with higher complexity, e.g. T- or  $\Pi$ -section are used [Poz11]. The bandwidth potential gives us an additional figure of merit to compare the impedance bandwidths depending on the desired characteristic mode. There are eight possible network topologies to take into account in the bandwidth potential calculations.

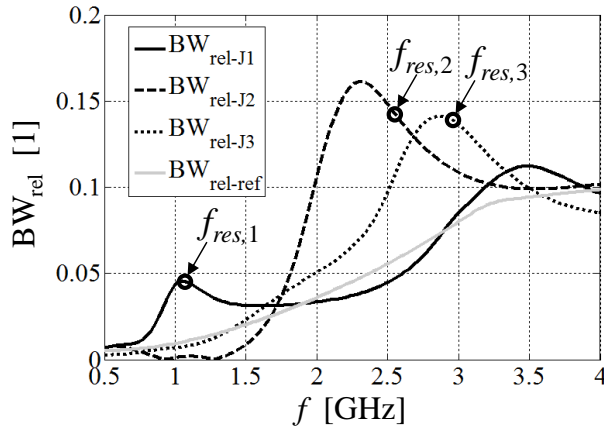


**Fig. 5-16** Calculated relative bandwidth potentials for the selective excitation of the characteristic mode  $J_1$  (black),  $J_2$  (dotted black) and  $J_3$  (dashed black) and one reference ICE (grey) shown in Fig. 5-8 a.

All feasible topologies are calculated and the topologies with the largest available relative bandwidths are selected for the overall evaluation. The calculations assume the typical mobile terminal antenna matching criterion of  $|S_{11}| \leq -6\text{dB}$  or  $|\text{VSWR}| \leq 3$  and should improve the normalized power coefficient due to the increased power transfer to at least  $\eta^* = 75\%$  (lossless circuit).

The relative bandwidth potential of all three configurations are presented in Fig. 5-16. In addition, the bandwidth potential  $\text{BW}_{\text{rel-ref}}$  of the single in-phase ICE implemented on a semi-infinite PCB (see Fig. 5-8 a with a FF-1) is used as a reference value (grey curve).

A comparison of the bandwidth potential curves shows that an improvement to the reference case can be achieved with all three configurations. It shows that at or near the eigenresonances of the desired modes the relative bandwidth potential can be significantly improved. The improvement of  $\text{BW}_{\text{rel-J1}}$  occurs mainly in the lower frequency range around

## 5. Selective Excitation of the Characteristic Modes of the Small Rectangular Plate

---

1.1 GHz and at a higher frequency around 3.5 GHz. At these frequencies the mode  $\mathbf{J}_5$  has the highest percentage power contribution (see Fig. 5-15 right). Both the  $BW_{\text{rel-J2}}$  and  $BW_{\text{rel-J3}}$  result in a broadband improvement to the reference  $BW_{\text{rel-ref}}$ . Summarized, the  $BW_{\text{rel-J1}}$ ,  $BW_{\text{rel-J2}}$  and  $BW_{\text{rel-J3}}$  can essentially be improved in the frequency region of  $0.5 \leq f_{\text{BW,J1}} [\text{GHz}] \leq 1.85$ ,  $1.7 \leq f_{\text{BW,J2}} [\text{GHz}] \leq 3.7$  and  $1.45 \leq f_{\text{BW,J2}} [\text{GHz}] \leq 3.6$  respectively.

The obtained results underline the tuneability of the three configurations. The absolute power delivered to the antenna is increased, if a matching circuit is included between each ICE and the feeding networks (FN) (see Fig. 5-15 left). Different feeding networks for the selective excitation of desired modes on small terminals which includes the matching circuits are evaluated in [III, Had13, Poo14].

# Chapter 6

## Common Excitation of the Characteristic Modes on Small Handheld Devices

By contrast to the selective excitation, where the purity of the modal excitation is desired, this chapter will concentrate on finding principles for common excitation of several characteristic modes. The main target in exciting multiple modes is to achieve a good broadband efficiency for the antenna. The excitation locations are fixed to the outer edges of the rectangular plate due to the space limitation e.g. in handset devices. The investigation starts with testing one probe around the edge and corner of the PCB in order to find an optimal location where the best power coefficient potential can be reached. The same investigation will be made with a combination of two probes distributed around the edge of the PCB. The coupling elements developed in section 5.3 will then be used in the locations where the normalized power coefficient can be maximized. The different excitation strategies will be compared to each other. The investigation will be made in the same observed frequency range of  $0.5 \leq f [\text{GHz}] \leq 4$  as before. Two large capacitive coupling elements will also be used to study the effects of CCE dimensions and feeding point locations on the broadband operation of the CCE antenna. Based on the behavior of the characteristic modes and the CCE resonances, a dual-broadband CCE antenna is demonstrated. The use of the matching circuits is excluded from this investigation, but will be applied in the small antenna design shown in chapter 7.

## 6.1 Common excitation of modes using capacitive coupling or inductive coupling

As shown in chapter 5, the use of combined sets of distributed coupling elements affects significantly the excitation of the characteristic modes. This can be seen in the normalized power coefficient and input impedance of the antenna system, especially around the modal resonances. Promising excitation points on the PCB are investigated in order to maximize the power delivered to the antenna over the large frequency range.

This investigation starts with a discussion of the previously used canonical inductive (Fig. 5-5 left) and capacitive (Fig. 5-5 right) probes. Four different probe positions on the previously used rectangular plate ( $60\text{mm} \times 120\text{mm}$ ) are investigated, as shown in Fig. 6-1. Each single IP or CP is placed in one of the four predefined positions along the long or short edge of the PCB in order to investigate where the highest efficiency over the observed frequency occurs. Notice that the probe positions in this chapter are changed compared to those in chapter 5.

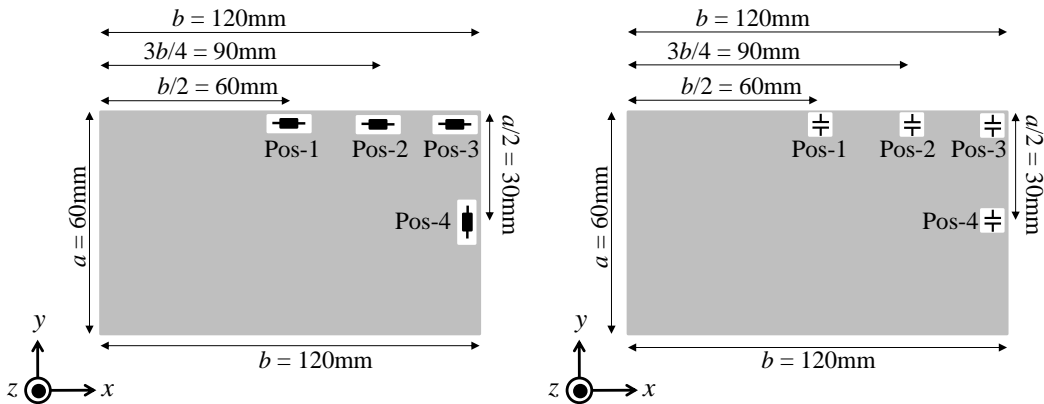


**Fig. 6-1** Inductive probe (IP) and capacitive probe (CP) coupling in four predefined positions on the rectangular plate.

Fig. 6-2 shows the calculated power coefficients of the inductive probe  $IP_{\text{pos}}$  (left) and capacitive probe  $CP_{\text{pos}}$  (right) coupling as a function of the position. That method is used to investigate the best broadband efficiency over the observed frequency range and considers not the peak power coefficients at specific frequencies.



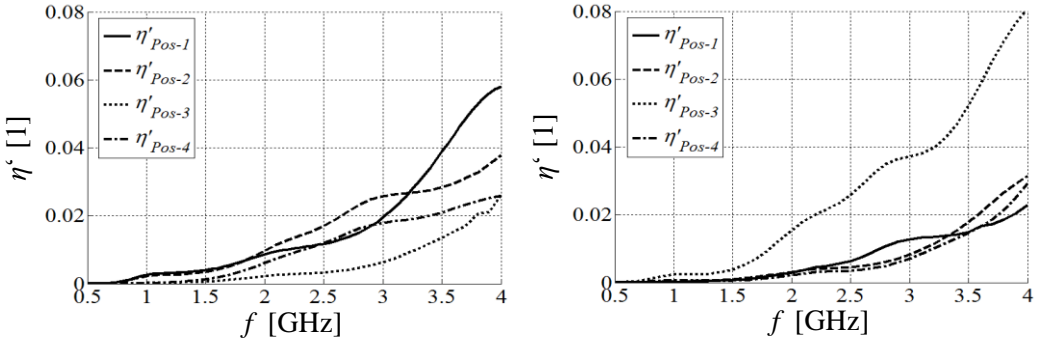


**Fig. 6-2** Normalized power coefficients of the selective IP coupling (left) and CP coupling (right) of the four different positions shown in Fig. 6-2.

Due to the non-resonant excitation of the probe, the characteristic mode of the rectangular plate are not affected, and thus the analysis of Fig. 6-1 and Fig. 6-2 can be directly applied. This applies that the location of the probe affects the relative power coefficient only and not the probe itself.

Comparing all normalized power coefficients in Fig. 6-2, the CP<sub>Pos-3</sub> coupling reaches the highest power coefficient  $\eta'$  over the whole observed frequency range. At that position the probe is located in a maximum of the available modal electric field distributions in the frequency range considered (see Fig. 5-2 and Fig. 5-4). As previously discussed, the characteristic modes with the lowest eigenvalues affects the radiating power of the system, if excited.

Correspondingly, the most promising locations for the inductive probes are Pos-1 and Pos-2, which are located at the current maxima of modes  $\mathbf{J}_1$  and  $\mathbf{J}_2$ , respectively. Based on the current distributions in Fig. 5-2, a probe at Pos-1 can also excite modes  $\mathbf{J}_3$ ,  $\mathbf{J}_4$ ,  $\mathbf{J}_6$  and  $\mathbf{J}_{01}$ . A probe in Pos-2 can excite all of the first seven modes at least to some extent. For further discussions concerning inductive excitation, we select Pos-2 because it offers a slightly better normalized power coefficient compared to Pos-1 in a broad frequency range from 1.9GHz to 2.35GHz.

Next, the inductive probe is replaced by the ICE from Fig. 5-8 a and the capacitive probe is replaced by a modification of the T-shaped CCE from Fig. 5-8 d, which is bended to a corner-shape (see Fig. 6-3). FF-1 is used with both coupling elements and the modal power

## 6. Common Excitation of the Characteristic Modes on Small Handheld Devices

coefficient distribution and achievable bandwidth of the resulting antenna configurations are investigated.

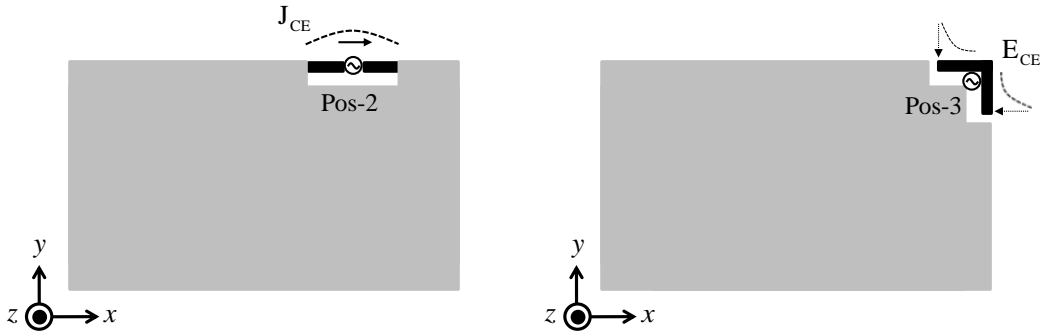


**Fig. 6-3** ICE in Pos-2 (left) and bended T-shaped element in Pos-3 (right) on the rectangular plate of Fig. 5-1.

In both cases the normalized power coefficient  $\eta'$  has been calculated and decomposed in a set of modal contributions  $\eta'_{J_n}$ . Fig. 6-4 shows which modes significantly contribute to the radiation.

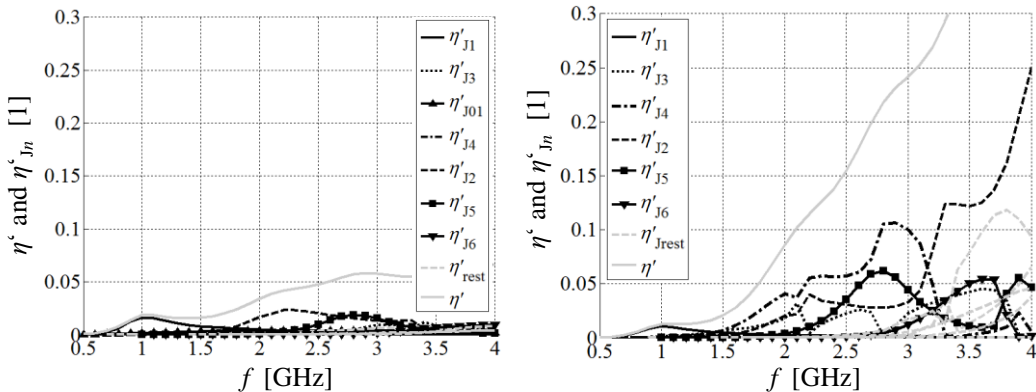


**Fig. 6-4** Normalized power coefficients of the inductive coupling (left) and the capacitive coupling (right) by using the implemented elements, as shown Fig. 6-3.

Both configurations excite most of the available modes (except for mode  $\mathbf{J}_{01}$ ). Comparing the two figures, the capacitive coupling in Pos-3 yields higher modal coefficients at most frequencies. All capacitive modes  $\mathbf{J}_1 - \mathbf{J}_6$  contribute to the radiation. The normalized power coefficient is significantly improved compared to the capacitive probe coupling (Fig. 6-2 (right – Pos-3)), because the CCE strongly affects the radiation in the higher frequency

## 6.1 Common excitation of modes using capacitive coupling or inductive coupling

In addition the CCE deliver more absolute power to the antenna. The inductive coupling by using an ICE in Pos-2 (see Fig. 6-4 left) shows that all of the available modes with low eigenvalues (see Fig. 5-1) can be excited, but the delivered absolute power to the antenna remains lower compared to the capacitive coupling. This indicates a less effective coupling of a single ICE for broadband applications.

As already discussed in section 5.5, the impedance mismatch affects the normalized power coefficient. Hence, an impedance matching is needed to reveal the true performance potential of the antennas.

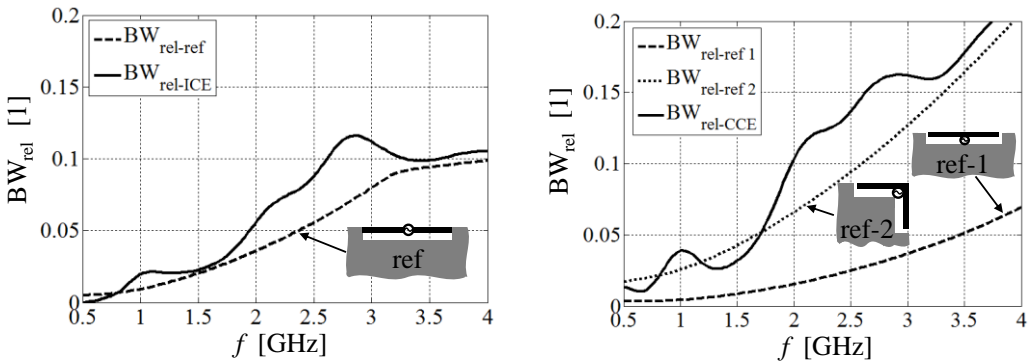


**Fig. 6-5** Calculated relative bandwidth potentials of the inductive coupling (left) and the capacitive coupling (right) by using the elements of Fig. 6-3. Both systems are compared to reference elements on the semi-infinite ground plane.

Therefore, the relative bandwidth potential of each system is calculated and shown in Fig. 6-5 in order to study the tuneability of each configurations. The antenna matching criterion is given by  $|s_{11}| \leq -6\text{dB}$  or  $|VSWR| \leq 3$ . The power transfer to the antenna can be improved to at least  $\eta' = 75\%$  if a matched bandwidth is achieved assuming lossless matching. As references, the coupling elements with the same volume factor (FF-1) are implemented on a semi-infinite ground PCB in order to suppress the characteristic mode excitation on the chassis (see Fig. 6-5). It can be observed that both coupling concepts can be matched and outperform the reference cases at most of the frequencies. The concepts show different bandwidth improvements at the same frequency regions. This can be explained by the different coupling strategies i.e. different mode coupling. The maxima of both the  $BW_{rel-ICE}$  and the  $BW_{rel-CCE}$  occur at the same specific frequencies, which underline the direct relation

of the characteristic modes to the bandwidth. Notice that the maxima of the bandwidth potential approximately coincide with the modal resonances of the modes and their particular superposition of these modes as a function of frequency. A comparison of the eigenvalue analysis of the rectangular plate (see Fig. 5-1) shows that the eigenvalues of all excited modes are  $|\lambda_n| \leq 1$ .

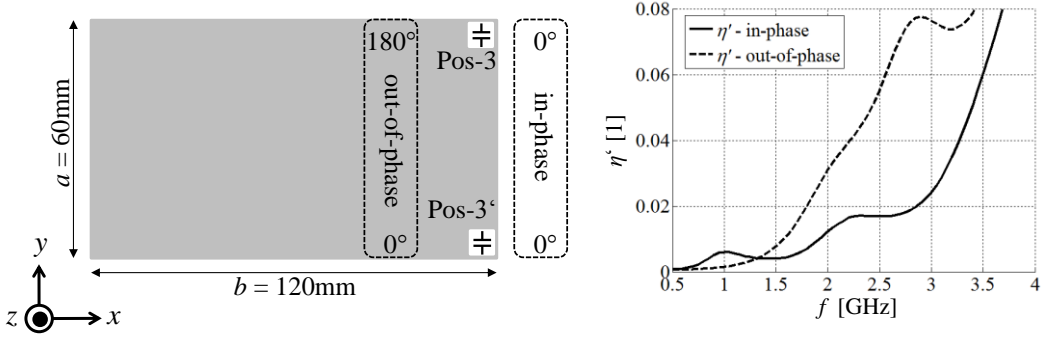
A comparison of the results in Fig. 6-5 indicates that the capacitive excitation of the chassis modes in Pos-3 offers a clear advantage against the references and against the inductive excitation in Pos-2. Recalling section 5.5 (Fig. 5-16), the selective excitation with distributed coupling elements yield even higher bandwidths. However, this does not mean that the selective excitation of the modes results in wider bandwidth. The reason of the higher bandwidth potentials in Fig. 5-16 is due to the fact that the distributed elements use more antenna volume than the single element. The effect of increasing the form factor of a single element is studied in section 6.4.

We should also keep in mind that the input-impedance of the bended capacitive coupling element is changed in comparison to the non-bended case, which results in different relative bandwidth potentials ( $BW_{\text{rel-ref } 2} > BW_{\text{rel-ref } 1}$ ). This affects the radiation as well (see Fig. 6-5 right). Both, the inductive and the capacitive coupling are further discussed by using a distributed ICE pair and a distributed CCE pair excitation. By this an improvement of the delivered power to the antenna is intended and to enhance the bandwidth potential.

### 6.2 Capacitive coupling by using distributed element pairs

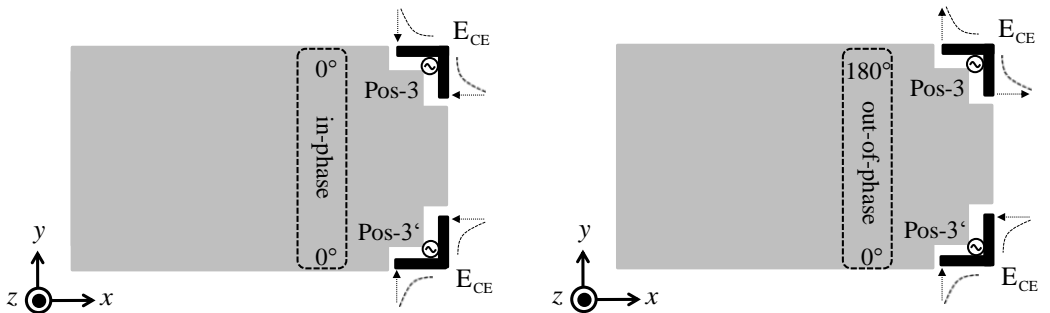
This section evaluate the performance of two capacitive probes driven from a combined feed. Here, the Pos-3' in an adjacent corner Pos-3 will be additionally used to excite the PCB to form a set of two CP's ( $CP_{\text{Pos3}}$  and  $CP_{\text{Pos3}'}$ ). The evaluation is based on an in-phase and an out-of-phase excitation, as shown in Fig. 6-6 left.

It can be seen in Fig. 6-6 (right) that the in-phase excitation offers a clearly better normalized power coefficient  $\eta'$  around 1GHz than the out-of-phase excitation, whereas the out-of-phase excitation offers clearly better power coefficient  $\eta'$  in the higher frequency range. Comparing these results with the results of the single probe coupling in Fig. 6-2 (right) the total efficiencies  $\eta'$  can be strongly improved in frequency range parts.



**Fig. 6-6** Calculated power coefficient of in-phase coupling and out-of-phase coupling of two CP (left) in corners of the rectangular plate.

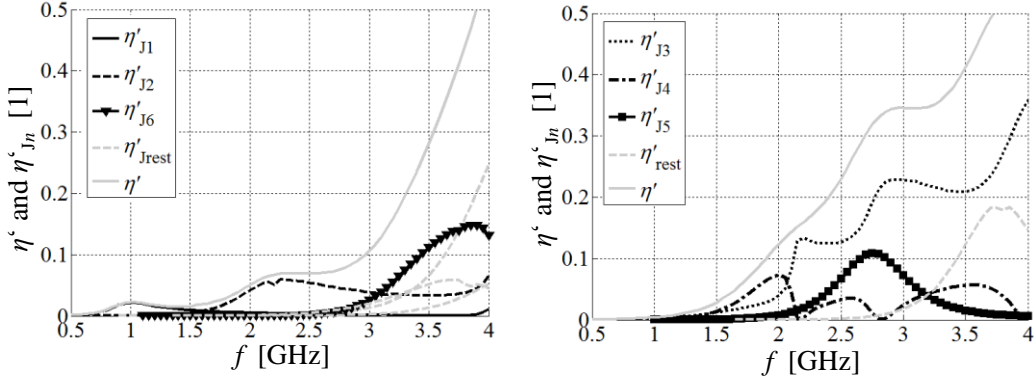
In comparison to the single probe excitation the pairwise coupling results in different excitation of the modes. The idea is that an in-phase excitation of two probes boosts modes which have a common phase in the two probe locations, in this case  $\mathbf{J}_1$ ,  $\mathbf{J}_2$  and  $\mathbf{J}_6$  (see Fig. 5-2). An out-of-phase excitation boosts modes having opposite phases at the probe locations, i.e. modes  $\mathbf{J}_3$ ,  $\mathbf{J}_4$  and  $\mathbf{J}_5$ . To test that prediction, the corner-shaped CCEs is used in the positions Pos-3 and Pos-3', while the in-phase and out-of-phase excitation are applied (Fig. 6-7).



**Fig. 6-7** Two T-shaped elements on the rectangular plate, driven in-phase (left) and out-of-phase (right).

The calculated power coefficient  $\eta'$  of both cases, see Fig. 6-8, show that different sets of decomposed modal power contributions  $\eta'_{,m}$  are obtained. Furthermore, same characteristic modes are excited as predicted before. The in-phase coupling of the elements results mainly in a combined excitation of low order modes  $\mathbf{J}_1$ ,  $\mathbf{J}_2$  and  $\mathbf{J}_6$  and some high order

modes  $\mathbf{J}_{\text{rest}}$  in the higher frequency range. The out-of-phase excitation results in the coupling of the modes  $\mathbf{J}_3$ ,  $\mathbf{J}_4$  and  $\mathbf{J}_5$  and some high order modes  $\mathbf{J}_{\text{rest}}$ . A comparison with single CCE coupling (Fig. 6-4 right) show that the modes  $\mathbf{J}_1 - \mathbf{J}_6$  are now distributed in two groups due to the in-phase and out-of-phase coupling of a CCE pair.



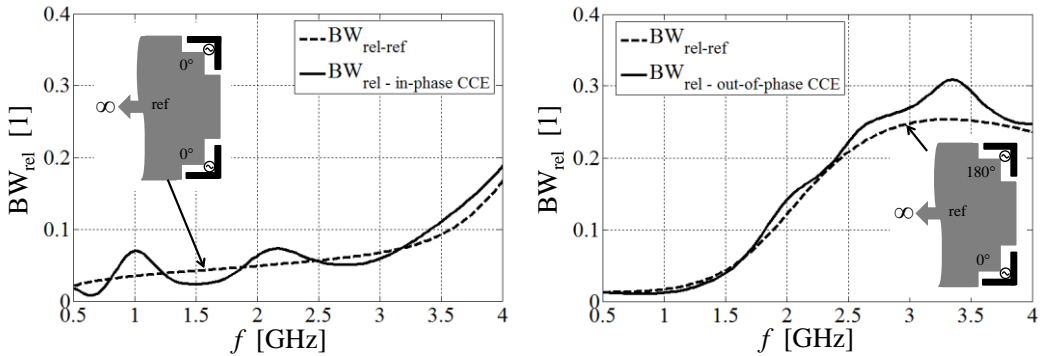
**Fig. 6-8** Normalized power coefficients of the combined coupling of two T-shaped elements on the rectangular plate, driven in-phase (left) and out-of-phase (right).

Fig. 6-8 shows that there are higher order modes  $\mathbf{J}_{\text{rest}}$  (here denotes by  $\eta'_{\text{Rest}}$ ) which have significantly effect on the normalized power coefficient  $\eta'$  in the high frequency range. In both cases the higher order modes denote the summarization of other PCB modes ( $\mathbf{J}_{\text{PCB}}$ ), the coupling structure modes ( $\mathbf{J}_{\text{CCE}}$ ) and the coupling modes ( $\mathbf{J}_{\text{coupl}}$ ).  $\mathbf{J}_{\text{coupl}}$  is defined by the coupling currents between the CCE and the PCB. This phenomenon is further discussed in the section 6.4, where the CCE is made self-resonant.

It can be observed that the normalized power coefficient of the in-phase excitation has two peaks in the low frequency range, whereas the out-of-phase excitation results in a higher power coefficient in the higher frequency range with one peak. The maxima are mainly related to the modal resonances of the modes  $\mathbf{J}_1$  and  $\mathbf{J}_2$  for the in-phase coupling and of modes  $\mathbf{J}_3$  and  $\mathbf{J}_4$  for the out-of-phase coupling. In order to evaluate the tuneability of the systems, the relative bandwidth potentials of both configurations as well as the reference structures are presented in Fig. 6-9.

It can be seen that the in-phase coupling results in a higher relative bandwidth potential at low frequencies (around the modal resonances of modes  $\mathbf{J}_1$  and  $\mathbf{J}_2$ ), whereas for higher

frequencies the case is the opposite.



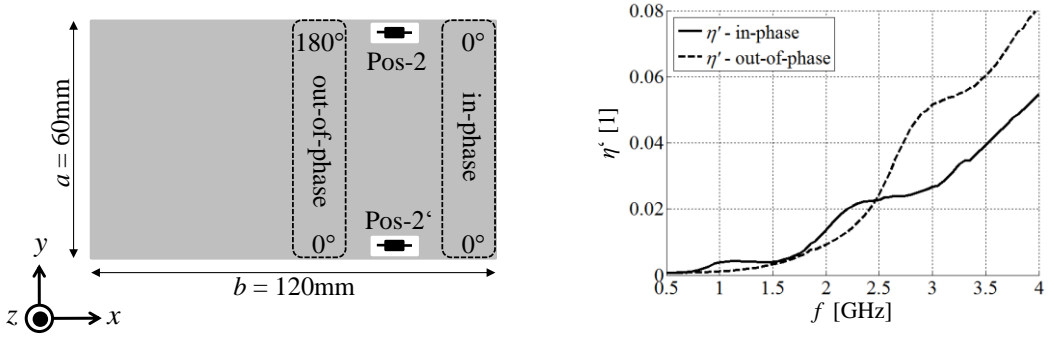
**Fig. 6-9** Calculated relative bandwidth potentials of the in-phase (left) and out-of-phase (right) CCE configurations (see Fig. 6-7) compared to reference values.

The low eigenvalues and the resonances of the modes  $\mathbf{J}_3 - \mathbf{J}_5$  boost here the performance of the out-of-phase excited CCE pair at the higher frequency range. Here, it should be noted that these modes ( $\mathbf{J}_3 - \mathbf{J}_5$ ) exist also in the reference case, because the ground plane is infinite only in negative  $x$ -direction (major axis of the chassis). Since the coupling elements are located in the corners of the PCB, the current modes on the minor axis of the PCB are not suppressed in the reference case, which is seen in the bandwidth results.

In order to conclude this section, the in-phase CCE pair coupling shows a high normalized power coefficient improvement in a low frequency range  $0.69 \leq f [\text{GHz}] \leq 0.96$  compared to the out-of-phase coupling, which offers better power coefficient in the higher frequency range  $1.7 \leq f [\text{GHz}] \leq 4$ . It is shown that the delivered power to the antenna and the relative bandwidths can be improved by using a CCE pair to excite different sets of chassis modes having low eigenvalues on the PCB.

### 6.3 Inductive coupling by using distributed element pairs

This section evaluate the performance of the two inductive probes (IP) from a combined feed, one IP in Pos-2 and one IP on the opposite edge (Pos-2'). The evaluation is done based on an in-phase and an out-of-phase excitation, as shown in Fig. 6-10 left.



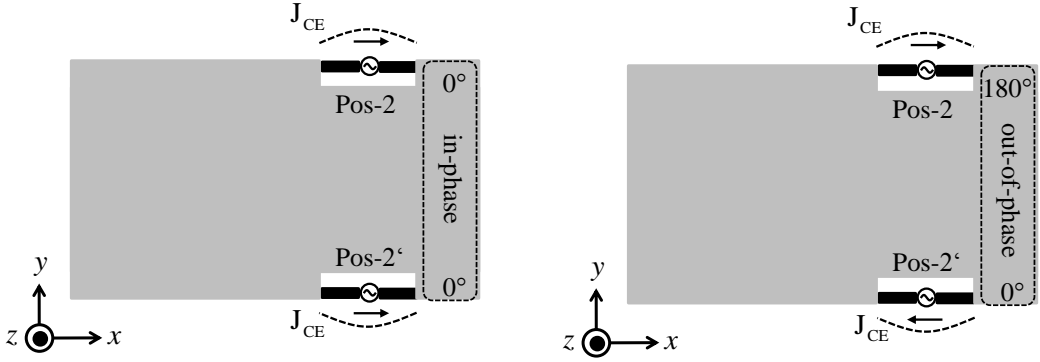
**Fig. 6-10** Calculated power coefficient of in-phase coupling and out-of-phase coupling of two IPs (left) in predefined positions on the rectangular plate.

Fig. 6-10 (right) shows the calculated total normalized power coefficients of both configurations. The in-phase coupling results in better power coefficient compared to the out-of-phase coupling with two maxima at around  $0.5 \leq f [\text{GHz}] \leq 2.5$ . However, the out-of-phase coupling results in a higher value at around  $2.5 \leq f [\text{GHz}] \leq 4$ . Comparing these normalized power coefficients with the coefficients of the single IP coupling (Fig. 6-1 left) an improvement can be noticed, as expected. The in-phase coupling improves especially the total power coefficient in the low frequency range where approximately the resonances of the modes  $\mathbf{J}_1$  and  $\mathbf{J}_2$  are located. The out-of-phase coupling improves the total power coefficient in the high frequency range  $2.5 \leq f [\text{GHz}] \leq 4$ , where the higher order modes with their resonances and low eigenvalues occur (e.g.  $\mathbf{J}_3$ ,  $\mathbf{J}_4$ , and  $\mathbf{J}_5$ ). Again, two sets of modes based on two different coupling scenarios based on the current distribution are excited.

An in-phase or out-of-phase current coupling by the IPs at both edges can be generated (Pos-2 and Pos-2'), as shown in Fig. 6-10 left. If we consider the first seven modes and their current distribution  $\mathbf{J}_n$  in Fig. 5-2 the in-phase coupling mainly excites the modes  $\mathbf{J}_1$ ,  $\mathbf{J}_2$  and  $\mathbf{J}_6$ , whereas the out-of-phase coupling mainly excites the modes  $\mathbf{J}_3$ ,  $\mathbf{J}_4$  and  $\mathbf{J}_5$ .

To confirm this, ICEs from Fig. 5-8 a with FF-1 are placed at the Pos-2 and Pos-2'. The ICEs is driven as combined pair with an in-phase (Fig. 6-11 left) and out-of-phase (Fig. 6-11 right) excitation in the opposite edges. Each configuration should excite a different set of characteristic modes on the PCB.





**Fig. 6-11** Combined coupling of two PCB-integrated ICEs on the rectangular plate, driven in-phase (left) and out-of-phase (right).

The calculated modal power coefficients  $\eta'_{J_n}$  of the ICE pairs are presented in Fig. 6-12. The in-phase coupling of both integrated ICEs results mainly in a combined excitation of low-order modes (here:  $\mathbf{J}_1$  and  $\mathbf{J}_2$ ), the mode  $\mathbf{J}_6$  and some high order modes  $\mathbf{J}_{rest}$ . The out-of-phase coupling results in excitation of the modes  $\mathbf{J}_3$ ,  $\mathbf{J}_4$ ,  $\mathbf{J}_5$ ,  $\mathbf{J}_{01}$  and some high order modes  $\mathbf{J}_{rest}$ .

The total power coefficient  $\eta'$  of the in-phase excitation has two noteworthy peaks in the lower frequency range, whereas the out-of-phase excitation has one significant peak in the higher frequency range. The maxima of the in-phase case are based on the modal contributions  $\eta'_{J_1}$  and  $\eta'_{J_2}$ , whereas the maximum of the out-of-phase case is mainly based on the modal contribution of  $\eta'_{J_5}$ , to a lesser extent mode  $\mathbf{J}_3$ .

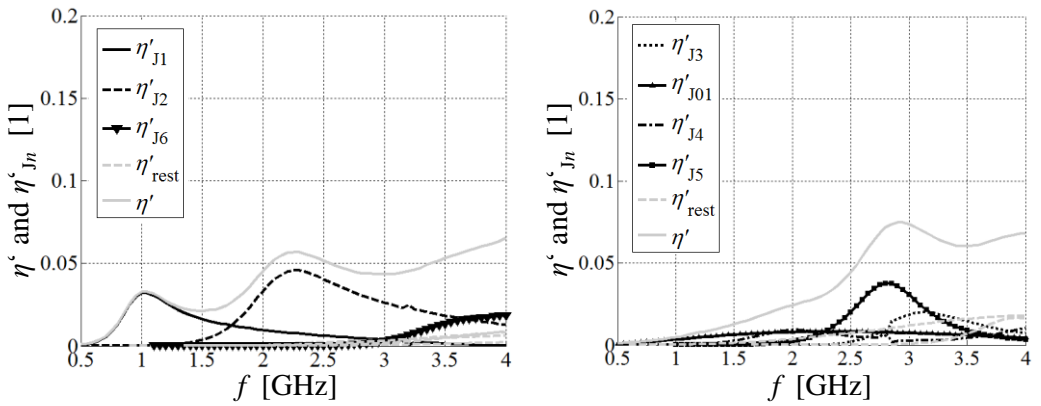


**Fig. 6-12** Normalized power coefficients of the two pairs of ICEs on the rectangular plate, driven in-phase (left) and out-of-phase (right).

## 6. Common Excitation of the Characteristic Modes on Small Handheld Devices

Comparing these results (Fig. 6-12) with the results of the capacitive coupling (Fig. 6-8) we can see that the coupling with the ICE pair is in both scenarios less effective. Higher total and modal power coefficients can be achieved by the capacitive excitation of the modes.

In addition, the relative bandwidth potentials of both ICE configurations are calculated and shown in Fig. 6-13, compared to the reference values. The impedance matching criterion is again fixed to  $|s_{11}| \geq 6\text{dB}$ .

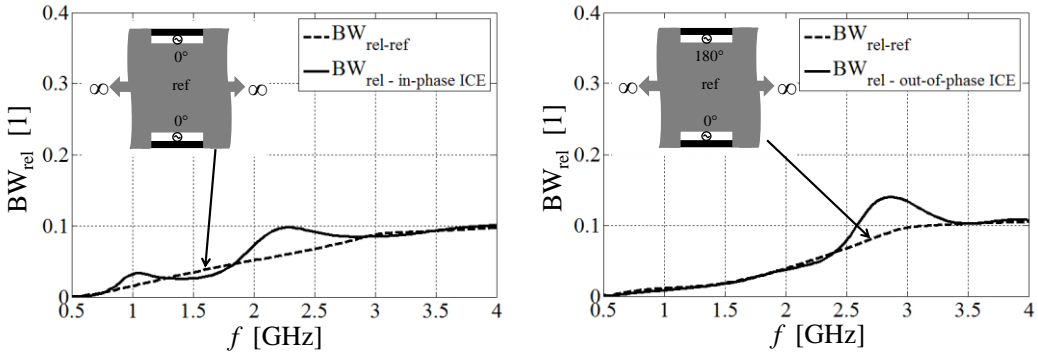


**Fig. 6-13** Calculated relative bandwidth potentials of the in-phase (left) and out-of-phase (right) configurations (see Fig. 6-10) compared to reference structures.

Compared to the reference bandwidth, the in-phase coupling results in a broader bandwidth around the resonances of the excited modes  $\mathbf{J}_1$  and  $\mathbf{J}_2$ . In the out-of-phase case the relative bandwidth can be only improved in a frequency range of  $2.5 \leq f [\text{GHz}] \leq 3.4$  where mode  $\mathbf{J}_5$  is strongly and mode  $\mathbf{J}_3$  less strongly excited.

Comparing the results of Fig. 6-13 with the results of the CCE pair in Fig. 6-9, it can be concluded that the bandwidth obtained by capacitive coupling are generally better. Looking at the in-phase results only, the inductive coupling configurations slightly outperforms the corresponding capacitive one near the resonances of  $\mathbf{J}_2$ , related to the strong coupling to that particular mode, seen in Fig. 6-12 (left). This is related to Pos-2 being located in the current maximum of mode  $\mathbf{J}_2$ , as we recall from section 6.1.

It is also noteworthy to mention that the reference cases ( $\text{BW}_{\text{rel-ref}}$ ) in the inductive coupling case are almost identical because the chassis modes are now mostly suppressed due to the ground plane being infinitely long in both negative and positive  $x$ -direction.

In order to conclude this section, the efficiencies and the relative bandwidths can be improved by using the ICE pair configuration to excite different sets of modes having low eigenvalues on the PCB. It has also been shown that the capacitive coupling with distributed CCEs yield a higher absolute power delivered to the antenna over the observed frequency range than the inductive coupling with two ICEs.

### **6.4 Capacitive excitation of characteristic modes by using off-ground elements**

As shown in sections 6.1 - 6.2, the normalized power coefficient and the bandwidth of a radiating structure can be drastically improved if distributed CCE's are located in the maxima of the electric field distribution of the desired modes. The electric field strength around the CCE should be as high as possible to couple optimally with the characteristic modes of the PCB. The form factor of the element should be used efficiently to achieve a compact, broadband and efficient antenna. Especially this aspect is discussed in the following two sub-sections. Here, the CCE is an off-ground element extending over the PCB dimensions in order to increase the coupling of the modes around the corners optimally. The behavior of the characteristic modes and the off-ground CCE resonances is used to study both effects to each other and what does that mean for the broadband operation of the system without additional matching circuits.

#### **6.4.1 Small off-ground T-shaped CCE's**

This investigation starts with an off-ground T-shaped corner CCE, see Fig. 6-14. Compared to the co-planar CCE in Fig. 6-3, the element here is three-dimensional to couple to the electric field distribution of the characteristic modes optimally and is has been oriented perpendicularly with respect to the electric fields [Vil06, Rah06, Fam06, Fam07].

As seen in Fig. 6-14, the dimensions are the length  $d = 20\text{mm}$ , the height  $c = 6\text{mm}$  and the variable gap distance  $e$  between the CCE and the PCB. The dimensions of the PCB are still fixed to  $60\text{mm} \times 120\text{mm}$ . The reference structure in Fig. 6-14 (right) is used to have the CCE on a semi-infinite PCB to suppress the influence of the characteristic modes on the PCB.

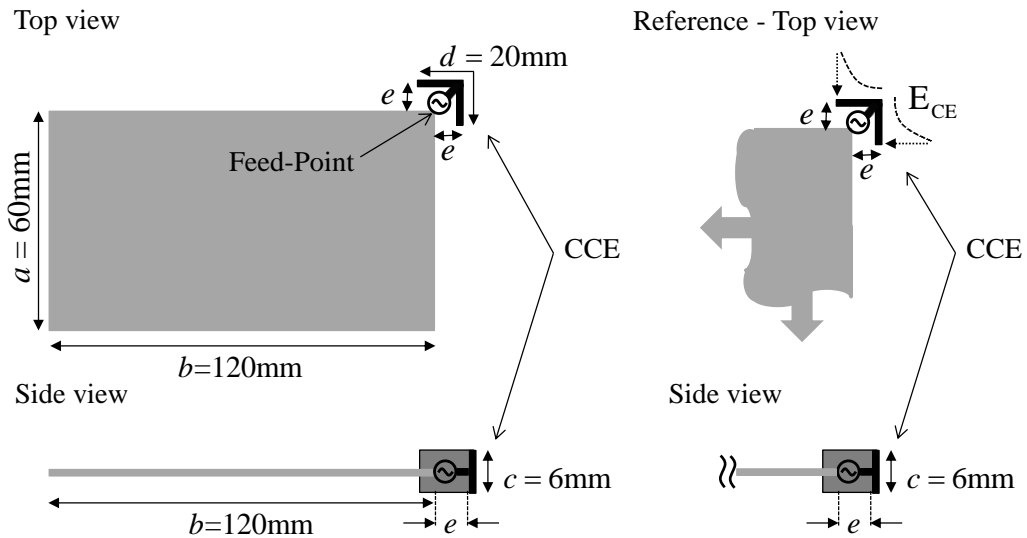


**Fig. 6-14** Implemented off-ground T-shaped CCE at the corner of the rectangular plate and an identical CCE on a semi-infinite PCB.

Both, the input-impedance of the CCE on the PCB (black curve) and its reference (black dotted curve) are shown on the Smith chart relative to  $50\Omega$  in Fig. 6-15. Here, the gap between the CCE and the PCB varies with  $e = 2\text{mm}$ ,  $4\text{mm}$ ,  $6\text{mm}$ , and  $8\text{mm}$ . It can be seen in Fig. 6-15 that the CCE is now self-resonant itself. The zero reactance point of the CCE antenna is marked with 0 in the figures. Thanks to the resonances, the CCE is now matched at certain frequency even without a separate matching circuit to 6dB return loss criterion (grey circle). The effect of the characteristic modes of the PCB can be localized at frequencies where the radiation resistances become larger in comparison to the references. Such impedance points are marked with the points 1, 2 and 3. For a better comparison, the resonance frequencies and the resulting matched 6dB - BW are summarized in Table 6-1. By increasing the value  $e$ , the resonance frequency is shifted towards the lower frequency region and results in a smaller 6dB bandwidth (see Table 6-1). With  $e = 2\text{mm}$ , the radiation resistance is rather low, and the input impedance is dominantly capacitive. With increasing  $e$ , the radiation resistance is increased as well and the input impedance becomes more inductive. The resonance frequency (point 0) shifts lower in frequency.

## 6.4 Capacitive excitation of characteristic modes by using off-ground elements

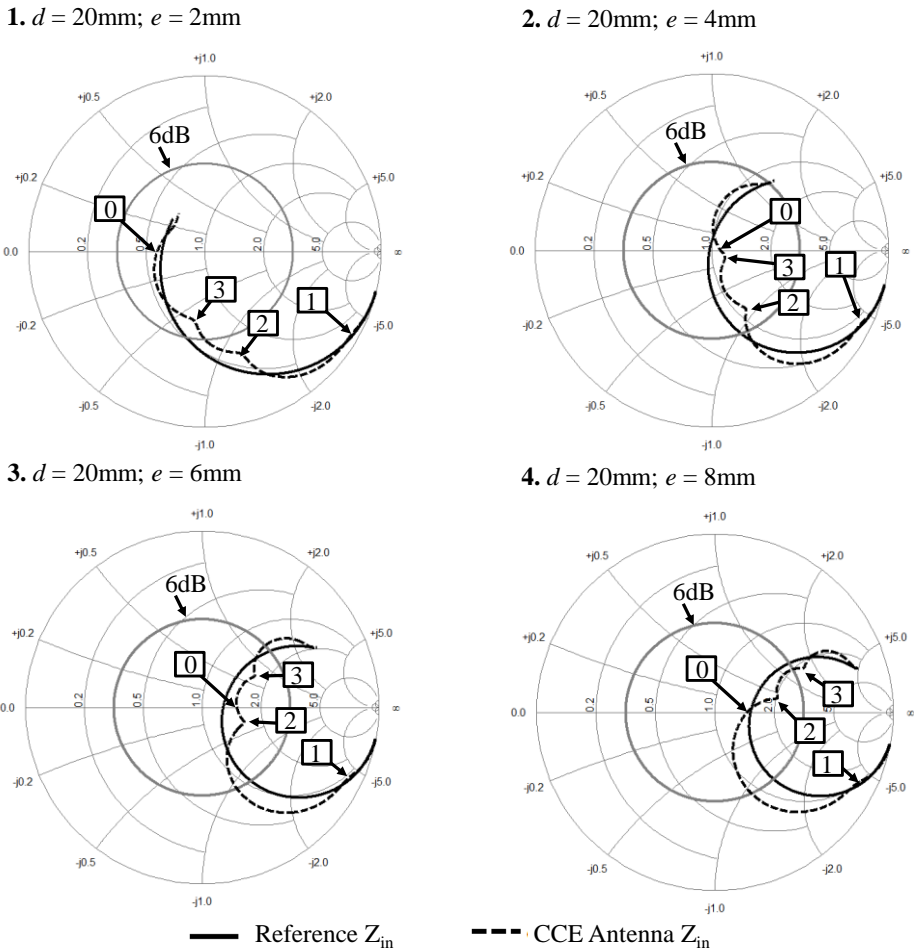


**Fig. 6-15** Calculated input-impedances of both the off-ground T-shaped corner CCE (black curve) and its reference (black dotted curve) with varying  $e = 2, 4, 6,$  and  $8$  [mm].

In order to analyze the delivered absolute power to the antenna of the four investigated configurations in Fig. 6-14 the normalized power coefficient of each one is calculated in Fig. 6-16. The figure shows how effective the coupling of the off-ground CCE is by increasing the coupling area around the corner of the PCB. It seems that the closer the resonance frequency (point 0) becomes to the points 1, 2, and 3 the higher the delivered absolute power becomes at that region. It means that making the CCE resonant at the same frequency using chassis modes the normalized power coefficient is improved. The same dependency can be observed in the bandwidth potential curves in Table 6-1 and the input-impedances curves in Fig. 6-15 as well. This means that a chassis antenna is matched near

## 6. Common Excitation of the Characteristic Modes on Small Handheld Devices

the resonances of the chassis more easily than at other frequencies. This indicates that the point 0 is the key parameter to increase the antenna performance of the system.

**Table 6-1** Self-resonances and 6dB - BW of both the off-ground T-shaped corner CCE and its reference with varying  $e = 2, 4, 6,$  and  $8$  [mm].

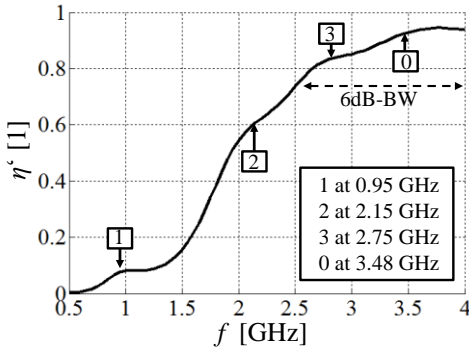
Parameter		Reference CCE		CCE Antenna		
in [mm]		values in [GHz]		values in [GHz]		
$d$	$e$	$\text{Im}\{Z_{in}\}=0$	6dB - BW	$\text{Im}\{Z_{in}\}=0$	6dB - BW	
1.	20	2	3.56	n/a (2.63 to n/a)	3.48	n/a (2.55 to n/a)
2.	20	4	2.77	1.94 (2.06 to 4.00)	2.85	1.87 (1.88 to 3.75)
3.	20	6	2.31	1.30 (1.78 to 3.08)	2.30	1.45 (1.68 to 3.13)
4.	20	8	2.02	0.97 (1.59 to 2.56)	1.75	0.99 (1.51 to 2.50)

If the frequency points 1, 2 and 3 in Fig. 6-16 are compared to the frequencies of the power coefficient maxima of the capacitive probe coupling in Fig. 6-2 (right at Pos 3) or the small CCE coupling in Fig. 6-4 (right), they are essential similar. This means that the same characteristic modes  $\mathbf{J}_1 - \mathbf{J}_6$  on the PCB as in the previous cases are excited. As shown in Fig. 6-16, points 1, 2 and 3 are slightly shifted lower in frequency, resulting from the increased electrical size of the structure.

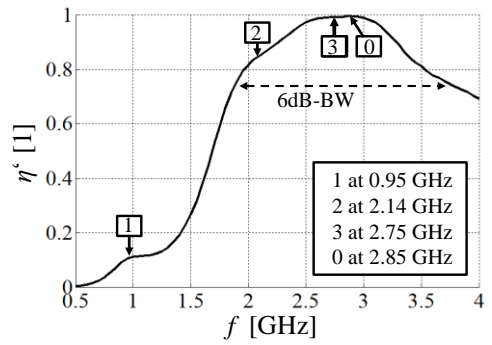
As seen in Fig. 6-16, the efficient coupling with higher order modes results in a broader 6dB-BW when  $e$  is small. With increasing value of  $e$ , the coupling to lower order modes improves, shifting the matched band towards lower frequencies and making the reached bandwidth narrower. The decrease of the bandwidth can be explained by the lower modal quality factors  $Q_{\text{eig},n}$  of the higher order modes, shown in Table 5-1. In addition, the higher the frequency becomes, the more modes with low eigenvalue can be excited, enabling high absolute power delivered to the antenna. In the lower frequency region around 1GHz, the size of the CCE is not sufficient to provide self-resonance and therefore the achieved normalized power coefficient is low. Therefore the coefficient around the point 1 in Fig. 6-16 (case 4) can only be improved to 20% without impedance matching actions.

## 6.4 Capacitive excitation of characteristic modes by using off-ground elements

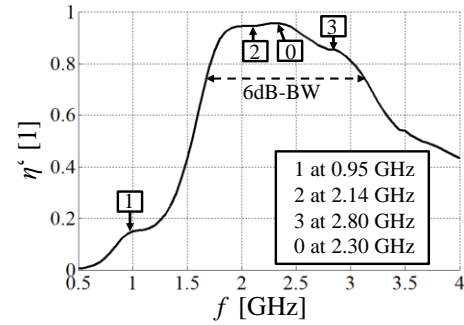
1.  $d = 20\text{mm}$ ;  $e = 2\text{mm}$



2.  $d = 20\text{mm}$ ;  $e = 4\text{mm}$



3.  $d = 20\text{mm}$ ;  $e = 6\text{mm}$



4.  $d = 20\text{mm}$ ;  $e = 8\text{mm}$

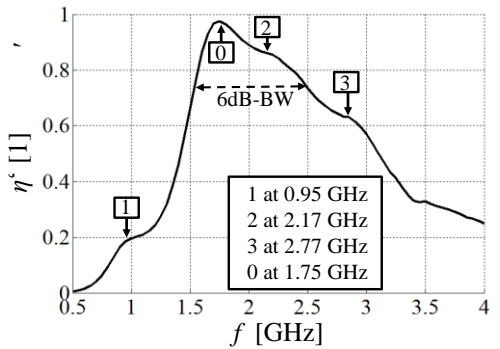
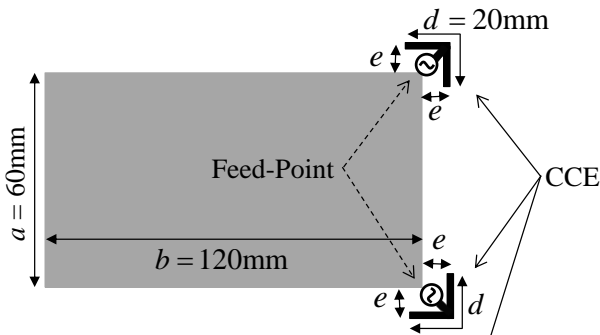


**Fig. 6-16** Normalized power coefficients of both the off-ground T-shaped corner CCE (black curve) with varying  $e = 2, 4, 6,$  and  $8$  [mm].

Top view



Side view

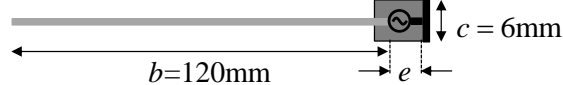


**Fig. 6-17** Implementation of two off-ground T-shaped CCE mounted on the corner on the PCB.

## 6. Common Excitation of the Characteristic Modes on Small Handheld Devices

To study this approach in terms of using a CCE pair the configurations shown in Fig. 6-17 is used. Such a coupling method with a distributed pair has already been used in section 6.2 where has shown promising results. Therefore it will be studied as well.

The off-ground CCE's is driven in-phase or out-of-phase, as shown in Fig. 6-18. Here, as well as in section 6.2, different phases of the electric field distributions  $E_{CCE}$  occur on each corner resulting in coupling of two different sets of characteristic modes on the PCB.

The calculated self-resonances of both configurations in Fig. 6-18 for all cases ( $e = 2, 4, 6$  and  $8$  [mm]) are summarized in Table 6-2.

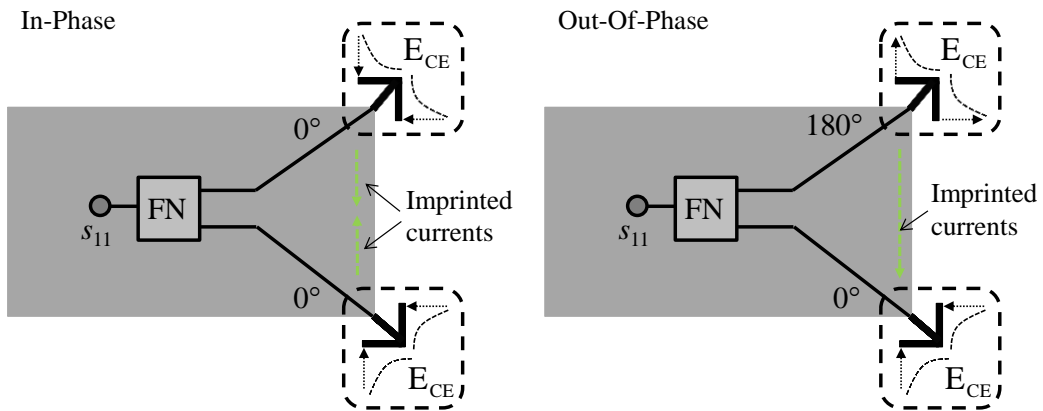


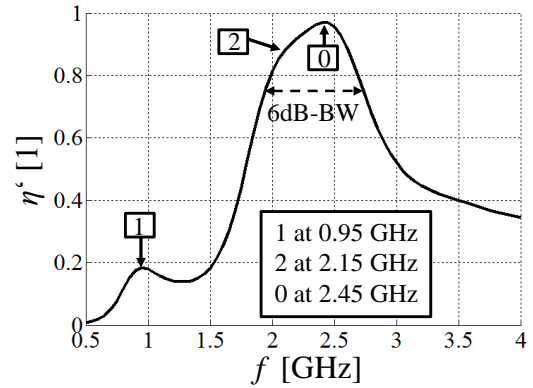
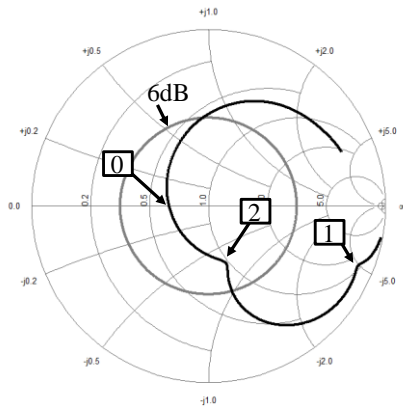
**Fig. 6-18** Combined in-phase (left) and out-of-phase (right) of the CCE's in Fig. 6-17.

**Table 6-2** Self-resonances and 6dB - BW of the off-ground T-shaped corner CCE pairs with varying  $e = 2, 4, 6,$  and  $8$  [mm].

Parameter		In-Phase CCE		Out-Of-Phase CCE		
in [mm]		values in [GHz]		values in [GHz]		
$d$	$e$	$\text{Im}\{Z_{in}\}=0$	6dB - BW	$\text{Im}\{Z_{in}\}=0$	6dB - BW	
1.	20	2	3.18	n/a (3.23 to n/a)	n/a	n/a (2.1 to n/a)
2.	20	4	2.82	0.64 (2.61 to 3.25)	3.4	n/a (1.69 to n/a)
3.	20	6	2.45	0.78 (1.95 to 2.73)	1.70	1.95 (1.50 to 3.45)
4.	20	8	2.15	0.75 (1.78 to 2.53)	1.55	0.71 (1.36 to 2.07)



3. In-Phase  $d = 20\text{mm}$ ;  $e = 6\text{mm}$



4. In-Phase  $d = 20\text{mm}$ ;  $e = 8\text{mm}$

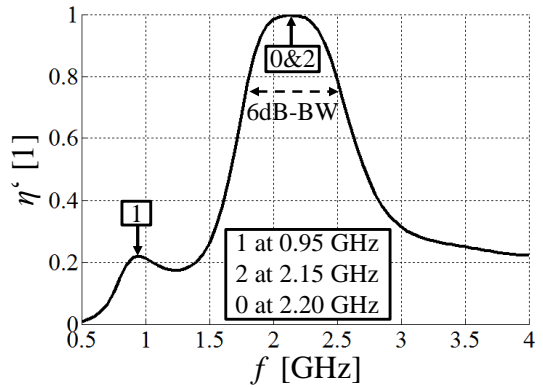
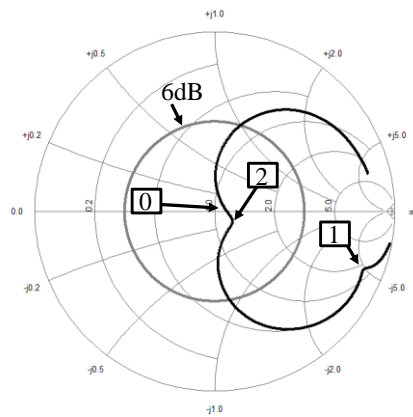
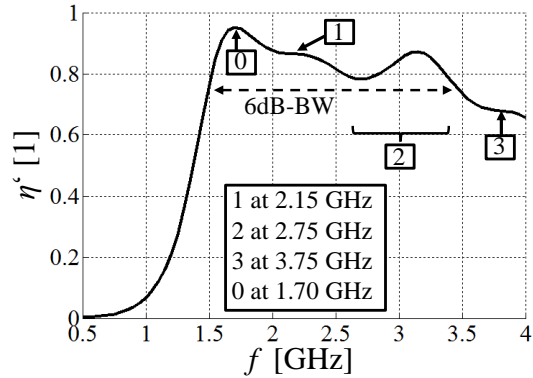
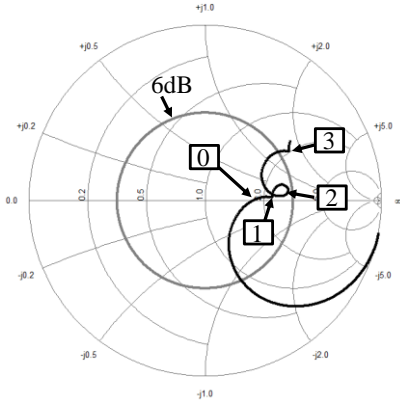


**Fig. 6-19** Calculated input-impedances (left) and normalized power coefficients (right) of the CCE pair driven in-phase and varying with  $e = 6$  and  $8$  [mm].

It can be shown that the resonances of both configurations are shifting lower in frequency with increasing  $e$ . The most notable observation is that the resonance frequencies of the in-phase and out-of-phase configurations are very different. This can be lead back to the different excitation of the modes, as already investigated in section 6.2.

The distances  $e = 6\text{mm}$  and  $e = 8\text{mm}$  (see Table 6-2 case 3 and 4) are compared with each other concerning the input impedance  $Z_{in}$  and the calculated normalized power coefficient  $\eta'$ . Both the in-phase and out-of-phase configuration results are shown in Fig. 6-19 and Fig. 6-20.

3. Out-Of-Phase  $d = 20\text{mm}$ ;  $e = 6\text{mm}$



4. Out-Of-Phase  $d = 20\text{mm}$ ;  $e = 8\text{mm}$

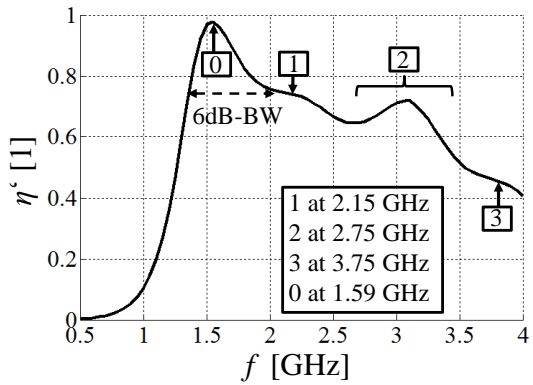
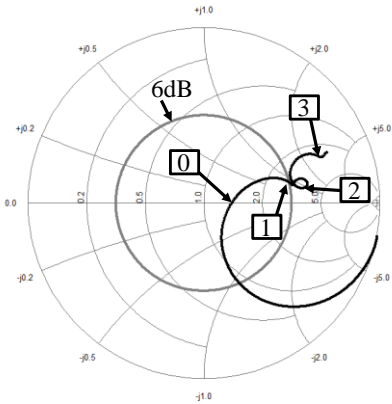


**Fig. 6-20** Calculated input-impedances (left) and normalized power coefficients (right) of the CCE pair driven out-of-phase and varying with  $e = 6$  and  $8$  [mm].

The results of the in-phase coupling in Fig. 6-19 show only two significant radiation resistance points where mainly the mode  $\mathbf{J}_1$  (Point 1) and  $\mathbf{J}_2$  (Point 2) are excited (compare to Fig. 6-8 left). In addition, there is only one self-resonance at point 0 ( $\text{Im}\{Z_{\text{in}}\}=0$ ), which is mainly caused by the resonance of the CCE pair. This point is also shifting lower in frequency and couples with the mode  $\mathbf{J}_2$  at point 2. The highest power coefficient can be achieved if the points 0 and 2 are close to each other (see Fig. 6-19 case 4). The coefficient at point 1 is lower due to the insufficient coupling at that low frequency in order to make the antenna operate at low frequencies. The input impedance must be re-designed in such a way that the self-resonance of the CCE occurs closer to the point 1 and couples more effectively with mode  $\mathbf{J}_1$  at that frequency range.

The results of the out-of-phase configuration in Fig. 6-20 show three significant radiation resistance points (point 1, 2 and 3) of the resulting input-impedances (left), which significantly affect the total efficiency (right). As shown, the points 1-3 are shifted higher in frequency resulting from an excitation of the modes  $\mathbf{J}_3$  -  $\mathbf{J}_5$  (compare Fig. 6-8 right). All of these modes have their resonances higher in frequency and contributing to the radiation if the self-resonance at point 0 is nearby. The resonance ( $\text{Im}\{Z_{\text{in}}\} = 0\Omega$ ) is shifting lower in frequency and generates an in-phase imprinted current between the CCEs on the PCB and makes the effective form factor of the CCE antenna larger. Due to the shift of the resonance to lower frequencies (here: out of the modal resonance), the bandwidth potential, the matching and the normalized power coefficient become less effective around that frequency point if the distance  $e$  becomes larger. A comparison with the in-phase coupling in Fig. 6-19 shows an out-of-phase imprinted current behavior between the CCE elements where the currents on the PCB can be neglected.

Both, the in-phase and the out-of-phase configuration, indicate that the self-resonance frequency (point 0) is a dominant parameter improving the total normalized power coefficient in or near the same frequency region. If the self-resonance of the coupling element comes closer to the points where a high radiation resistance occurs (point 1, 2 and 3) the absolute power delivered to the antenna is increased and a matched 6dB - BW occurs.

### 6.4.2 Large off-ground CCE

The commonly used Capacitive Coupling Element (CCE) based antenna was first introduced in [Van02, Vil06] and was mainly used to demonstrate the relation of the achievable bandwidth with respect of the small form factor antennas. The key idea was to replace the self-matched antennas with an inherently non-matched CCE, where the shape, type and location are selected in such a way that the dominant modes on the PCB are sufficiently excited. A separate matching circuitry was used to realize a matched input impedance at the desired single and broadband frequency ranges [Val13\_1, Val13\_2]. The recent publication [Val14] shows a summarization of the usage of such CCEs.

Therefore the aim of this sub-section is to analyze such a commonly used off-ground CCE based on the TCM in order to see how the excited characteristic modes behave and what that means for the absolute power delivered to the antenna without using external matching

## 6. Common Excitation of the Characteristic Modes on Small Handheld Devices

circuitry. As shown in the previous sub-section 6.4.1, the bandwidth (6dB-BW) and the normalized power coefficient  $\eta'$  can be improved if the form factor (FF) of the CCE and the respective input impedance can be modified to couple the desired characteristic modes near or in the resonances. The self-resonance frequency at point 0 ( $\text{Im}\{Z_{\text{in}}\} = 0\Omega$ ) of the reference CCE should be located near to the frequency where the modal resonance of the desired mode occurs. According to the results discussed above and the results in [Van02, Hol10], the off-ground CCE seems to be a promising antenna element that can efficiently excites the dominating modes of the PCB.

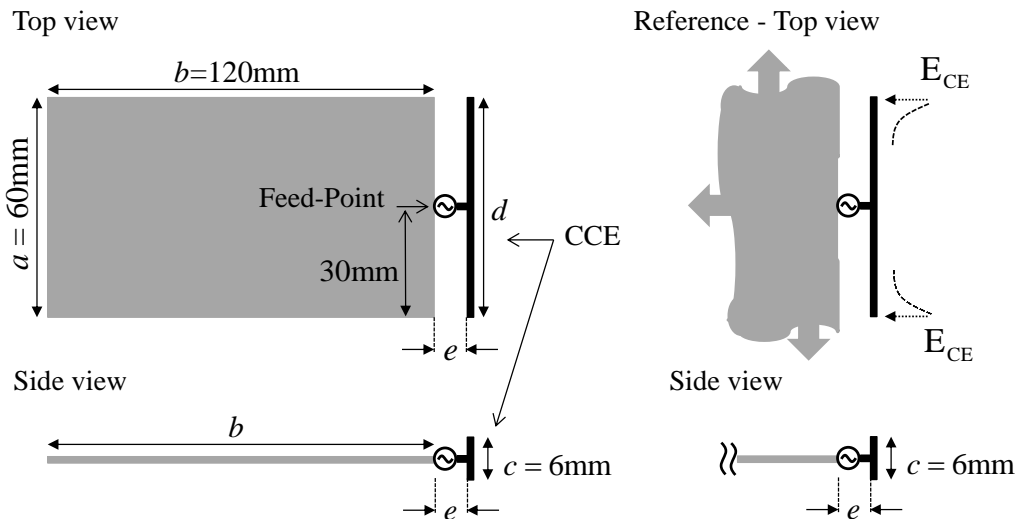


**Fig. 6-21** Large off-ground CCE and its reference CCE on a semi-infinite ground.

The off-ground CCE here used, shown in Fig. 6-21 (left), is oriented perpendicularly with respect to the electric fields of the dominant characteristic modes of the PCB. The electric field coupling of such a configuration generates a common in-phase capacitive excitation of the respective characteristic modes. The investigated PCB has the same dimensions as in the previous sections. The length  $d$  of the CCE and the gap  $e$  between the PCB and the CCE are variable and used as investigation parameters. The feeding point is fixed to the middle of the chassis' short edge to create symmetrical electric field loadings of both corners.

The reference in Fig. 6-21 (right), mounted on top of the half-infinite ground, is used to analyze the CCE without an influence of the characteristic mode coupling.

#### 6.4 Capacitive excitation of characteristic modes by using off-ground elements

The 6dB impedance bandwidths (6dB-BW) and the self-resonances ( $\text{Im}\{Z_{in}\} = 0\Omega$ ) of both configurations reached by varying the parameters  $d$  and  $e$  in the observed frequency range ( $0.5 \leq f[\text{GHz}] \leq 4$ ) are shown in Table 6-3. It can be observed that the larger the form factor of the CCE is, the smaller the 6dB-BW becomes and the self-resonance is shifted lower in frequency.

**Table 6-3** Self-resonances and 6dB - BW of the large off-ground CCE and its reference with varying  $d$  and  $e$ .

Parameter		Reference		CCE Antenna		
in [mm]		values in [GHz]		values in [GHz]		
$d$	$e$	$\text{Im}\{Z_{in}\}=0$	6dB - BW	$\text{Im}\{Z_{in}\}=0$	6dB - BW	
1.	10	2	n/a	n/a	n/a	
2.	10	5	4.00	n/a (3.26 to n/a)	3.5	n/a (3.3 to n/a)
3.	10	8	3.26	n/a (2.67 to n/a)	3.08	0.93 (2.80 to 3.73)
4.	20	8	2.44	1.18 (2.02 to 3.20)	2.48	0.49 (2.20 to 2.69)
5.	30	8	1.99	0.9 (1.69 to 2.59)	2.05	0.58 (1.81 to 2.39)
6.	40	8	1.71	0.71 (1.47 to 2.18)	1.75	0.50 (1.72 to 2.22)
7.	50	8	1.50	0.54 (1.33 to 1.87)	1.60	n/a
8.	60	8	1.34	0.41 (1.22 to 1.63)	1.48	n/a
9.	74	8	1.18	0.48 (1.05 to 1.53)	1.4	0.22 (0.89 to 1.11)

In addition to the first eight cases in Table 6-3, where the length of the CCE is shorter or equal to the width of the chassis, a bended version of the CCE (Fig. 6-22) is used as case 9. The length  $d$  of the 74mm is obtained by bending the ends of the CCE at the corners of the chassis. Due to the bended part, the electric fields at the corners can be efficiently used for coupling, see section 6.2. The form factor occupied by the CCE antenna compared to the case 8 is nearly the same. Furthermore, the PCB is slightly cut at the corners in order to have an unchanged coupling distance between the outer edges of the CCE and the corners of the PCB. As shown in Table 6-3 (case 9), the modification shifts the self-resonances of

## 6. Common Excitation of the Characteristic Modes on Small Handheld Devices

the antenna and the matched frequency band towards lower frequencies. Compared to the reference case the self-resonance of the bended CCE based antenna occurs at a higher frequency and the 6dB-BW becomes smaller.

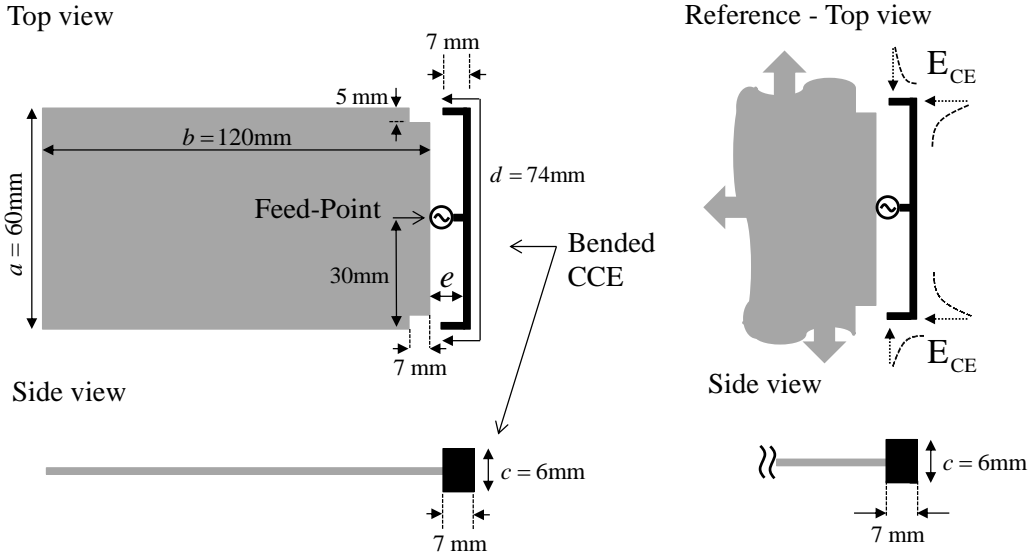
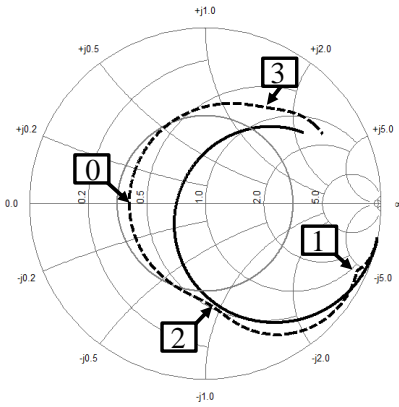


**Fig. 6-22** The large off-ground CCE bended around the corners and the corresponding reference CCE on a semi-infinite PCB.

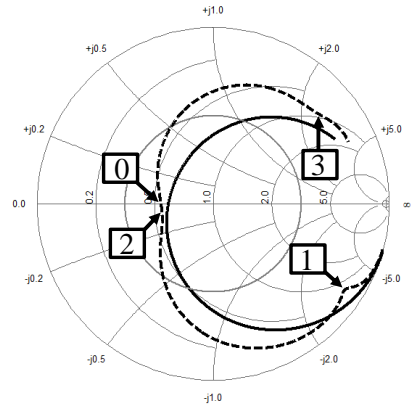
In all cases, having the same  $e = 8\text{mm}$ , it can be observed that the increase of the length  $d$  of the CCE decreases the 6dB – BW and shifts the self-resonance of both systems lower in frequency. A comparison of the matching shows that with the finite PCB the matching of the antenna system decreases drastically, as shown in Table 6-3 (cases 7-9). Only the bended CCE approach results in good matching zone at low frequencies.

For a fair comparison of the relevant cases, the input-impedances of the cases 4 - 9 are shown in Fig. 6-15 on the Smith chart relative to  $50\Omega$ . Now, the gap between the CCE and the PCB is fixed to  $e = 8\text{mm}$  and the length  $d$  varies in in a range of  $20 \leq d [\text{mm}] \leq 74$  within the observed frequency range of  $0.5 \leq f [\text{GHz}] \leq 4$ .

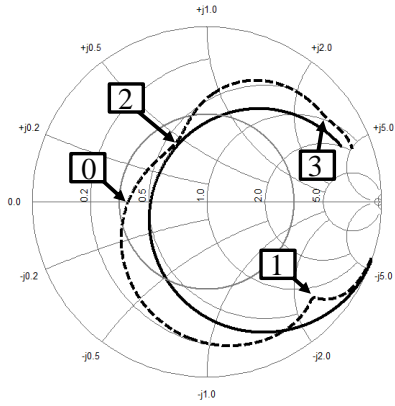
4.  $d = 20\text{mm}$ ,  $e = 8\text{mm}$



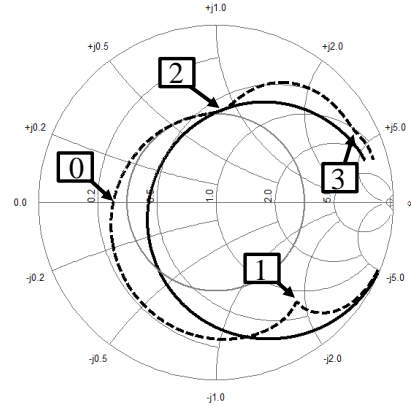
5.  $d = 30\text{mm}$ ,  $e = 8\text{mm}$



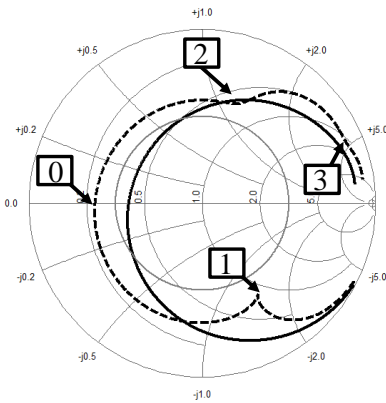
6.  $d = 40\text{mm}$ ,  $e = 8\text{mm}$



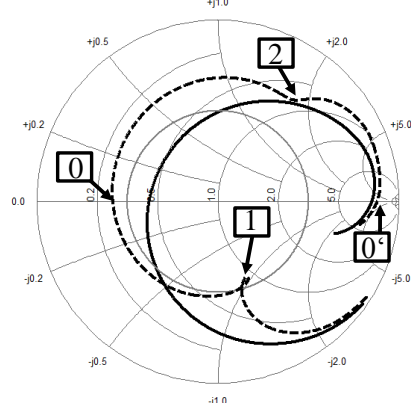
7.  $d = 50\text{mm}$ ,  $e = 8\text{mm}$



8.  $d = 60\text{mm}$ ,  $e = 8\text{mm}$



9.  $d = 74\text{mm}$ ,  $e = 8\text{mm}$



— Reference  $Z_{in}$       - - - CCE Antenna  $Z_{in}$       — 6dB

Fig. 6-23 Calculated input-impedance of the off-ground CCE on the PCB (black curve) and its reference (black dotted curve) with  $e = 8\text{mm}$  and varying  $d$ .

## 6. Common Excitation of the Characteristic Modes on Small Handheld Devices

---

The CCE input impedance is heavily affected by the finite PCB and results in different substantial radiation resistance points (point 1 - 3). In addition, the self-resonance (point 0) and an anti-resonance (point 0') of the CCE are marked in order to localize both for further explanation. The grey circle on the Smith chart plots re-presents the threshold inside which the input-impedance are matched to 6dB return loss or better.

As shown in Fig. 6-23, the increase in  $d$  shifts the input impedance in inductive direction, and notably, the input resistance increases in the lower frequency range. The point 3 loses its importance as it moves towards an anti-resonance in the high-impedance end of the Smith chart, whereas point 1 increases in its significance. The point 2 shifts closest to the center of the Smith chart and coincides with the point 0 (case5). It can be seen that the relative positions of points 0 and 2 determine the 6dB bandwidth in cases 4-7. In case 9, the point 1 reaches the 6dB circle due to the increased radiation resistance and inductance. Based on the chassis coupling the input-impedance results in a higher inductive behavior in the frequency region between the points 1 and 2. This results in an un-matched region as opposed to the reference. In that region the mode excitation is less affected and heavily affects the radiation resistance in a minimum. Furthermore, an additional anti-resonance at 3.2GHz (point 0') occurs due to the reference input impedance in case 9.

This investigation shows that the length  $d$  of the CCE track (shifting of the point 0 from  $f = 2.48\text{GHz}$  (case 4) to  $f = 1.4\text{GHz}$  (case 9)) and the PCB heavily affect the overall radiation of the system in the observed frequency range.

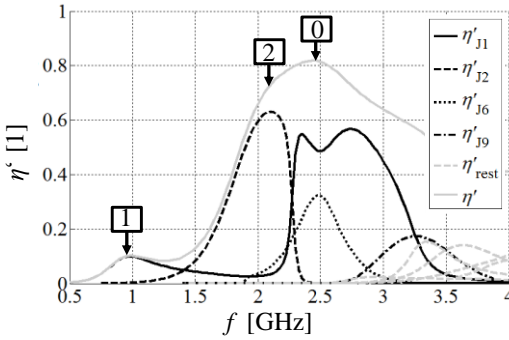
In order to evaluate how efficiently we direct the power into the excited modes of the investigated structure the normalized power coefficient  $\eta'$  (see (4-27)) and its decomposition in the modal contributions  $\eta'_{jn}$  are calculated and compared in Fig. 6-24. It can be seen in Fig. 6-24, that the modes  $\mathbf{J}_1$ ,  $\mathbf{J}_2$ ,  $\mathbf{J}_6$  and  $\mathbf{J}_9$  are mainly excited, contributing to the normalized power coefficient  $\eta'$  depending on where the self-resonance (point 0) is located. In addition, the maxima of the modal power coefficients  $\eta'_{j2}$  and  $\eta'_{j6}$  are shifted lower in frequency if the length  $d$  of the CCE track is increased. That means the electrical size of the CCE (here point 0) plays a significant role in determining how efficiently the CCE couples to the characteristic modes. The maximum of  $\eta'_{j2}$  is shifted from  $f = 2.1\text{GHz}$  to



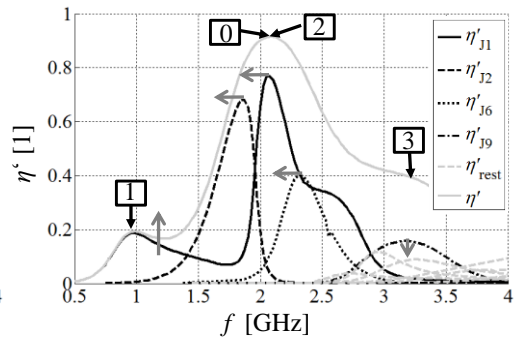
### 6.4 Capacitive excitation of characteristic modes by using off-ground elements

$f = 1.4\text{GHz}$  and  $\eta'_{j6}$  is shifted from  $f = 2.5\text{GHz}$  to  $f = 2.1\text{GHz}$ . This means that the maximum of  $\eta'_{j6}$  at  $d = 60\text{mm}$  (point 2 in case 8) or  $d = 74\text{mm}$  (point 2 in case 9) occurs at the same frequency, where  $\eta'_{j2}$  occurs at  $d = 20\text{mm}$  (point 2 in case 4). It seems that the point 0 (depending on the length  $d$ ) controls where the excited modes are significantly contributing to the absolute power  $P_{\text{abs.in}}$ .

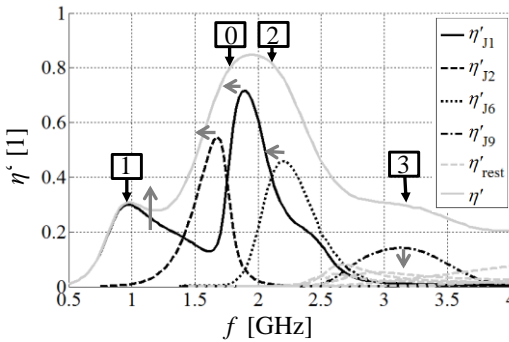
4.  $d = 20\text{mm}$ ,  $e = 8\text{mm}$



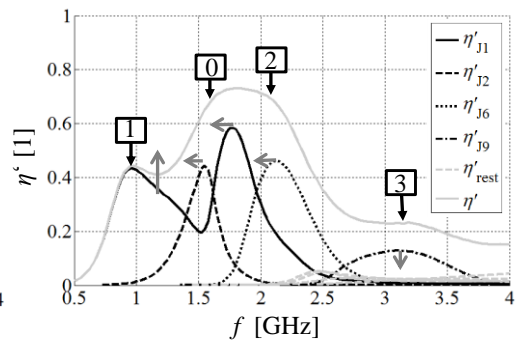
5.  $d = 30\text{mm}$ ,  $e = 8\text{mm}$



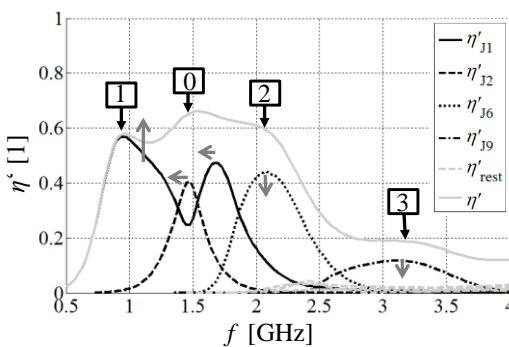
6.  $d = 40\text{mm}$ ,  $e = 8\text{mm}$



7.  $d = 50\text{mm}$ ,  $e = 8\text{mm}$



8.  $d = 60\text{mm}$ ,  $e = 8\text{mm}$



9.  $d = 74\text{mm}$ ,  $e = 8\text{mm}$

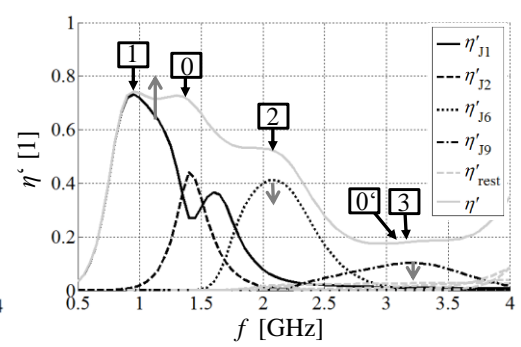
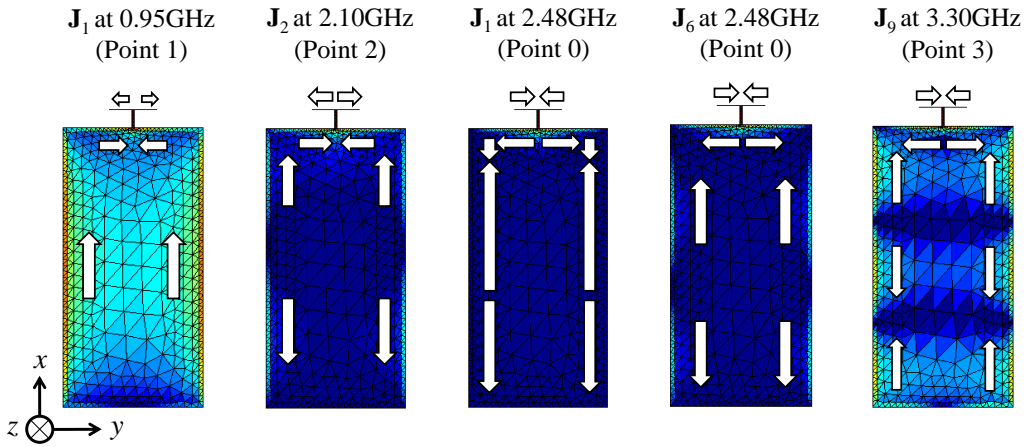


**Fig. 6-24** Normalized power coefficients of the off-ground CCE on the PCB with  $e = 8\text{mm}$  and varying  $d$ .

**Case 4:**  $d = 20\text{mm}$ ;  $e = 8\text{mm}$



**Case 8:**  $d = 60\text{mm}$ ;  $e = 8\text{mm}$

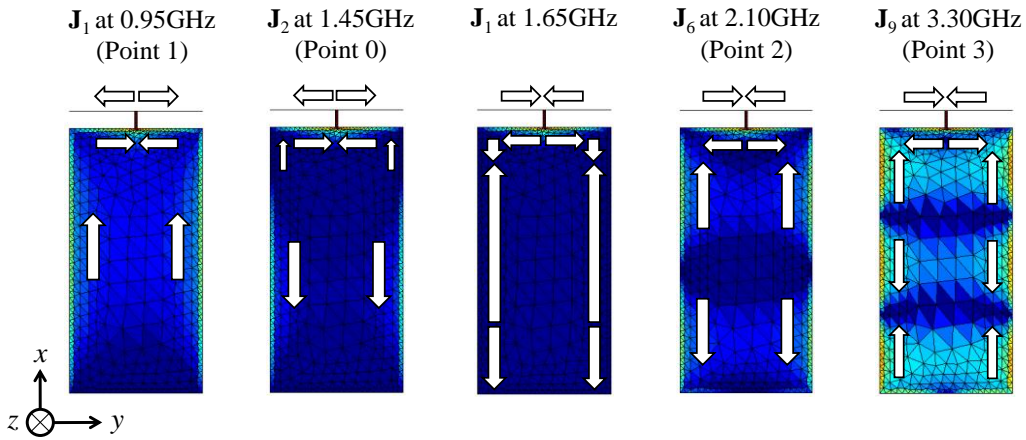


**Fig. 6-25** Normalized current distributions and current schematics of the excited modes  $J_1$ ,  $J_2$ ,  $J_6$  and  $J_9$  at different notable frequency points for case 4 (top) and case 8 (bottom).

As shown in Fig. 6-24, only the cases 4, 5 and 6 have  $\eta'_{J_n} \geq 75\%$  around the 6dB-BW frequency region (see Table 6-3) where the points 0 and 2 are close to each other. The modal contribution  $\eta'_{J_1}$  has more than one maximum in all cases, a fixed one occurs in the low frequency at  $f = 0.95$  GHz (point 1) and the other varying maxima occur at higher frequencies near the point 0. The maxima in the higher frequency are shifting lower (see case 4 to 9), if  $d$  increases, improving the overall power coefficient  $\eta'$  around the self-resonance at point 0 of the system. The point 0 shifts closer to the point 1, where two maxima of  $\eta'_{J_1}$  overlap and improves the coefficient  $\eta'$  due to high contributing of  $\eta'_{J_1}$  in

the low frequency region. As shown in Fig. 6-24, only case 9 has a small frequency region where the normalized power coefficient  $\eta' \geq 75\%$  in low frequency around 1 GHz (compare Table 6-3).

As already shown in the characteristic mode analysis of the simple dipoles in section 4.3.2, the characteristic modes are depending on the antenna shape and on the frequency. Therefore, to give a proper comparison of the excited characteristic modes of the cases 4 and 8 their related current schematics are illustrated at remarkable frequency points, see Fig. 6-25 (top and bottom).

Comparing both cases, the form factor of the CCE reference in case 4 (FF:  $8 \times 6 \times 20 \text{mm}^3 = 960 \text{mm}^3$ ) and in case 8 (FF:  $8 \times 6 \times 60 \text{mm}^3 = 2880 \text{mm}^3$ ) is 3.8 times larger and shifts the modal resonances of the modes low in frequency. In addition, the point 0 of case 4 occurs at  $f = 2.48 \text{GHz}$  and of case 8 at  $f = 1.48 \text{GHz}$  (compare Fig. 6-23 and Table 6-3) and affect the mode coupling at different frequencies depending on the modal current and electric field distributions. As shown in Fig. 6-25 and as expected before, each mode has different current path directions. The current distributions of the modes, here in case 4 and 8, have a mainly sinusoidal magnitude distributions which depends on the electrical length of the whole structure. The total electrical length depends on the length of the major axis of the PCB ( $b = 120 \text{mm}$ ), the length of the half minor axis of the PCB to the feed point ( $a/2 = 30 \text{mm}$ ), the length  $e = 8 \text{mm}$  of the feeding strip and on one outer track of the CCE ( $d/2$ ). Summarized, the maximum length of the current path is in case 4  $l_{\max} = 168 \text{mm}$  and is in case 8  $l_{\max} = 188 \text{mm}$ . The modes  $\mathbf{J}_1$ ,  $\mathbf{J}_2$ ,  $\mathbf{J}_6$  and  $\mathbf{J}_9$  represent a current distributions of half a wavelength, a full wavelength, one-and-half a wavelength and two wavelengths along whole structure respectively, as shown in Fig. 6-25. The high frequency mode  $\mathbf{J}_1$  at point 0 is deformed significantly. The phenomenon of high deformation occurs for the other observed modes at higher frequencies also [CFa07\_2].

In case 4, it can be seen that the current intensities (here for the modes  $\mathbf{J}_1$ ,  $\mathbf{J}_2$  and  $\mathbf{J}_6$ ) appearing around the CCE at about the frequency point 0 are strong, whereas the excited currents appearing on the PCB are weaker. However, the currents on the PCB of the characteristic mode  $\mathbf{J}_1$  at  $0.95 \text{GHz}$  (Point 1) and  $\mathbf{J}_9$  at  $3.30 \text{GHz}$  (Point 3) are strong. This can be lead back to the CCE which is far away from its resonance at these frequency points. It

## 6. Common Excitation of the Characteristic Modes on Small Handheld Devices

can be shown that the current paths of each excited mode depend on the electrical length of the overall structure. This means that the current path of mode  $\mathbf{J}_1$  at low frequencies (here at  $f = 0.95\text{GHz}$ ) is mainly characterized by the major axis of the PCB due to the electrically small CCE. At high frequencies (here at  $f = 2.48\text{GHz}$ ) the deformation of the mode  $\mathbf{J}_1$  increases with frequency in a significant way. Here, the current path becomes longer due to the electrically larger CCE.

In case 8 the self-resonance of the CCE on the PCB (point 0) is located at  $f = 1.45\text{GHz}$  due to the 3.8 times larger form factor of the CCE reference. The current schematic of mode  $\mathbf{J}_1$  in Fig. 6-25 (bottom) is shown for the  $f = 0.95\text{GHz}$  (point 1) and for  $f = 1.65\text{GHz}$  where the second maximum of the  $\eta'_{J_1}$  curve occurs in Fig. 6-24. It can be seen that the current intensity of the mode  $\mathbf{J}_1$  appears at point 1 stronger around the longer CCE and reduces the current intensity on the PCB. This is caused by the longer current path (here:  $l_{\max} = 188\text{mm}$ ). The same deformation of mode  $\mathbf{J}_1$ , compared to case 4, can be observed at  $f = 1.65\text{GHz}$ . Here the deformation is weaker due to the lower observed frequency, which makes the structure electrically smaller. The current schematics of mode  $\mathbf{J}_6$  and  $\mathbf{J}_9$  in case 8 are depicted at  $f = 2.1\text{GHz}$  (point 2) and  $f = 3.2\text{GHz}$  (point 3). It can be seen that the current of the modes on the PCB and around the CCE occur with same intensity due to the non-resonant CCE at these frequency points.

**Case 8:**  $d = 60\text{mm}$ ;  $e = 8\text{mm}$

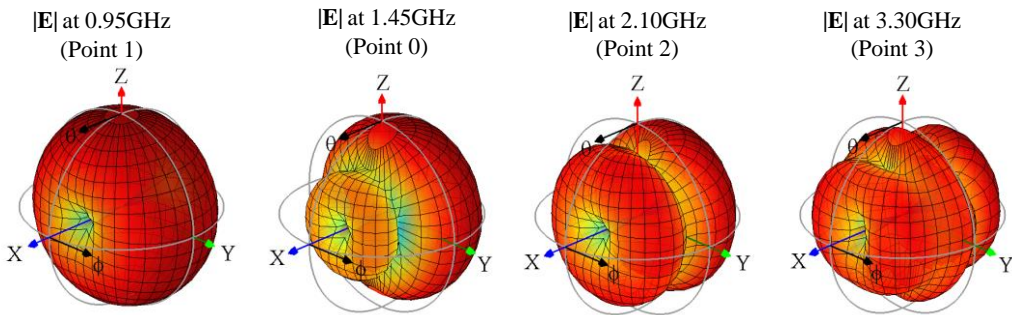


**Fig. 6-26** Calculated 3D radiation pattern at different dominant frequency points for case 8.

Due to the vicinity of the outer tracks of the CCE and to the minor axis of the PCB the fields and the currents around the CCE cancel almost entirely in far distance. However, the imprinted currents on the PCB will excite the characteristic modes and affect heavily

the 3D radiation pattern of the structure, as shown in Fig. 6-26 in case 8. Here the 3D radiation pattern of the dominant points 1, 0, 2 and 3 are illustrated.

In Fig. 6-26 the magnitude of the electric field  $|\mathbf{E}|$  represents the absolute values of the radiation pattern of half a wavelength (point 1), one wavelength (point 2), one-and-half wavelength (point 3) along the  $x$ -axis. The  $|\mathbf{E}|$  at Point 0 represents the absolute value of an asymmetric pattern along the  $x$ -axis. A comparison of the dominant modes (see Fig. 6-25 below) at the observed points shows the direct contribution of the dominant mode currents on the PCB. The current path of mode  $\mathbf{J}_1$  at point 1, mode  $\mathbf{J}_2$  at point 0, mode  $\mathbf{J}_6$  at point 2 and mode  $\mathbf{J}_9$  at point 3 represent the same sinusoidal behavior of a half, a full, an asymmetrical and one-and-half wavelength along the  $x$ -axis on the PCB. It can be concluded that the CCE can be used as an additional matching medium. It improves the absolute power delivered to the antenna as desired without contributing themselves to the radiation. Due to the current cancelation around the slot of the CCE and the PCB only the modal currents on the PCB will affect the 3D radiation pattern.

The last investigation of this section will be the power coefficient improvement in the low frequency range by using the knowledge gained from the earlier investigations in this chapter. As shown above, the larger the outer tracks of the CCE become in length, a better power coefficient can be reached in the low frequency range. We have to make point 0 closer to point 1 to achieve a high power contribution by exciting the lowest order mode  $\mathbf{J}_1$  of the structure efficiently. Therefore, the structure in case 9 is redesigned by shifting the feeding strip (the connection between the CCE and the PCB) to making the CCE unsymmetrical about the major axis of the PCB. Here, the connection is shifted in two steps ( $fp = 40\text{mm}$  and  $fp = 50\text{mm}$ ), as shown in Fig. 6-30. It can be shown that the length  $d$  of the CCE can be separated in two CCE track lengths  $d_1$  and  $d_2$  ( $d_1 > d_2$ ). In both cases the form factor of the CCE and PCB is not changed and a fair comparison to case 9 (see Fig. 6-22) can be made.

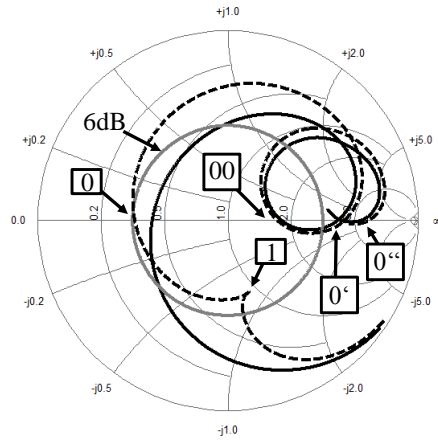
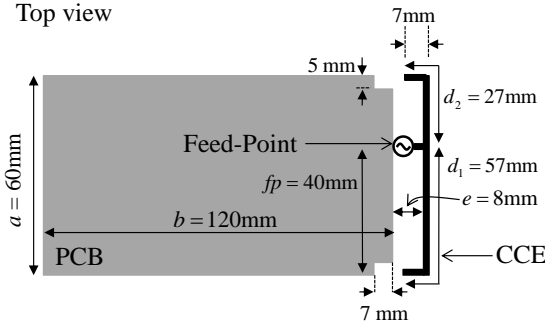
The calculated input impedances of both unsymmetrical cases show that the lowest order mode of the structure improves the radiation of the antenna around Point 1 if the feed point is shifted. The largest normalized power coefficient in low frequency range (at around  $f = 1\text{GHz}$ ) can be achieved if the feed point is shifted to  $fp = 50\text{mm}$  (see Fig. 6-28 right).

## 6. Common Excitation of the Characteristic Modes on Small Handheld Devices

This is mainly caused by the resonance of the longer CCE track with the length  $d_1$ , marked with point 0. Both the self-resonance (point 0) and the mode  $\mathbf{J}_1$  (point 1) results in a power coefficient  $\eta' \geq 75\%$  by increasing the radiation resistance at that frequency region (compare Fig. 6-27 and Fig. 6-28).

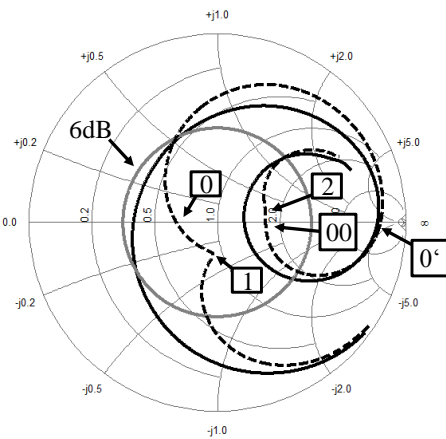
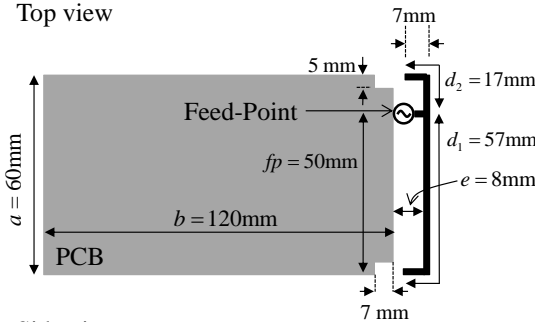
### Unsym. CCE: $fp = 40\text{mm}$

Top view



### Unsym. CCE: $fp = 50\text{mm}$

Top view



--- CCE Antenna  $Z_{in}$     — Reference  $Z_{in}$

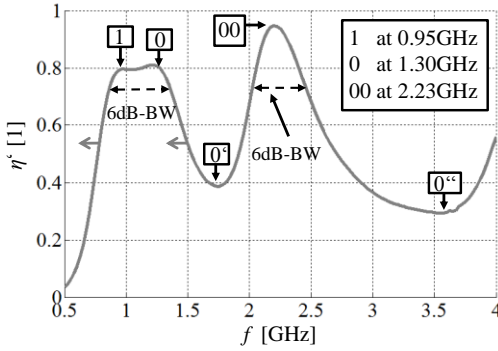
**Fig. 6-27** Calculated input impedances (right) of the unsymmetrical CCE with a feed point shifting of  $fp = 40\text{ mm}$  (top-left) and  $fp = 50\text{ mm}$  (bottom-left).

In addition, as shown in Fig. 6-27 a second self-resonance of the structure at point 00 within the  $-6\text{dB}$  circle can be achieved. This resonance is caused by the smaller CCE track with length  $d_2$  and results in a high power coefficient at around  $f = 2.23\text{GHz}$  (see Fig. 6-28 left) and  $f = 2.7\text{GHz}$  (see Fig. 6-28 right). It can be observed that the smaller the second

## 6.4 Capacitive excitation of characteristic modes by using off-ground elements

CCE track in length is, the higher the second power coefficient maximum shifts in frequency. By this means the CCE couples with higher order modes resulting in a broader 6dB-BW (see Fig. 6-28 right at points 00 and 2). Each example results in a dual-broadband CCE antenna, as shown in Fig. 6-28 left and right.

Unsym. CCE:  $fp = 40\text{mm}$



Unsym. CCE:  $fp = 50\text{mm}$

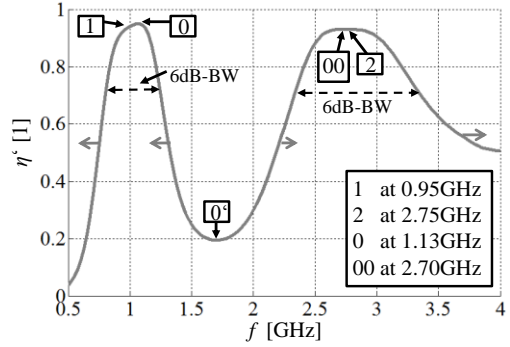


**Fig. 6-28** Normalized power coefficients of the unsymmetrical CCE from Fig. 6-27.

The obtained results in this chapter underline the different strategies for common mode excitation. By using different kind of off-ground CCEs several modes were excited to achieve a good broadband antenna. It showed how the location and the design of the coupling element affect the mode coupling, the absolute power contribution to the antenna and the radiation pattern.





# Chapter 7

## Applications on Small Antenna Design

Typically, in small terminal applications the antenna concept is chosen such that it uses the chassis of the terminal as a counterpoise for the antenna element. In the previous chapters 5 and 6 it has already been proven that the chassis can efficiently be used to design a desired antenna on the mobile terminal itself. Consequently, results in [Man09, Mar10\_1, Mar10\_2] show that the correlation of two elements on a shared chassis is significantly affected by the electrical size of the chassis and the location of the elements on the chassis. On the other hand, the dominant role of the chassis can be utilized to excite orthogonal chassis modes in a separate (see chapter 5) or common (see chapter 6) way in order to operate essentially as a multiple port or broadband antenna system.

Chapter 5 has demonstrated the advantage of the selective excitation of the characteristic modes on the chassis using distributed ICEs efficiently. Chapter 6 has demonstrated that off-ground CCEs have the advantage to excite a multiple set of modes resulting in broadband matched input impedance at low and/ or high frequency. Both concepts are used to evaluate efficient small multiple port or broadband antenna system. The performance of the systems are evaluated by measurements and simulations on the matching, the electromagnetic (EM) isolation, the envelope correlation and the total efficiency.

In section 7.1 a 3-port antenna system based on the selective excitation of the first three chassis modes by using three sets of ICEs will be evaluated [I, II, III, V]. In section 7.2 an off-ground CCE concept will be evaluated and used to design a matched LTE-A handset antenna enabling the excitation of all available modes on the chassis [VI, VII]. In section 7.3, a 2.6GHz multiple antenna system consisting of an off-ground CCE and an out-of-

phase ICE to excite different sets of orthogonal modes will be evaluated [III, IV]. The last section 7.4 of this chapter will evaluate a multi antenna system consisting of a tuneable CCE antenna and two self-resonant capacitive feed coupling elements (CFCEs) for small terminals [VII, VIII].

### 7.1 3-port antenna design based on a selective inductive excitation

<sup>1</sup>Recent mobile terminals for the 4th generation aims for higher data rates which can be realized by multiple antenna systems and MIMO technology [SHe08, Vau87, Li10, Fos98]. Most approaches to realize such multi antenna systems on small terminals are based on the arrangement of different antenna elements on small terminals in order to obtain high EM isolated antenna ports. Frequently stated design rules are e.g. to separate the antennas by the largest available distance to each other or to use de-polarized antenna elements. Another possible method to reduce mutual coupling is to include certain chokes or specific filter structures. By this the currents flowing between the elements on the common ground of the chassis are reduced. In this content some concepts published in literature are summarized in [Lux10].

However, none of the concepts and design rules above consider adequately the antenna integration conditions on the common ground of the chassis. In [Man09, Mar10\_1, Mar10\_2] we have already shown that the common chassis plays a dominant role in terms of the correlation of the antenna elements. Moreover we have proven that separating the antenna elements by the largest available distance might not be a sufficient design rule in case of small terminals. Moreover, we have to consider the different orthogonal characteristic modes excited on the chassis by the antenna elements.

On the other hand the characteristic modes offer interesting properties for MIMO itself, as they are orthogonal to each other, as shown in section 2.2 and 2.3. Concepts for the excitation of the characteristic modes on the small terminal have been published in [Cha10, KKi13, Hui14]. For example in [Cha10] miniature off-ground CCEs are located in the

---

<sup>1</sup>This section uses textual materials and figures from [I, II] © IEEE 2011, [III] © IEEE 2012, [V] © IET 2014.

corners of the PCB to realize a four port antenna system.

In [Man11, I, II] and section 5.5 we have presented a concept using ICEs for the selective excitation of different characteristic modes. The basic concept of that 3-port antenna system is shown in Fig. 7-1 [V].

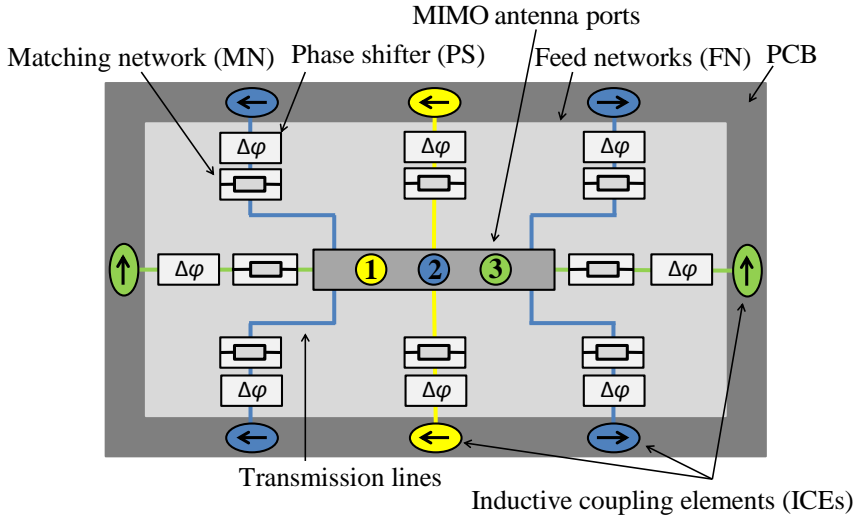


**Fig. 7-1** Concept of the 3-port antenna system based on the selective inductive mode excitation on the same rectangular plate. © 2012 IEEE [III], Reproduced by permission of the IET [V].

The encapsulated tuning module may consist of MN (Matching Networks), PD (Power Dividers) and PS (Phase Shifters) and, together with transmission lines that connect the individual ICEs, builds the FNs (Feed Networks) for three sets of  $ICE_{J_n}$  couplers. As shown in Fig. 7-1, port 1 is marked in yellow, port 2 is marked in blue and port 3 is marked in green. There are in total 8 ICEs belonging to 3 different sets of couplers  $ICE_{J_n}$ . Each set builds an arrangement to excite a specific mode  $J_n$  and is connected to one port of the multi antenna system.

To evaluate the basic concept the dimensions of the PCB will be fixed to the already investigated rectangular plate ( $60\text{mm} \times 120\text{mm}$ ), as shown in section 5.1. In our example, the desired frequency of operation is centred to  $f_{op} = 2.5\text{GHz}$ . Fig. 5-1 (left) shows the eigenvalues  $\lambda_n$  of the obtained characteristic modes  $J_n$ . With respect to the concept we focus on the first three modes  $J_1$ ,  $J_2$  and  $J_3$ . At the operation frequency  $f_{op} = 2.5\text{GHz}$  these modes can be selectively excited, as proven in section 5.5, and they have low eigenvalues

## 7. Applications on Small Antenna Design

$|\lambda_n| \leq 1$  ( $|\lambda_1(f_{op})| = 0.3$ ,  $|\lambda_2(f_{op})| = 0.18$ ,  $|\lambda_3(f_{op})| = 0.39$ ). Due to the low eigenvalues at  $f_{op} = 2.5\text{GHz}$  these modes can be matched with reasonable effort (see Fig. 5-15), while those with large eigenvalues  $|\lambda_n| \gg 1$  are quite difficult to match to  $50\Omega$ .

Fig. 7-2 illustrates the modal current distributions of the first three characteristic modes  $\mathbf{J}_1$ ,  $\mathbf{J}_2$  and  $\mathbf{J}_3$  at the edges of the major and minor axes on the PCB at the operation frequency  $f_{op} = 2.5\text{GHz}$ . It shows that the maxima and minima of the current distribution of each characteristic mode are located at specific positions. As proven in section 5.5, a desired mode can be excited by distributed ICEs located at the local maxima of the current distribution.

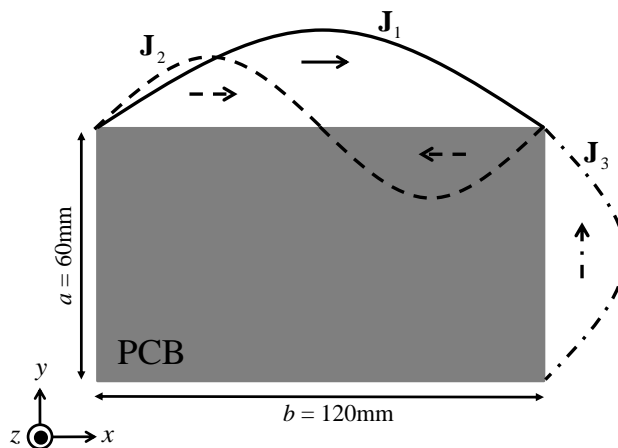


**Fig. 7-2** Superimposed surface current distribution of the modes  $\mathbf{J}_1$ ,  $\mathbf{J}_2$  and  $\mathbf{J}_3$  at  $f_{op} = 2.5\text{GHz}$ . Reproduced by permission of the IET [V].

A configuration of inductive couplers of an ICE-multiport antenna is illustrated in Fig. 7-3. According to section 5.5, the familiar ICEs with FF-1 are mounted at the edges of the PCB at locations where the maxima of the current distribution of the desired modes appear. The individual ICEs must be adjustable by their phase depending on the desired mode at  $f_{op} = 2.5\text{GHz}$ , as shown in Fig 7-2 and 7-3. The excitation of mode  $\mathbf{J}_1$  can be achieved by exciting both couplers of the  $\text{ICE}_{\mathbf{J}_1}$  in-phase together. For the excitation of mode  $\mathbf{J}_2$  two of the four  $\text{ICE}_{\mathbf{J}_2}$  have to be excited in phase together and the other two  $\text{ICE}_{\mathbf{J}_2}$  have to be driven  $180^\circ$  out-of-phase together. Mode  $\mathbf{J}_3$  can be excited by driving both  $\text{ICE}_{\mathbf{J}_3}$  in-phase together.

The entire 3-port antenna system including the feed network is realized with a seven-layer

PCB. Fig. 7-3 shows the conceptual design of the feed networks (FN) for each port. Each FN is designed and evaluated in stripline technology, as investigated in [III, V].

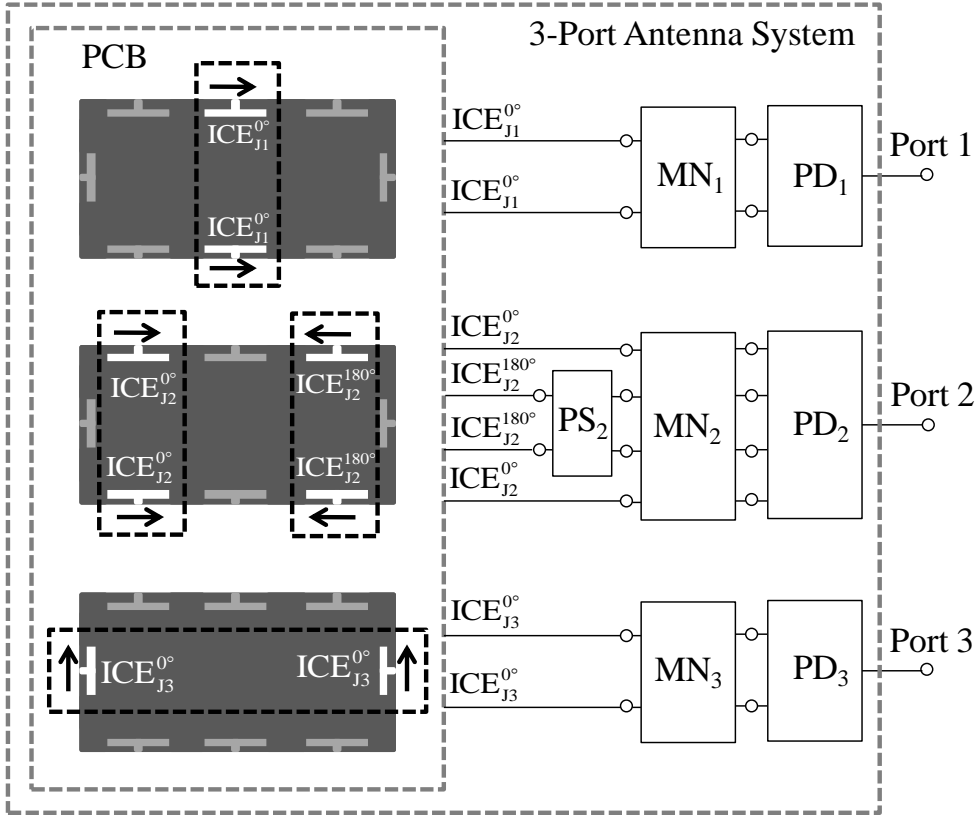


**Fig. 7-3** Schematic of a 3-port antenna including feed networks for the selective excitation of three characteristic modes on a small terminal PCB. Reproduced by permission of the IET [V].

Each PD ( $\lambda/4$ -transformer) evenly divides the power belonging to the set of couplers  $ICE_{Jn}$  to a  $50\Omega$  stripline. Each  $MN_n$  consists mainly of short-circuited and open-circuited stubs in stripline technology with specific lengths, as investigated in [III, V]. The general short- and open circuit tuning was introduced in [Win44]. The matching of the three antenna port impedances can be achieved by varying the lengths of the matching stubs and the transmission lines [III]. The entire realized feeding networks for the selective excitation of the desired modes are evaluated at  $f_{op} = 2.5\text{GHz}$  and shown in [V]. The broadband matching of such a 3-port system is evaluated in [Had13].

Based on the simulated model presented in [V] a prototype based on a 7-layer Rogers

## 7. Applications on Small Antenna Design

RO4003C laminate (see Fig. 7-4) has been fabricated and evaluated. The coaxial connectors for feeding the three ports were placed in locations where the influence on the modal current distributions ( $\mathbf{J}_1$ ,  $\mathbf{J}_2$  and  $\mathbf{J}_3$ ) is minimal (compare Fig. 5-2 and Fig. 7-4).

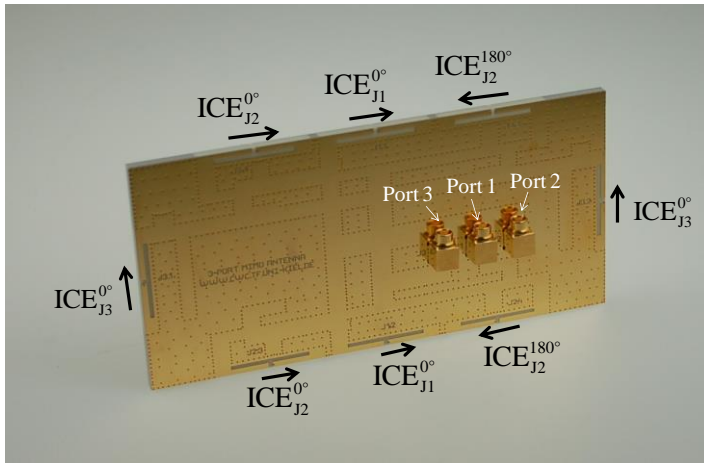


**Fig. 7-4** The 3-port antenna prototype. Reproduced by permission of the IET [V].

The  $s$ -parameters obtained of the prototype are shown in Fig. 7-6.

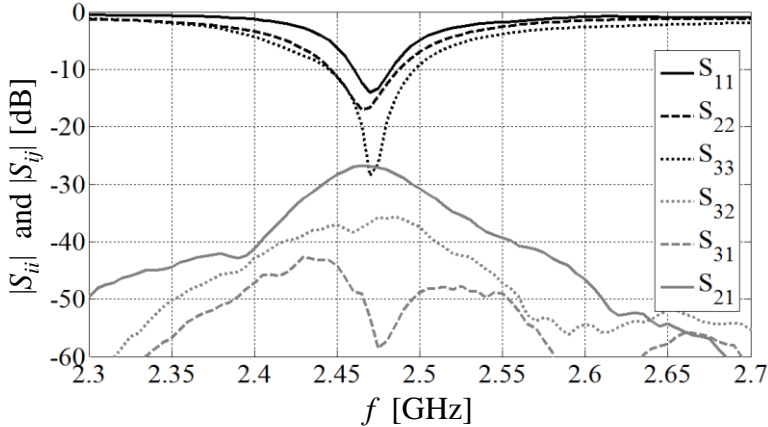


**Fig. 7-5** The  $s$ -parameters of the 3-port antenna prototype. Reproduced by permission of the IET [V].

The comparison of the measured  $s$ -parameters (Fig. 7-5) and the simulated  $s$ -parameters in [V] show a good agreement. However, there is a slight shift by  $\Delta f = 1.2\%$  of the resonance frequency. This can be explained by material tolerances of the Rogers laminate. Therefore, we have decided to do the evaluation of the antenna system at  $f = 2.47\text{GHz}$ .

The measured EM isolation between the ports is  $|S_{ij}| \geq 27\text{dB}$  for all modes.

The antenna radiation measurements were performed in an anechoic chamber using a spectrum analyzer as receiver and a wireless transceiver module as transmitter. The results are shown in Fig. 7-6. The wireless transceiver module RFM70 [RFM14] has been used in order to avoid any unwanted cable effects that may arise when the small terminal device is fed by a coaxial cable. The effects on the modal current distribution and its radiation pattern are evaluated in [Man13]. As shown in Fig. 7-6, the combined transceiver module and the required lithium-ion battery [Ren14] has a small form-factor of  $(30 \times 20 \times 8\text{mm}^3)$  and both are located in an uninfluential position with respect to the modal current distribution (compare Fig. 5-2).

Fig. 7-6 shows the measured 3D radiation patterns of the three modes of the realized prototype. A comparison of the radiation patterns in Fig. 5-3 show that only minor effect on the radiation pattern occur by placing the transceiver module in that uninfluential position [Man13].

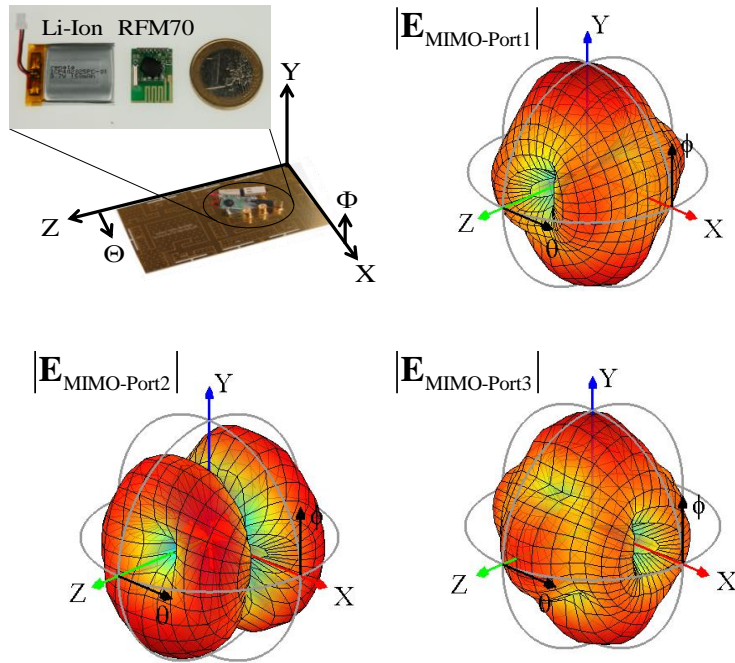


**Fig. 7-6** Measured radiation pattern of the 3-port antenna prototype at  $f = 2.47\text{GHz}$ . [RFM14, Ren14] Reproduced by permission of the IET [V].

## 7. Applications on Small Antenna Design

It can be observed that the measured patterns  $|\mathbf{E}_{\text{MIMO-Port1}}|$ ,  $|\mathbf{E}_{\text{MIMO-Port2}}|$  and  $|\mathbf{E}_{\text{MIMO-Port3}}|$  of the three ports fairly coincide with the expected canonical modes (compare Fig. 5-3). In order to give a quality measure of the modal excitation the cross-correlations between the canonical modes  $\mathbf{J}_n$  (based on the TCM ( $|\mathbf{E}_{Jn}|$ )) and the entire radiation pattern of the measured mode  $|\mathbf{E}_{\text{MIMO-Port } n}|$  of the prototype is calculated by

$$|\rho_{\mathbf{E}_{Jn}, \mathbf{E}_{\text{MIMO-Port } n}}| = \frac{\iint |\mathbf{E}_{Jn}| \cdot |\mathbf{E}_{\text{MIMO-Port } n}| dA}{\sqrt{\iint |\mathbf{E}_{Jn}|^2 dA} \cdot \sqrt{\iint |\mathbf{E}_{\text{MIMO-Port } n}|^2 dA}}. \quad (7.1)$$

At this point it should be noticed that because of the measurement setup, only the magnitudes of the radiation patterns could be used in the calculation. Therefore, the correlation coefficient does not represent the full complex far-field patterns. Nevertheless, it represents a fair measure to evaluate the similarity of the patterns, as shown in Table 7-1, and proves the applicability of the used transceiver module [Man13, V].

**Table 7-1** Cross-correlation between the radiation pattern of the canonical mode and the 3-port antenna prototype.

$ \rho_{J1, \text{MIMO-Port1}} $	$ \rho_{J2, \text{MIMO-Port2}} $	$ \rho_{J3, \text{MIMO-Port3}} $
0.93	0.99	0.85

The total efficiency, taking into account mismatch and losses, was calculated from the measured 3D far field patterns. Table 7-2 shows that they are reasonable high in all three cases. Notice that with real applications, such as commercial mobile phones, other components and materials will further decrease the total efficiency.

**Table 7-2** The measured total efficiency of the 3-port antenna system.

$\eta_{\text{tot, MIMO-Port 1}}$	$\eta_{\text{tot, MIMO-Port 2}}$	$\eta_{\text{tot, MIMO-Port 3}}$
62%	79%	75%

This section has shown a systematic application of the TCM to design a multi antenna



system for a small terminal. In terms of envelope correlation, port isolation and antenna efficiency the results achieved are promising with respect to the adaptation of the concept to a real implementation. The size and location of the couplers offer clear potential to be extended to a more port system. As an outlook, the feed networks could be integrated in a encapsulated tuning module enhancing the compactness of the system.

It has been shown that for a typical size mobile terminal at least three chassis modes can be excited efficiently. At higher frequencies, or for larger terminal sizes, more modes with low eigenvalues are available and the concept can be extended to more antenna ports easily.

## 7.2 Broadband matched hybrid coupling element (HCE)

<sup>2</sup>The investigations of the chapter 6 and section 7.1 have shown that the TCM offers interesting features with respect to design multiple antenna systems on small terminals. However, these concepts are based on the selective excitation of the existing orthogonal modes while the resulting bandwidth is limited. In order to fulfill all aspects of the 4<sup>th</sup> communications standards, the compact antenna design for broadband applications plays an important role in the development process of a modern mobile phone.

One possible implementation of a broadband matched LTE-A antenna is based on a common excitation of several characteristic modes [VI]. Therefore, the design goal for a wide-band/multiband antenna is to provide modes with low eigenvalues in the desired frequency range and match them to the port impedance of the antenna efficiently. In addition an efficient excitation of the modes requires an impedance matching, which can be realized by modifying the antenna geometry. Based on that approach additional imprinted currents which are excited on the PCB can be used for impedance matching passively, i.e. the coupling structure itself. This approach has already been proven by using self-resonant off-ground CCEs, as shown in section 6.4 and [V, VI].

The three desired LTE-A bands in this section are the low-band (698MHz - 960MHz), the

---

<sup>2</sup>This section uses textual materials and figures from [VI] © IEEE 2014, [VII] © IEEE 2015.

## 7. Applications on Small Antenna Design

middle-band (1.71GHz - 2.17GHz) and the high-band (2.50GHz - 2.69GHz). Especially the low-band is very challenging to achieve the required impedance matching.

Fig. 7-7 shows the consecutive design steps of a hybrid coupling element (Fig. 7-7 b - d) which is capable of providing the desired modal excitation on the chassis. The steps are based on manipulating the modes by modifying the coupling element structure so that the given and the additional mode resonances are shifted to the desired frequency ranges.

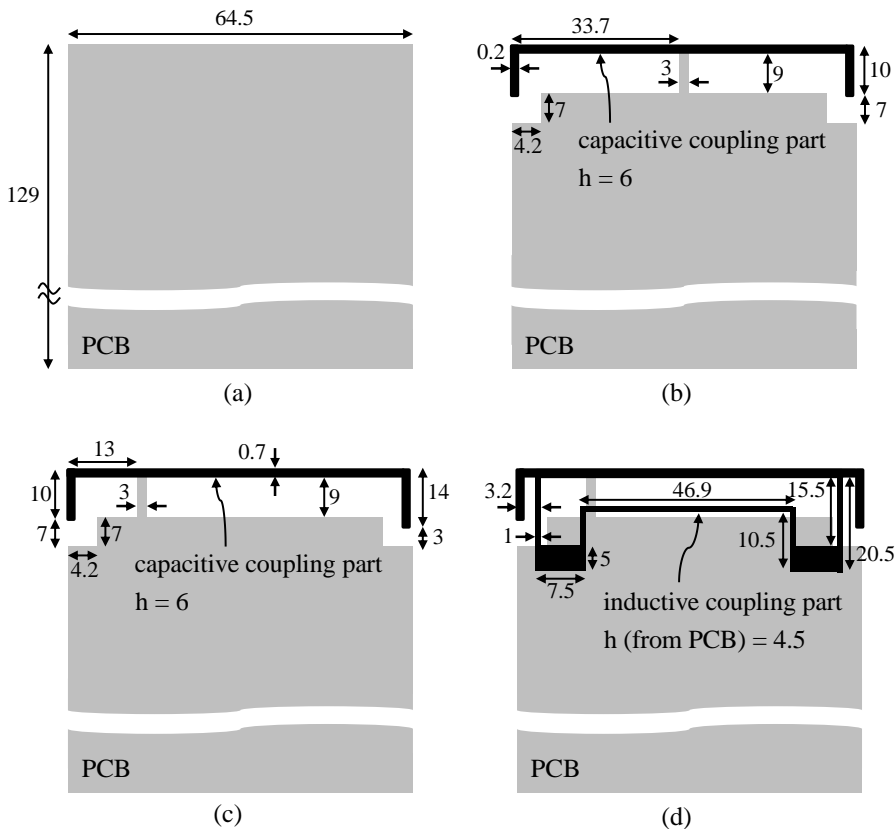


**Fig. 7-7** Simplified small terminal (a), the symmetrical capacitive- (b), the unsymmetrical capacitive- (c) and the hybrid coupling element (d). Dimensions are in mm. © 2014 IEEE [VI].

The respective eigenvalue analysis of all four design steps without an internal excitation are shown in Fig. 7-8. The eigenvalue investigation starts with a small rectangular terminal (Fig. 7-7 a and Fig. 7-8 a). It shows that only  $\mathbf{J}_1$ ,  $\mathbf{J}_2$ ,  $\mathbf{J}_3$  and  $\mathbf{J}_4$  have low eigenvalues in the observed frequency range. The mode  $\mathbf{J}_3$  has its resonance in the high-band frequency range. As shown in sub-section 6.4.2, the operation of the symmetrical CCE at the low-

band is based on the effective excitation of  $\mathbf{J}_1$  of the small terminal. Hence, in order to effectively shift the mode  $\mathbf{J}_1$  to the low-band the coupling element is placed on top of the short edge of the small terminal as shown in Fig. 7-7 b. It is known from chapter 6 that the CCE needs to be located in an electric field maximum of the respective chassis modes. Here, the major axes modes  $\mathbf{J}_1$ ,  $\mathbf{J}_2$ , and  $\mathbf{J}_3$  and their electric field maxima are located at the short edges of the chassis, especially near the corners. As shown in Fig. 7-8 b,  $\mathbf{J}_1$  and  $\mathbf{J}_3$  have their resonance in the low- and middle-band. The resonance of mode  $\mathbf{J}_2$  occurs between the low- and middle-band. The drastic deformation of the mode  $\mathbf{J}_1$  results in a narrow impedance bandwidth in the low-band if only this mode is excited. Therefore, the structure will be redesigned by shifting the feed-strip between the CCE and the PCB (un-symmetrical CCE).

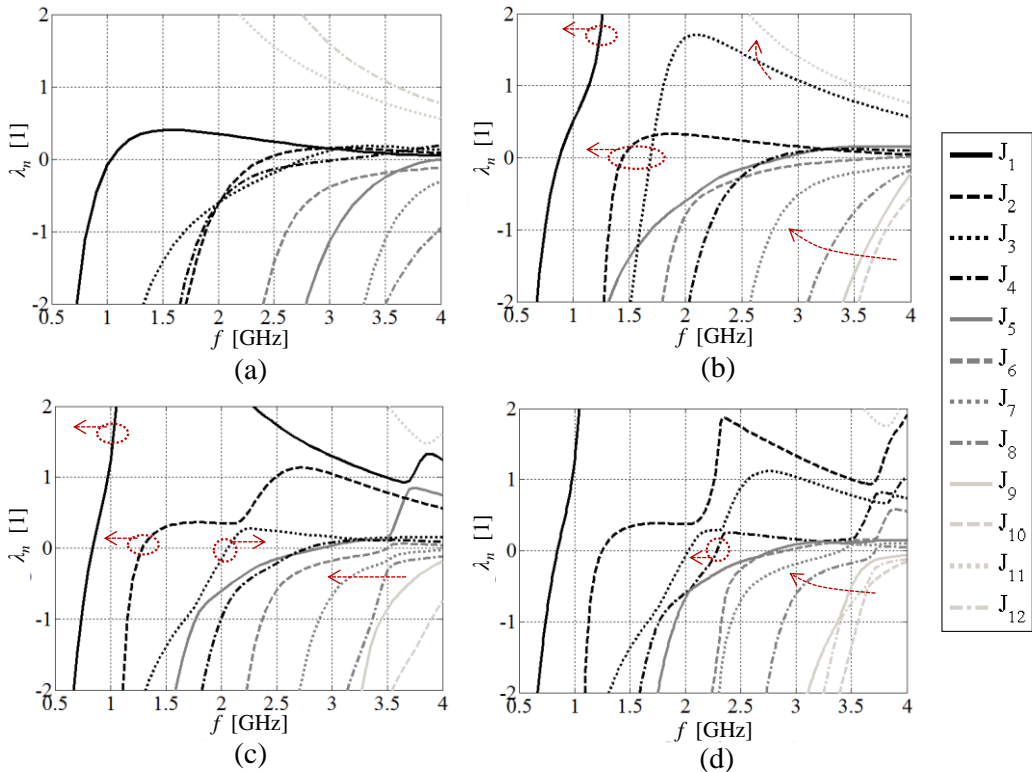


**Fig. 7-8** Eigenvalue analysis of the small terminal (a), the symmetrical capacitive- (b), the unsymmetrical capacitive- (c) and the hybrid coupling element (d), [VI]. Mode order of each structure sorted by their resonances ( $\lambda_n = 0$ ). © 2014 IEEE [VI].

As a result, the modal resonance of mode  $\mathbf{J}_2$  is shifted down closer to mode  $\mathbf{J}_1$  (see Fig.

## 7. Applications on Small Antenna Design

7-8 c). Thereby both modes can be used to widen the impedance bandwidth in the low-band, as already evaluated in sub-section 6.4.2 (see Fig. 6-27 and Fig. 6-28). In addition, higher order modes (here:  $J_{5-10}$ ) are shifted down in frequency and enable a broadband matching the high band. Including the internal excitation (compare Fig. 6-28), such an unsymmetrical structure results in a dual-broadband antenna system, but cares not for the desired bandwidth within the desired frequency bands. Therefore, an additional design step for modifying the antenna geometry is required.

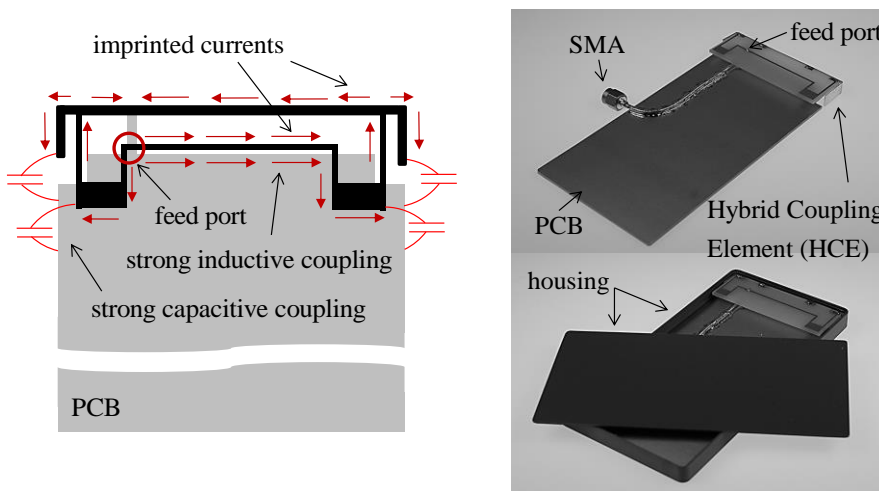


**Fig. 7-9** The prototype of the off-ground HCE mounted beyond the PCB (right) and the principle capacitive and inductive coupling and imprinted currents (left). © 2014 IEEE [VI]. © 2015 IEEE [VII].

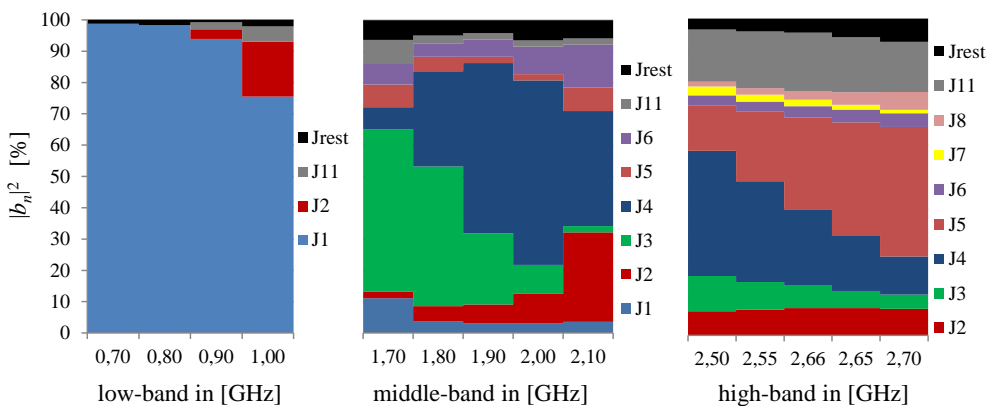


**Fig. 7-10** Percentage radiation ratios of the different excited characteristic modes of the HCE antenna. © 2014 IEEE [VI].

In order to increase the bandwidth in the high band, the coupling element needs to be redesigned in such a way that all of the available modes with low eigenvalues in the high band are excited. This is achieved by an additional bended ICE track which affects the excitation of the same co-located modal current distributions of the respective modes in the middle of the short edge significantly (see Fig. 7-9 right). As shown in Fig. 7-7 d, the additional inductive loop (ICE) is connected to the CCE. By doing this, the resonance of mode  $\mathbf{J}_5$  is shifted in the high-band (see Fig. 7-8 d). The resonance of mode  $\mathbf{J}_4$  occurs now between the middle- and high-band. The higher order modes (here:  $\mathbf{J}_{7-10}$ ,  $\mathbf{J}_{12}$ ) are shifted towards lower frequencies which results mainly in low eigenvalues in the high-band. The optimal excitation of the required modes is realized by the internal feeding port which is connected with the CCE and the additional ICE part as marked in Fig. 7-9 (right).

In order to prove that a wider bandwidth is obtained by the hybrid coupling element, the percentage power budget (see (4.32)) of each mode is calculated and shown in Fig. 7-10 for the low-, middle- and high-band. The power budget of the modes can be calculated by the formulation derived in [Aus98, Saf12, Saf13]. It can be observed in that the HCE excites all available modes according to Fig. 7-8 d in the desired three LTE-A bands. As shown in Fig. 7-10, the main excited modes for low-band are  $\mathbf{J}_1$  and  $\mathbf{J}_2$ , for the middle-band are  $\mathbf{J}_3$  and  $\mathbf{J}_4$  and for the high-band are  $\mathbf{J}_4$  and  $\mathbf{J}_5$ .

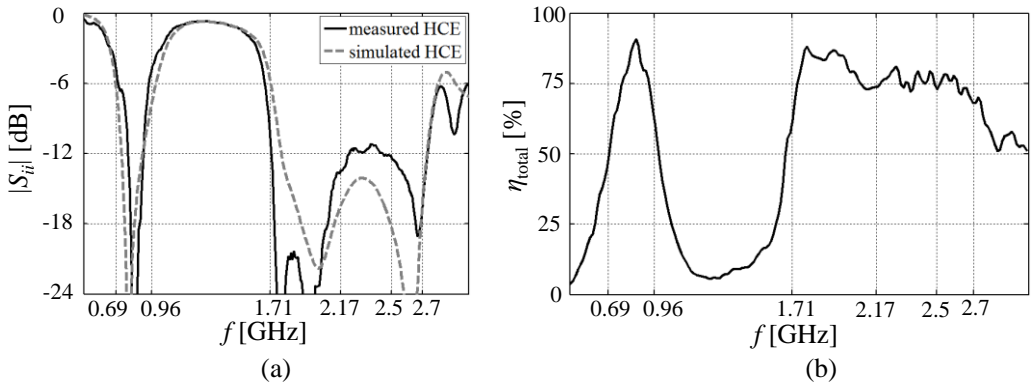


**Fig. 7-11** The s-parameter (left) and the total efficiency (right) of the HCE prototype. © 2015 IEEE [VII].

At first the proposed design has been implemented using the FDTD-based EM software Empire XCell [Emp15]. The prototype is realized on a FR4 substrate enclosed by a typical

plastic housing (see Fig. 7-9 right). The material of the housing is PVC ( $\epsilon_r = 2.91$ ,  $\tan(\delta) = 0.025$ ) with the outer dimensions  $133 \times 68 \times 8\text{mm}^3$ . The fabricated prototype without and with the plastic housing are shown in Fig. 7-9 right. All results, shown in Fig. 7-11, are based on the fabricated mock-up system.

Fig. 7-11 (left) shows the measured reflection coefficient of the mock-up system in comparison to the simulation results. By using the typical impedance matching criterion  $|S_{11}| \leq -6\text{dB}$ , it can be seen that the proposed HCE antenna is adequately matched at the low-band (698MHz - 960MHz) and the high-band (1.71GHz - 2.69GHz). Both frequency bands cover the LTE E-UTRA operation bands 1 - 10 and 12 - 14 with a measured total efficiency of at least  $\eta_{\text{total}} = 75\%$  in free-space. Comparing the measured total efficiency of the HCE with the normalized power coefficient of the unsymmetrical CCE (see Fig. 6-28) a broader matched range in the high-band can be reached. Therefore, the hybrid coupling element can be classified as a broadband matched antenna.

This section has shown a systematic application of the TCM for the design of an efficient broadband antenna system for a small terminal and fulfill all aspects of 4G communications standards [SHe08].

### 7.3 2-port antenna based on a tuned unsymmetrical CCE and a distributed pair of ICEs

<sup>3</sup>The CCE, which is the main antenna, should be broadband and excite different modes compared to the secondary antenna (the ICE pair). Such a novel MIMO antenna system for a mobile terminal is studied and the optimal locations of the antenna elements are evaluated with the help of the TCM [II, III, IV]. Hence, by exciting the separate orthogonal modes with the separate antenna elements, both the EM isolation and the envelope correlation between the antennas can be optimized in order to achieve a good MIMO performance. The multiple antenna evaluation frequency range is fixed to the E-UTRA operation band 7 (2.5GHz - 2.69GHz).

The design of the main antenna has the bandwidth requirement of the lowest frequency

---

<sup>3</sup> This section uses textual materials and figures from [IV] © IEEE 2013.

7.3 2-port antenna based on a tuned unsymmetrical CCE and a distributed pair of ICES band at 0.69GHz - 0.96GHz. At that frequencies it is typically very challenging to achieve adequate impedance bandwidth. The operation of the CCE at the low-band is based on the effective excitation of the lowest-order (half-wave) characteristic mode, as shown in subsection 6.4.2. Hence, in order to excite the lowest-order mode effectively, the main antenna is placed beyond the short edge of the chassis as shown in Fig. 7-12. Furthermore, the shape of the CCE and the location of the feeding pin are optimized in a way that it creates two self-resonances, one in the low-band (here: 0.69GHz - 0.96GHz) and one in high-band (here: 1.71GHz - 2.7GHz) (compare Fig. 6-27 and Fig. 6-28). In order to ensure a sufficient impedance matching, lumped-element matching circuits are applied at both bands. The matching circuits is discussed later in this section.

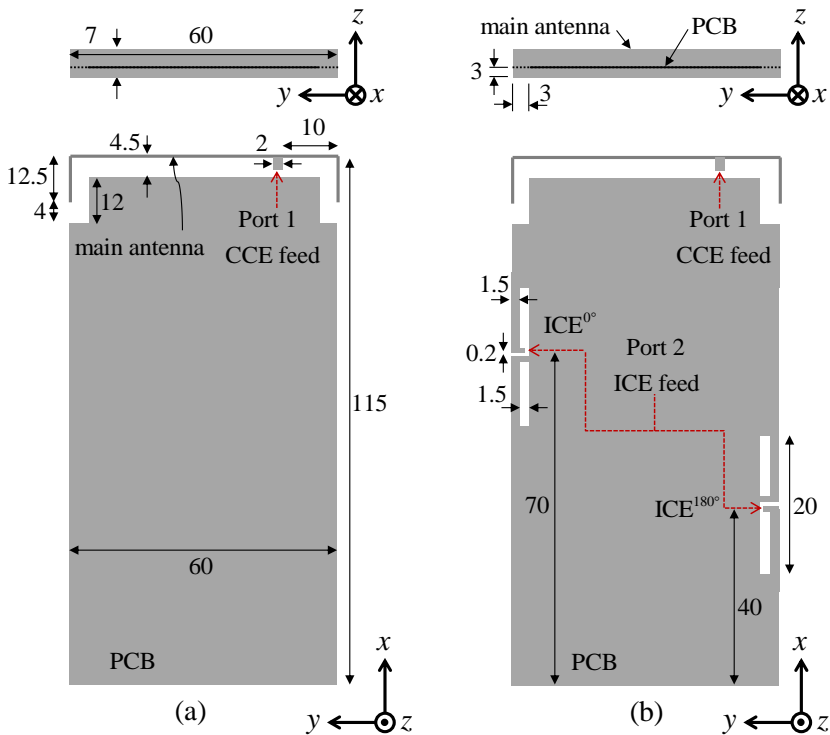


**Fig. 7-12** Simplified small terminal with only the main antenna (a) and with the secondary antenna (b). Dimensions are in mm. © 2013 IEEE [IV].

The eigenvalue analysis of the simplified small terminal taking only the main antenna (see Fig. 7-12 (a)) into account is shown in Fig. 7-13. It can be seen that only few modes provide low eigenvalues at the desired frequency (here: 2.5 - 2.7GHz).

The characteristic modes excited by the main antenna (Port 1 in Fig. 7-12 (a)) are studied.

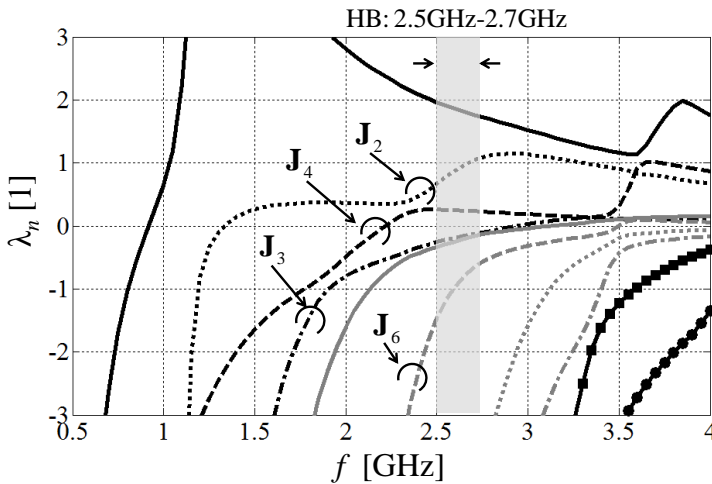


**Fig. 7-13** Eigenvalue analysis of the unsymmetrical CCE [IV]. Mode order of each structure sorted by their resonances ( $\lambda_n = 0$ ). © 2013 IEEE [IV].

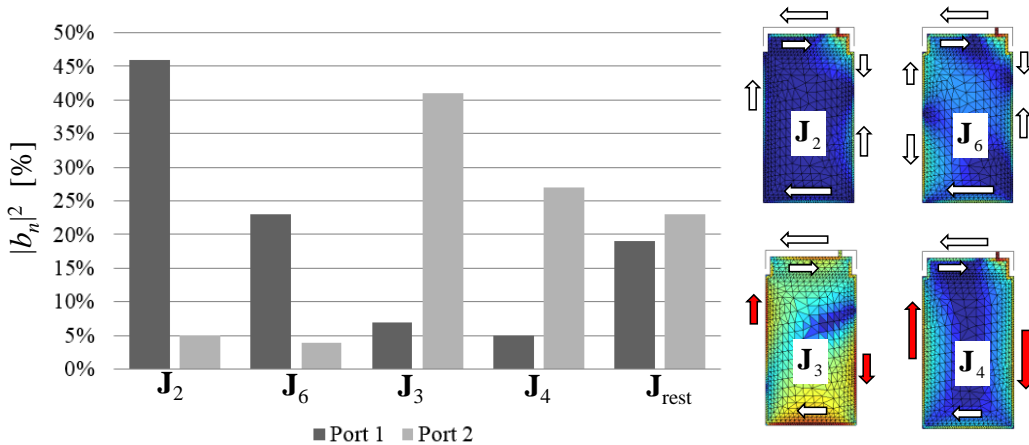


**Fig. 7-14** Percentage contribution (left) of the different modes (right) of the unsym. CCE at 2.6GHz. Port1 stands for the main antenna and Port2 stands for the secondary antenna. © 2013 IEEE [IV].

The simplified main antenna structure (shown in Fig. 7-12 (a)) is used in the characteristic mode study. This analysis reveals which characteristic modes are effectively excited by the main antenna and which modes are not excited. Then, the secondary antenna can be designed in such a way that the excited modes do not interfere with those one of the main antenna. This design strategy is assumed to lead to a good MIMO performance based on the earlier results in this thesis. Based on the TCM analysis in Fig. 7-14, two of the most



### 7.3 2-port antenna based on a tuned unsymmetrical CCE and a distributed pair of ICES

dominant characteristic modes ( $\mathbf{J}_2$  and  $\mathbf{J}_6$ ) excited by the main antenna at 2.6GHz are responsible for  $|b_2|^2 + |b_6|^2 = 68\%$  of the total radiation of the main antenna. The respective current maxima (arrows) and current nulls (blue) of the excited modes  $\mathbf{J}_2$  and  $\mathbf{J}_6$  are shown in Fig. 7-14 (right). The rest is radiated by the minor characteristic modes, from which the next two modes radiate  $|b_3|^2 = 7\%$  ( $\mathbf{J}_3$ ) and  $|b_4|^2 = 5\%$  ( $\mathbf{J}_4$ ), and the rest of the modes  $\mathbf{J}_{\text{rest}}$  account for less than  $|b_{\text{rest}}|^2 = 1\%$  each (together about 19%).

The placement of the secondary antenna is presented in Fig. 7-12 (b). The selection is based on the TCM analysis and the current distributions shown in Fig. 7-14. It is obvious that in order to guarantee a good MIMO performance, the second antenna should not strongly excite the two most dominant characteristic modes of the main antenna ( $\mathbf{J}_2$  and  $\mathbf{J}_6$ ). However, it should excite modes with low eigenvalues (see Fig. 7-13).  $\mathbf{J}_3$  and  $\mathbf{J}_4$  contribute  $|b_3|^2 + |b_4|^2 = 12\%$  of the radiation of the main antenna only and are therefore good candidates. As we remember from section 5.5 and 7.1, the distributed ICES can efficiently excite the wanted mode when the element(s) are placed with an appropriate phasing at a current maximum. Hence, the optimal locations of the ICE antennas are positioned in such a way that the modes  $\mathbf{J}_3$  and  $\mathbf{J}_4$  have the current maximum and the modes  $\mathbf{J}_2$  and  $\mathbf{J}_6$  have the current minimum at the same location. In addition, the inductive coupling elements must be fed  $180^\circ$  out-of-phase, since the modes  $\mathbf{J}_3$  and  $\mathbf{J}_4$  have differential mode type currents on the major edges of the chassis (see Fig. 7-14 right, red arrows). A comparison of the radiation ratio of the modes excited by both antennas are shown in Fig. 7-14 left and orthogonal radiation properties can be expected.

The prototype antenna is shown in Fig. 7-15 (left). It is implemented on a 1.5 mm thick FR4 PCB. The corresponding simulations were performed using the FDTD-based EM simulator Empire [Emp15].

The impedance matching for the main antenna is implemented with a dual-resonant matching circuit [Vil07] for the low-band operation (LB). For the high-band operation (HB) the matching is implemented by a combination of the L-section matching circuitry [Poz11] and the self-resonances of the CCE. The matching circuit topology is chosen in such a way that the number of lumped elements is minimized (see Fig. 7-15 right). The inductors were chosen from the Würth Elektronik series WE-TCI0402, and the capacitor from ATC

## 7. Applications on Small Antenna Design

### RF/Microwave Capacitors Design Kit ATC KIT 26.

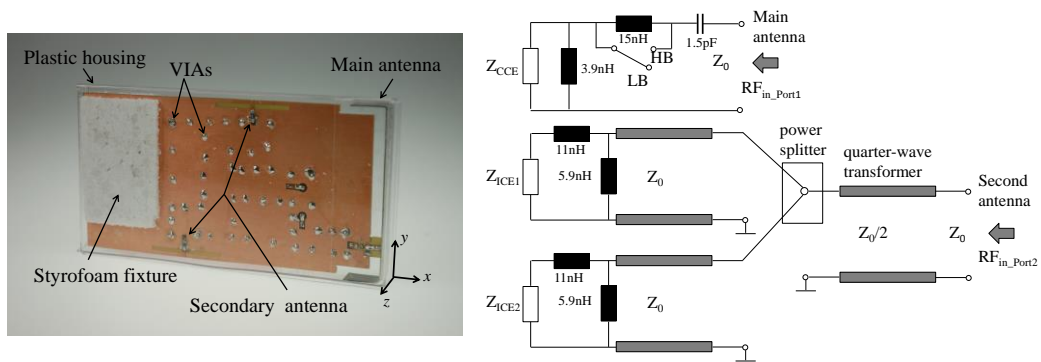


**Fig. 7-15** Mock-up system of the investigated prototype antenna (left) and the matching circuits for the main and second antenna (right). © 2013 IEEE [IV].

The switching between the LB and HB is implemented with a mechanical switch. The simultaneous operation within the LB and HB has been implemented using the dual-branch matching circuit introduced in [Val13\_1]. Each out-of-phase ICE is separately matched with an L-section matching circuit located next to the elements. The circuits must be identical in both of the L-sections. Therefore, both matching circuits care for the same amplitudes and phases. The feeds are then combined with a power splitter/combiner, after which the impedance level is optimized with a quarter-wave transformer. The required feeding structure is designed in tri-plate (stripline) technology on the backside of the same PCB [III]. Therefore, the feeding structure is not a part of the radiating system. The S-parameters of the antenna are shown in Fig. 7-16.

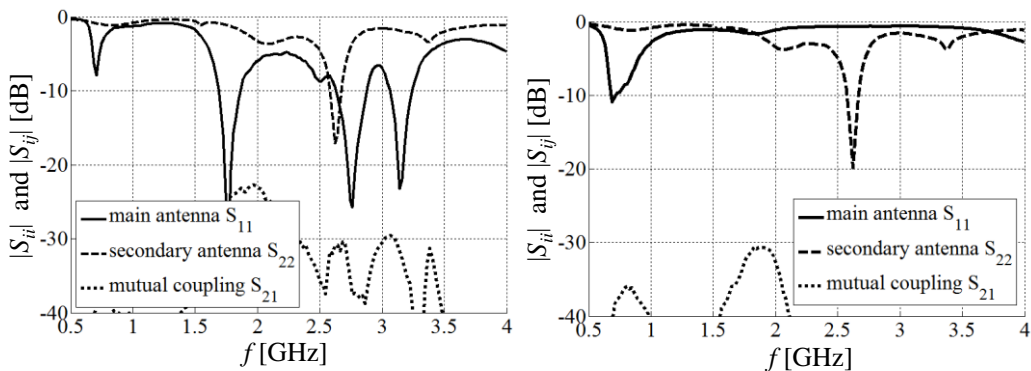


**Fig. 7-16** The s-parameters for HB (left) and LB (right) of the investigated prototype antenna. © 2013 IEEE [IV].

### 7.3 2-port antenna based on a tuned unsymmetrical CCE and a distributed pair of ICES

The matching circuit in both switching states (see Fig. 7-15 right) show promising results in terms of the return loss of the ports and EM-isolation between the ports at the high (Fig. 7-16 left) and low (Fig. 7-16 right) bands. Especially in the high-band (here HB 2.5GHz – 2.7GHz), the potential for a MIMO antenna system is demonstrated. The measured EM isolation is better than 30dB. The good isolation between the antennas can be explained by the excitation of orthogonal modes on the commonly used radiating structure (see Fig. 7-14).

The losses of the substrate material, the plastic housing and the matching circuit as well as the transmission lines decrease the total efficiency of the entire system. Table 7-3 shows the measured total efficiency for the high-band (HB: 2.5GHz - 2.7 GHz) of both the main antenna (Main Ant.) and secondary antenna (Sec. Ant.). The measured efficiencies for low-band (LB: 0.69GHz - 0.96 GHz) and other frequencies of the high-band case are shown in [IV].

**Table 7-3** Measured total efficiencies of both antennas and the envelope correlation calculated from the measured radiation pattern. © 2013 IEEE [IV].

HB-Case	2.5GHz	2.6GHz	2.69GHz
Main Ant. $\eta_{total}$	62%	63%	71%
Sec. Ant. $\eta_{total}$	39%	60%	40%
$ \rho_{Port1, Port2} $	0.007	0.064	0.03

With respect to MIMO applications, the envelope correlations were calculated from the measured complex radiation patterns and the propagation channel was modeled with isotropic and uniform environment parameters based on [Oga09]. The performance of the two-port antenna system at the high-band (here HB 2.5GHz – 2.7GHz) is excellent with respect to the calculated cross-correlation shown in Table 7-3. Therefore, the excited current distribution on the commonly used chassis (see Fig. 7-14) indicates a nearly perfect orthogonality of its related patterns, as it was expected initially based on [Gar71].

## 7.4 Multiple-port antenna based on a broadband tuned CCE and self-resonant CFCEs

<sup>4</sup>For broadband communications, the usage of the CCE antenna becomes a promising approach, as shown in previous section 7.3 and e.g. in [IV, Val13\_1, Val14]. In order to access the communications bands over a large frequency range, a broadband CCE antenna has been proposed in [Kim12]. However, a large antenna form factor (the space occupied by the antenna structure within the mobile device) is required for the design. Therefore, this section shows an inherently non-matched CCE antenna (main antenna) which is tunable and can be broadband matched to any E-UTRA band up to 2.7GHz, as shown in [VII, VIII, Mar14]. In addition, the systematic application of the TCM helps to find the optimal locations of self-resonant diversity elements based on the given location of the main antenna on the same terminal. The systematic design strategy is based on avoiding an excitation of those characteristic modes, which are excited by the broadband CCE antenna at the desired operation frequencies.

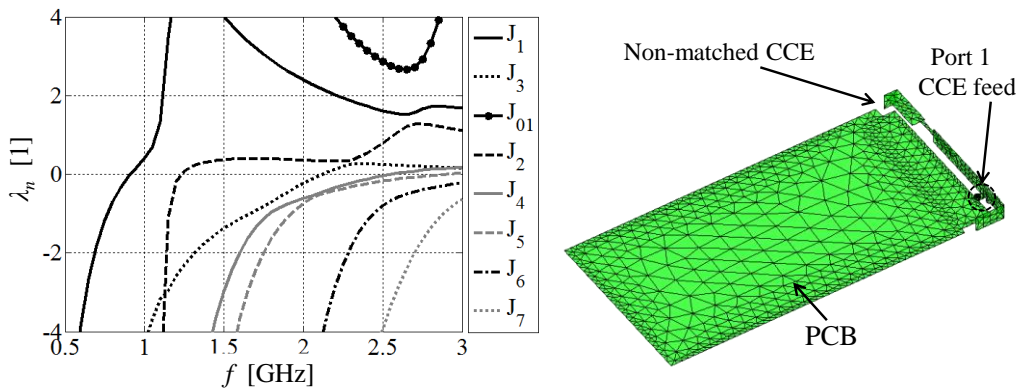


**Fig. 7-17** The eigenvalue analysis (left) of the compact handset antenna (right). © 2015 IEEE [VIII].

The main antenna, here a non-resonant CCE (see Fig. 7-17 right), has a fixed geometry and all its parameters are described in [VII]. This antenna is placed on the short edge of the PCB and it is designed to excite several characteristic modes  $\mathbf{J}_n$ . In [VII], it has been

<sup>4</sup> This section uses textual materials and figures from [VII, VIII] © IEEE 2015.

shown that this kind of antenna is four times smaller than the HCE antenna shown in section 7.2.

It can be seen in Fig. 7-17 that many modes provide low eigenvalues in the observed frequency range and heavily affect the performance if excited. Four  $\mathbf{J}_n$  in two different operating bands are excited dominantly, as shown in Fig. 7-18. Additionally, the radiation contribution is analyzed to show the relative contribution of each characteristic mode in the E-UTRA OB 2 and 7 to the total radiated power. Here, two of the four  $\mathbf{J}_n$  mainly dominate the radiation performance. Each dominant mode has its maxima of the current distribution at specific locations (black arrows) along the major edge. At these locations the mode has a minimum of the electric field distribution. Therefore, a specific mode cannot be excited if capacitive feed antennas are placed at the maxima (minima) of the dominant current distribution (electric field distribution).

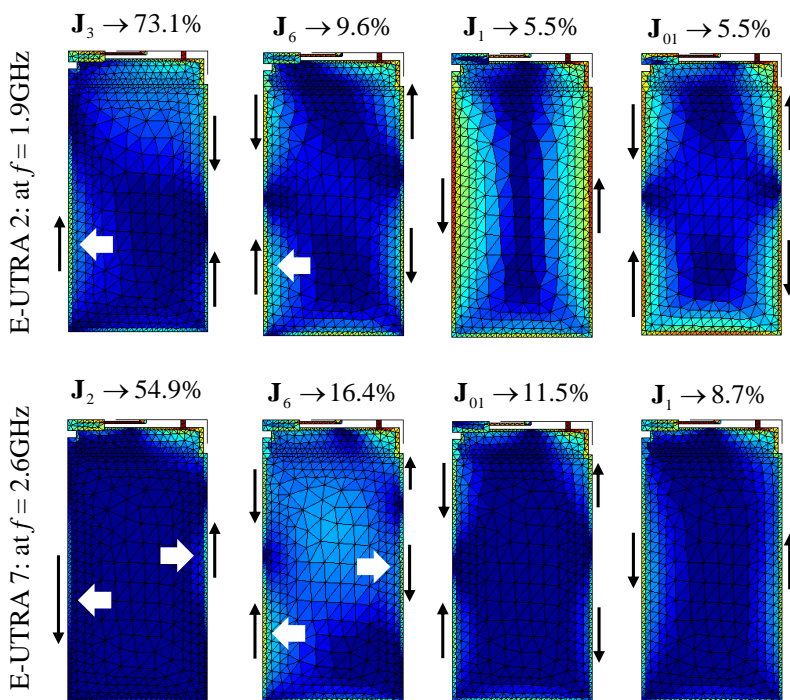


**Fig. 7-18** Normalized current distributions with maxima (black arrows), nulls (blue) and optimal placements (white arrows) at the edges of the the most dominant characteristic chassis modes in two different operation bands. 2015 IEEE [VIII].

Therefore, we are looking for a compact self-resonant diversity element with a strong capacitive coupling behavior which can be placed at the long edge of the PCB. This design

## 7. Applications on Small Antenna Design

strategy is assumed to lead to a good multi-element antenna performance.

As already discussed in sub-section 5.3.4, the CFCE is a good candidate for a matched coupling element antenna. The proposed element in Fig. 7-19 consists of two symmetrically folded arms with their open ends facing the small capacitive feed reacting as a high capacitive load. This kind of antenna structure uses mainly the electric field for the excitation and can be therefore optimally placed in the minima of the electric field distribution of the main antenna's dominant modes. The optimized gap width between the arms and the short feed point is 0.25mm, but this value is highly sensitive and can be additionally used to optimize the matching performance of the element itself. For the compactness of the element the height is fixed to  $h = 3\text{mm}$ . Only the length  $l$  is a design parameter which is used to match the element in the required operation bands. For the evaluation of the concept three optimal placements are found out, one at  $f = 1.9\text{GHz}$  and two at  $f = 2.6\text{GHz}$  (see Fig. 7-18 white arrows).

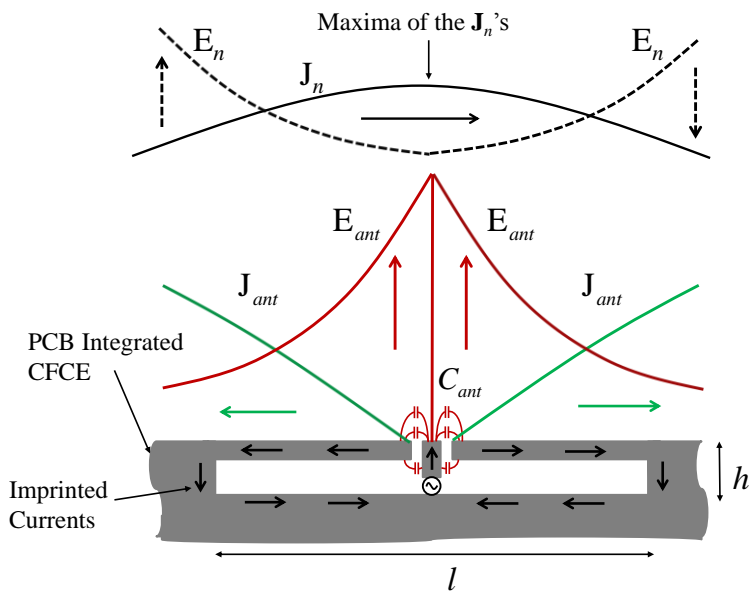


**Fig. 7-19** Self-resonant CFCE with strong capacitive feed. 2015 IEEE [VIII].

For the verification of the concept an EM-simulated 3-port antenna is designed (see Fig. 7-20) in two evaluation cases: a 3-port and 2-port MIMO antenna at the E-UTRA OB 7 (see Fig. 7-21 (a)) and OB 2 (see Fig. 7-21 (b)).

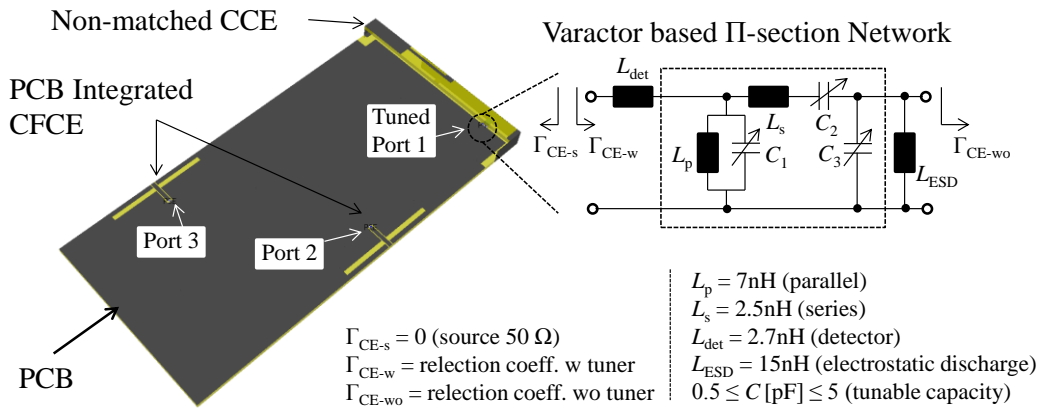


**Fig. 7-20** The 3-port antenna system with tunable CCE antenna and two integrated diversity CFCEs along the major edges of the PCB. 2015 IEEE [VIII].

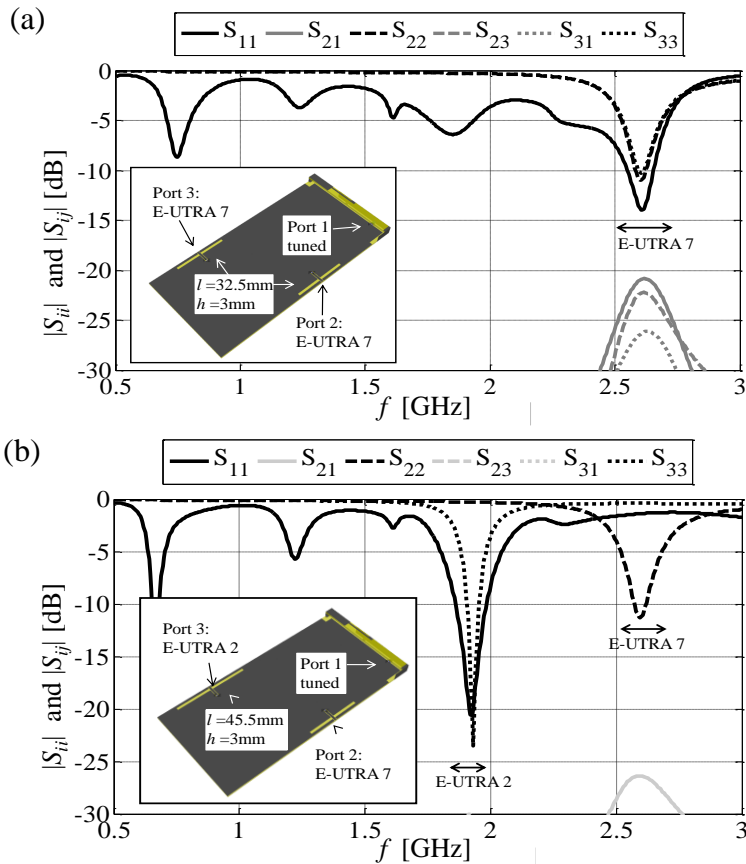


**Fig. 7-21** The results of the 3-port (a) and 2-port (b) MIMO case, here the tuned CCE antenna (black curves), the optimal placed diversity elements (black dotted curves) and the EM isolation (grey curves) for the observed E-UTRA bands. 2015 IEEE [VIII].

The non-resonant CCE is tunable and can be matched in the desired bands through two switched states in both evaluation cases [VII, Mar14]. In the first case (see Fig. 7-21 (a)) two diversity elements are placed at the predefined locations (see Fig. 7-18 at  $f = 2.6\text{GHz}$ ) along both long edges. In the second case (see Fig. 7-21 (b)) one element for the E-UTRA OB 2 (see Fig. 7-18 at  $f = 1.9\text{GHz}$ ) is placed on the left side and one another element for the E-UTRA OB 7 (Fig. 7-18 at  $f = 2.6\text{GHz}$ ) is placed on the right side along the long edge.

Both cases show that the diversity elements can be matched at the desired operation band over the length  $l$ . The proposed concept in both scenarios results in an EM isolation between the antennas of  $|S_{ij}| \geq 21\text{dB}$ .

This strategy leads to an excellent MIMO performance at the E-UTRA OB 2 and 7. The optimal locations of both antenna elements yield a high EM isolation in the operation bands. In perspective for the future, the operation bandwidth of the diversity elements can be improved by using additional matching circuits.



# Chapter 8

## Conclusion

This thesis contributes to advancing the design of efficient multiple and broadband antenna system in small handheld devices based on the TCM. The subject has first studied with a general approach by providing basis knowledge of the characteristic modes and RWG basis functions. The theory part has presented numerical formulations which has been utilized to derive a normalized power coefficient depending on the feeding port location and the excited characteristic modes. Based on that different kinds of mode coupling mechanisms and an independent control of the characteristic modes are evaluated and used for an efficient antenna design in small terminals. The evaluation has demonstrated the advantage of the selective inductive excitation and the common capacitive coupling of the characteristic modes on the chassis. The theory and the evaluation has later been used in the thesis to design four different multiple and/or broadband antenna systems, published in [I-VIII].

The physical background of the TCM has been used to analyze a generic PEC strip based on the eigenvalues, modal significances, radiating bandwidths and quality factors of the characteristic modes. A parameter study of the strip has shown that the modes can be manipulated and depending on the dimension ratio of the radiating structure and the frequency itself. A simple planar dipole structure has been used in order to manipulate the modal parameters of the modes by different dimensions. An additional feeding port enabled the mode excitation and results in different impedance matched regions. The normalized power coefficient decomposed in its modal contributions shows how heavily the different modes are excited and contributing to the absolute power delivered to the antenna. Such

## 8. Conclusion

---

analysis and manipulation have various advantages. They can be used to design compact antennas where the chassis acts an antenna without a manipulation of the modes [I, II, V] or the antenna element itself is modified for a direct manipulation of the modes [VI]. By the second concept the antenna generated additional modes on the structure itself and increases the amount of available modes on the radiation structure. Both concepts are successfully utilized in developing novel broadband/multi-band and narrow-band antenna structures for mobile terminals.

The presented work includes the selective excitation of the characteristic chassis modes by using non-resonant inductive coupling elements [I, II, III]. The ICE antennas have various advantages. They can be made very compact in size, thanks to the direct coupling in the local current maxima of the given characteristic chassis mode. Due to the efficient coupling of the modes the resulting radiation mainly depends on the dimension ratio of the chassis and their mode parameters. A desired excitation of the first three modes can be achieved and could be easily extended to a higher order mode excitation. However, in order to make the non-resonant ICE to operate at the desired frequency, its input impedance needs to be matched to the source impedance at each desired frequency band [III]. The properties of the ICE antennas are successfully utilized in developing multiple port antennas for mobile terminals [IV, V].

Also, the common excitation of several characteristic modes are presented [II]. The work includes the evaluation of the location where the best broadband bandwidth potential can be reached on the PCB. Here, the capacitive coupling in the local electric field maxima of the given characteristic chassis mode are evaluated. Different kinds of off-ground capacitive coupling elements are used to study the effects of their dimensions on the broadband operation of the CCE antenna [VI]. It has been shown that the achievable bandwidth depends on the number of the excited modes, the particular superposition of these modes as a function of frequency and the manipulation of the CCE structure itself. All of these properties are successfully utilized to develop broadband self-matched and adaptive tuned antennas for mobile terminals [IV, VI, VII].

Additionally, the systematic application of the TCM includes the goal to find optimal lo-

cations for self-resonant and matched antenna structures on the mobile terminal. This strategy avoided the excitation of those modes, which are excited by the main antenna in mobile terminals at the operation frequency. A novel capacitive feed coupling element was also designed and evaluated. The CFCE antennas have various advantages [VIII]. They can be made very compact in size, thanks to the small form factor. In addition, the CFCE can be placed in the local current maxima of the excited characteristic mode of the main antenna which results in an excellent EM isolation between both antennas.

The outcome of the content and each publication in this thesis reflects a systematic application of the TCM in designing efficient broadband and multiple antenna systems in mobile terminals [I-VIII]. Each design strategy utilized the properties of the characteristic modes and their physical background to evaluate integrated small form factor antennas, inherently non-matched antennas and broadband antennas in handheld devices. The systematic applications of TCM shows how the complexity of the antenna design in given terminals can be reduced. This can have considerable potential for further work in the field like compact massive MIMO antennas [Man16].

## Bibliography

- [And07] Andersen, J.B., and Berntsen, S., "Comments on "The Foster Reactance Theorem for Antennas and Radiation Q," *Antennas and Propagation, IEEE Transactions on*, vol.55, no.3, pp.1013-1014, March 2007.
- [Aus98] Austin, B.A., and Murray, K.P., "The application of characteristic-mode techniques to vehicle-mounted NVIS antennas," *Antennas and Propagation Magazine, IEEE*, vol.40, no.1, pp.7-21, 30, Feb 1998.
- [Bal89] Balanis, C.A., "Advanced Engineering Electromagnetics," 1th Edition, Wiley, 1968.
- [Bes03] Yaghjian, A.D., and Best, S.R., "Impedance, bandwidth, and Q of antennas," *Antennas and Propagation Society International Symposium, IEEE*, vol.1, no., pp.501-504 vol.1, 22-27 June 2003.
- [Bes04] Best, S.R., "The Foster reactance theorem and quality factor for antennas," *Antennas and Wireless Propagation Letters, IEEE*, vol.3, no.1, pp.306-309, Dec. 2004.
- [Bes06] Best, S.R., "A Discussion on Small Antennas Operating with Small Finite Ground Planes," *Antenna Technology Small Antennas and Novel Metamaterials*, 2006 IEEE International Workshop on , vol., no., pp.152-155, March 6-8, 2006.
- [CFa07\_1] Cabedo-Fabres, M., Antonino-Daviu, E., Valero-Nogueira, A., and Bataller, M.F., "The Theory of Characteristic Modes Revisited: A Contribution to the Design of Antennas for Modern Applications," *Antennas and Propagation Magazine, IEEE*, vol.49, no.5, pp.52-68, Oct. 2007.
- [CFa07\_2] Cabedo-Fabres, M., "Systematic Design of Antennas Using the Theory of Characteristic Modes," *Ph. D. Dissertation*, Universidad Politecnica De Valencia, Oct. 2007.
- [CFa07\_3] Cabedo-Fabres, M., Antonino-Daviu, E., Escuderos, D.S., and Rodrigo-Penarrocha, V.M., "On the Application of Characteristic Modes for the Analysis of Large Scale Antenna Problems," *Antennas and Propagation, 2007. EuCAP 2007. The Second European Conference on*, pp.1-7, 11-16 Nov. 2007.
- [Cha08] Chaudhury, S.K.; Chaloupka, H.J.; Ziroff, A., "Novel MIMO Antennas for Mobile Terminal," *Microwave Conference, 2008. EuMC 2008. 38th European* , vol., no., pp.1751-1754, 27-31 Oct. 2008
- [Cha10] Chaudhury, S.K., Chaloupka, H.J., and Ziroff, A., "Multiport antenna systems for MIMO and diversity," *Antennas and Propagation (EuCAP), 2010 Proceedings of the Fourth European Conference on* , vol., no., pp.1-5, 12-16 April 2010.

- [Chen14] Chen, Y., Martens, R., Valkonen, R., and Manteuffel, D., "A Varactor-Based Tunable Matching Network for a Non-Resonant Mobile Terminal Antenna", in *Antennas and Propagation (EUCAP), 2014 8th European Conference on.*, The Hague, The Netherlands, April 6-11, 2014, pp. 2225-2229.
- [Dav08] Daviu, E.A., "Analysis and Design of antenna for wireless Communications Using Modal Methods," *Ph. D. Dissertation*, Universidad Politecnica De Valencia, Oct. 2007.
- [Dia06] Diallo, A., Luxey, C., Thuc, P.L., Staraj, R., and Kossiavas, G., "Study and reduction of the mutual coupling between two mobile phone PIFAs operation in the DCS 1800 and UMTS bands", *Antennas and Propagation, IEEE Transactions on*, 2006, 54, (11), pp. 3063–3074.
- [Eth10] Ethier, J.L.T., and McNamara, D.A., "Modal significance measure in characteristic mode analysis of radiating structures," *Electronics Letters*, vol.46, no.2, pp.107-108, January 21 2010.
- [Eth10] Ethier, J.L.T., and McNamara, D.A., "Through the looking glass: A characteristic mode view of electromagnetic modeling & design," *Antenna Technology and Applied Electromagnetics & the American Electromagnetics Conference (ANTEM-AMEREM), 2010 14th International Symposium on*, pp.1-4, 5-8 July 2010.
- [Eth14] Ethier, J.L.T., and McNamara, D.A., "Antenna Shape Synthesis Without Prior Specification of the Feedpoint Locations," *Antennas and Propagation, IEEE Transactions on*, vol.62, no.10, pp.4919-4934, Oct. 2014.
- [Fam06] Famdie, C.T., Schroeder, W.L., and Solbach, K., "Numerical analysis of characteristic modes on the chassis of mobile phones," *Antennas and Propagation, 2006. EuCAP 2006. First European Conference on*, pp.1-6, 6-10 Nov. 2006.
- [Fam07] Famdie, C.T., Schroeder, W.L. and Solbach, K., "Optimal antenna location on mobile phones chassis based on the numerical analysis of characteristic modes," *Microwave Conference, 2007. European*, pp.987-990, 9-12 Oct. 2007.
- [Fos98] Foschini, G.J., und Gans, M. J., "On Limits of Wireless Communications in a Fading Environment When Using Multiple Antennas," *Wireless Personal Communications*, Vol.6, No.3, March 1998, pp. 311 - 335.
- [Fuj01] Fujimoto K., and James, J.R., "Mobile Antenna Systems Handbook," 2nd ed. Norwood, MA, Artech House, 2001.
- [Gar65] Garbacz, R.J., "Modal expansions for resonance scattering phenomena," *Proceedings of the IEEE*, vol.53, no.8, pp.856-864, Aug. 1965.
- [Gar71] Garbacz, R.J., and Turpin, R., "A generalized expansion for radiated and scattered fields," *Antennas and Propagation, IEEE Transactions on*, vol.19, no.3, pp.348-358, May 1971.
- [Gar82] Garbacz, R.J., and Pozar, D.M., "Antenna shape synthesis using characteristic modes," *Antennas and Propagation, IEEE Transactions on*, vol.30, no.3, pp.340-350, May 1982.
- [GCa08] Gómez-Calero, C., González, L., and Martínez, R., "Tri-band compact antenna array for MIMO user mobile terminals at GSM 1800 and WLAN bands", *Microwave Optical Technology Letter*, 2008, 50, (7), pp. 1914–1918.

## Bibliography

---

- [Gus06] Gustrau, F., and Manteuffel, D. "EM Modeling of Antennas and RF Components for Wireless Communications Systems," Springer-Verlag Berlin Heidelberg, Signals and Communications Technology, 1<sup>st</sup> Edition, 2006.
- [Gus12] Gustrau, F., "RF and Microwave Engineering: Fundamentals of Wireless Communications," John Wiley & Sons, New York, 2<sup>nd</sup> Edition, July 2011.
- [Had13] Hadamik, T., Martens, R., and Manteuffel, D., "Comparison of two matching networks for a LTE2600 handset antenna," *Antennas and Propagation Conference (LAPC), 2013 Loughborough*, Loughborough University, UK, pp.145-148, 11-12 Nov. 2013.
- [Har60] Harrington, R.F., "Effect of Antenna Size on Gain, Bandwidth and Efficiency," *Journal of Research of the National Bureau of Standards – D. Radio Propagation*, Paper 64D1-31, pp.1-12, Sep 1971.
- [Har68] Harrington, R.F., "Field Computation by Method of Moments," New York: Macmillan, 1968.
- [Har71\_1] Harrington, R.F., and Mautz, J.R., "Theory of characteristic modes for conducting bodies," *Antennas and Propagation, IEEE Transactions on*, vol.19, no.5, pp.622-628, Sep 1971.
- [Har71\_2] Harrington, R.F., and Mautz, J.R., "Computation of characteristic modes for conducting bodies," *Antennas and Propagation, IEEE Transactions on*, vol.19, no.5, pp.629-639, Sep 1971.
- [Har72] Harrington, R.F., and Mautz, J.R., "Control of radar scattering by reactive loading," *Antennas and Propagation, IEEE Transactions on*, vol.20, no.4, pp.446-454, Jul 1972.
- [Hol10] Holopainen, J., Valkonen, R., Kivekas, O., Ilvonen, J., and Vainikainen, P., "Broadband Equivalent Circuit Model for Capacitive Coupling Element-Based Mobile Terminal Antenna," *Antennas and Wireless Propagation Letters, IEEE*, vol.9, pp.716-719, 2010.
- [Hui14] Hui Li, Miers, Z.T., and Lau B.K., "Design of Orthogonal MIMO Handset Antennas Based on Characteristic Mode Manipulation at Frequency Bands Below 1 GHz," *Antennas and Propagation, IEEE Transactions on*, vol.62, no.5, pp.2756-2766, May 2014.
- [Ilv14] Ilvonen, J., Valkonen, R., Holopainen, J., and Viikari, V., "Design Strategy for 4G Handset Antennas and a Multiband Hybrid Antenna," *Antennas and Propagation, IEEE Transactions on*, vol.62, no.4, pp.1918-1927, April 2014.
- [Joh90] Johnson, W.A., Wilton, D.R., and Sharpe, R.M., "Modeling scattering from and radiation by arbitrarily shaped objects with the electric field integral equation triangular surface patch code," *Electromagnetics*, Vol.10, pp.41-63, 1990.
- [Kar04] Karaboikis, M., Soras, C., Tsachtsiris, G., and Makios, V.: 'Compact dual-printed inverted-F antenna diversity systems for portable wireless devices', *IEEE Antennas Wireless Propagation Letter*, 2004, 3, pp. 9–14.
- [Kin60] King, R., Harrison, C., Jr., and Denton, D., Jr., "Transmission-line missile antennas," *Antennas and Propagation, IRE Transactions on*, vol.8, no.1, pp.88-90, Jan. 1960.

- [Kiv04] Kivekäs, O., Ollikainen, J., Lehtiniemi, T. and Vainikainen P., "Band-width, SAR, efficiency of internal mobile phone antennas," *IEEE Transaction on Electromagnetic Compatibility*, vol. 46, no. 1, pp. 71–86, Feb. 2004.
- [KKi13] Kishor, K.K., and Hum, S.V., "A Two-Port Chassis-Mode MIMO Antenna," *Antennas and Wireless Propagation Letters, IEEE*, vol.12, no., pp. 690-693, 2013.
- [KKi14] Kishor, K.K., and Hum, S.V. "A Pattern Reconfigurable Chassis-Mode MIMO Antenna", *Antennas and Propagation, IEEE Transactions on*, pp. 3290 – 3298, vol. 62, iss. 6, June 2014.
- [Li10] Li, Q., Li, G., Lee, W., Lee, M., Mazzaresse, D., Clerckx, B., and Li, Z., "MIMO techniques in WiMAX and LTE: a feature overview," *Communications Magazine, IEEE* , vol.48, no.5, pp.86,92, May 2010.
- [Liu90] Liu, D., Garbacz, R.J., and Pozar, D.M., "Antenna synthesis and optimization using generalized characteristic modes," *Antennas and Propagation, IEEE Transactions on*, vol.38, no.6, pp.862-868, June 1990.
- [Lop04] Lopez, A.R., "Review of narrowband impedance-matching limitations," *Antennas and Propagation Magazine, IEEE*, vol.46, no.4, pp.88,90, Aug. 2004.
- [Lux10] Luxey, C., and Manteuffel, D., "Highly-efficient multiple antenna-systems for small MIMO devices," *Antenna Technology (iWAT), 2010 International Workshop on*, pp.1-6, 1-3 March 2010.
- [Luz78] Luzwick, J., and Harrington, R.F., "A reactively loaded aperture antenna array," *Antennas and Propagation, IEEE Transactions on*, vol.26, no.4, pp.543-547, Jul 1978.
- [Mak02] Makarov, S., "Antenna and EM Modeling with Matlab," Wiley-Interscience, John Wiley & Sons, New York, July 2002.
- [Man11\_1] Manteuffel, D., and Martens, R., "A concept for MIMO antennas on small terminals based on characteristic modes," *Antenna Technology (iWAT), 2011 International Workshop on*, Hong Kong, pp.17-20, 7-9 March 2011.
- [Man11\_2] Manteuffel, D., "MIMO antenna design challenges," *Antennas and Propagation Conference (LAPC), 2009 Loughborough*, Loughborough University, UK, pp.50-56, 16-17 Nov. 2009.
- [Man12] Manteuffel, D., and Martens, R., "Multiple antenna integration in small terminals," *Antennas and Propagation (ISAP), 2012 International Symposium on*, Nanjing, China, pp.211-214, Oct. 29 2012-Nov. 2 2012.
- [Man13] Manteuffel, D., and Martens, R., "Improved radiation pattern measurements of MIMO handheld mobile terminal," *Antennas and Propagation (EuCAP), 2013 7th European Conference on*, Gothenburg, Sweden, pp.86-87, 8-12 April 2013.
- [Man16] Manteuffel, D., and Martens, R., "Compact Multi Mode Multi Element Antenna for Indoor UWB Massive MIMO," *Antennas and Propagation, IEEE Transactions on*, 2016. (in revision)
- [Mar10\_1] Martens, R., and Manteuffel, D., "Element correlation of MIMO antennas on small terminals," *Antennas and Propagation (EuCAP), 2010 Proceedings of the Fourth European Conference on*, pp.1-5, 12-16 April 2010.

## Bibliography

---

- [Mar10\_2] Martens, R., Safin, E., and Manteuffel, D., "On the relation between the element correlation of antennas on small terminals and the characteristic modes of the chassis," *Antennas and Propagation Conference (LAPC), 2010 Loughborough*, Loughborough University, UK, pp.457-460, 8-9 Nov. 2010.
- [Mar12] Martens, R., and Manteuffel, D., "2-port antenna based on the selective excitation of Characteristic Modes," *Antennas and Propagation Society International Symposium (APSURSI), 2012 IEEE*, Chicago, USA, vol., no., pp.1-2, 8-14 July 2012.
- [Mar14] Martens, R., Chen, Y., and Manteuffel, D., "Tunability Comparison of a Capacitive Coupling Element and a Planar Inverted-F Antenna," *Antennas and Propagation Conference (LAPC), 2011 Loughborough*, Loughborough University, UK, pp.667-668, 10-11 Nov. 2014.
- [Mar16] Martens, R., and Manteuffel, D., "The Modal Power Coefficient," *Antennas and Propagation, IEEE Transactions on*, 2016. (in revision)
- [Mau73] Mautz, J.R., and Harrington, R.F., "Modal analysis of loaded N-port scatterers," *Antennas and Propagation, IEEE Transactions on*, vol.21, no.2, pp.188-199, Mar 1973.
- [Mie13] Miers, Z., Li, H.; Lau, B.K., "Design of Bandwidth-Enhanced and Multiband MIMO Antennas Using Characteristic Modes," *Antennas and Wireless Propagation Letters, IEEE*, vol.12, no., pp.1696-1699, 2013.
- [Mie13] Miers, Z.; Hui Li; Buon Kiong Lau, "Design of Bandwidth-Enhanced and Multiband MIMO Antennas Using Characteristic Modes," *Antennas and Wireless Propagation Letters, IEEE*, vol.12, no., pp.1696-1699, 2013.
- [New79] Newman, E.H., "Small antenna location synthesis using characteristic modes," *Antennas and Propagation, IEEE Transactions on*, vol.27, no.4, pp.530-531, Jul 1979.
- [Oga09] Ogawa, K., Matsuyoshi, T., and Monma, K., "An analysis of the performance of a handset diversity antenna influenced by head, hand and shoulder effects at 900 MHz," *IEEE Antennas and Propagation Society International Symposium*, vol.2, pp.1122-1125, 11-16, July 1999.
- [Poo14] Poopalaratnam, D., Kishor, K.K., and Hum, S.V., "Multi-feed chassis-mode antenna with dual-band MIMO operation," *Antennas and Propagation Society International Symposium (APSURSI), 2014 IEEE*, pp.1427-1428, 6-11 July 2014
- [Poz11] Pozar, D.M., "Microwave Engineering," John Wiley & Sons, New York, 4<sup>th</sup> Edition, Dec 2011.
- [PVa00] Pat. FI114260, Modular coupling structure for a radio device and a portable radio device, P. Vainikainen, J. Ollikainen, O. Kivekäs, and I. Kelder, Finland, Appl. 20002529, 17.11.2000, (15.09.2004), 22 p.
- [Rah06] Rahola, J., and Ollikainen, J., "Optimal antenna placement for mobile terminals using characteristic mode analysis," *Antennas and Propagation, 2006. EuCAP 2006. First European Conference on*, pp.1-6, 6-10 Nov. 2006
- [Rah09] Rahola, J., "Bandwidth potential and electromagnetic isolation: Tools for analyzing the impedance behaviour of antenna systems," *Antennas and Propagation, 2009. EuCAP 2009. 3rd European Conference on*, pp.944-948, 23-27 March 2009
- [Rah14] Rahola, J., Ludick, D., and Futter, P., "Characteristic modes and antenna bandwidth," *Antennas and Propagation Society International Symposium (APSURSI)*,



- 2014 *IEEE*, pp.1415-1416, 6-11 July 2014
- [Ren14] ‘Renata SA Lithium Ion Polymer Accumulators’, <http://www.renata.com/industrial-products/lithium-ion-polymer/>, accessed Jan. 2014
- [RFM14] ‘RFM70 2.4G RF Transceiver’, <http://www.hoperf.de>, accessed Jan. 2014
- [RWG82] Rao, S.M., Wilton, D., and Glisson, A.W., "Electromagnetic scattering by surfaces of arbitrary shape," *Antennas and Propagation, IEEE Transactions on*, vol.30, no.3, pp.409-418, May 1982.
- [Saf12] Safin, E., Martens, R., and Manteuffel, D., "Modal source reconstruction based on radiated far-field for antenna design," *Antennas and Propagation (EUCAP), 2012 6th European Conference on*, vol., no., pp.1645-1649, 26-30 March 2012.
- [Saf13] Safin, E., and Manteuffel, D., "Reconstruction of the Characteristic Modes on an Antenna Based on the Radiated Far Field," *Antennas and Propagation, IEEE Transactions on*, vol.61, no.6, pp.2964-2971, June 2013.
- [Sch06] Schroeder, W.L., Vila, A.A., and Thome, C., "Extremely Small, Wide-band Mobile Phone Antennas by Inductive Chassis Mode Coupling," *Wireless Technology, 2006. The 9th European Conference on*, vol., no., pp.407,410, 10-12 Sept. 2006
- [She08] Sanchez-Hernandez, D., "Multiband Integrated antennas for 4G Terminals," Artech House Inc., 1th Edition, July 2008.
- [Shu13] Shuai Zhang, Kun Zhao, Zhinong Ying, and Sailing He, "Adaptive Quad-Element Multi-Wideband Antenna Array for User-Effective LTE MIMO Mobile Terminals," *Antennas and Propagation, IEEE Transactions on*, vol.61, no.8, pp.4275-4283, Aug. 2013.
- [Sonk11] Sonkki, M., Antonino-Daviu, E., Ferrando-Bataller, M., and Salonen, E., "Small radiating ground plane with higher order modes," *Antennas and Propagation (EUCAP), Proceedings of the 5th European Conference on*, vol., no., pp.1243-1247, 11-15 April 2011.
- [Stu07] Stuart, H.R., Best, S.R., and Yaghjian, A.D., "Limitations in Relating Quality Factor to Bandwidth in a Double Resonance Small Antenna," *Antennas and Wireless Propagation Letters, IEEE*, vol.6, no., pp.460-463, 2007.
- [Val13\_1] Valkonen, R., Kaltiokallio, M., and Icheln, C., "Capacitive Coupling Element Antennas for Multi-Standard Mobile Handsets," *Antennas and Propagation, IEEE Transactions on*, vol.61, no.5, pp.2783-2791, May 2013.
- [Val13\_2] Valkonen, R., Ilvonen, J., Icheln, C. and Vainikainen, P., "Inherently non-resonant multi-band mobile terminal antenna," *Electronics Letters*, vol.49, no.1, pp.11-13, January 3 2013.
- [Val14] Valkonen, R., Lehtovuori, A., and Manteuffel, D., "Capacitive coupling elements - Changing the way of designing antennas," *Antennas and Propagation (EuCAP), 2014 8th European Conference on*, pp.229-233, 6-11 April 2014.
- [Van02] Vainikainen, P., Ollikainen, J., Kivekas, O., and Kelander, I., "Resonator-based analysis of the combination of mobile handset antenna and chassis," *Antennas and Propagation, IEEE Transactions on*, vol.50, no.10, pp.1433-1444, Oct 2002.
- [Vau87] Vaughan, R.G., and Andersen, J.B., "Antenna diversity in mobile communications," *Vehicular Technology, IEEE Transactions on*, vol.36, no.4, pp.149-172,

## Bibliography

---

- Nov. 1987
- [Vil06] Villanen, J., Ollikainen, J., Kivekas, O., and Vainikainen, P., "Coupling element based mobile terminal antenna structures," *Antennas and Propagation, IEEE Transactions on*, vol.54, no.7, pp.2142-2153, July 2006.
- [Vil07] Villanen, J., and Vainikainen, P., "Optimum Dual-resonant Impedance Matching of Coupling Element Based Mobile Terminal Antenna Structures," *Microwave and Optical Technology Letters*, Vol. 49, No. 10, pp. 2472 – 2477, Oct. 2007.
- [Wen00] Wen G., Jarmuszewski, P., and Yihong Q., "The Foster reactance theorem for antennas and radiation Q," *Antennas and Propagation, IEEE Transactions on*, vol.48, no.3, pp.401-408, Mar 2000.
- [Wen07] Wen G., "Reply to "Comments on "The Foster Reactance Theorem for Antennas and Radiation Q""," *Antennas and Propagation, IEEE Transactions on*, vol.55, no.3, pp.1014-1016, March 2007.
- [Wen13] Wen Ding, Gaofeng Wang, Feng Liang, and Bo Yuan, "An Enhanced Gap Source Model," *Antennas and Propagation, IEEE Transactions on*, vol.61, no.3, pp.1266-1272, March 2013.
- [Win44] Wing, A., and Eisenstein, J. , "Single- and double-stub impedance matching," *Journal of Applied Physics*, 15, pp. 615-622, 1944.
- [Yan06] Yang, F., and Rahmat-Samii, Y., "Microstrip antennas integrated with electromagnetic band-gap (EBG) structures: a low mutual coupling design for array applications," *Antennas and Propagation, IEEE Transactions on*, 2006, 51, (10), pp. 2936–2946.
- [Yee73] Yee, A., and Garbacz, R.J., "Self- and mutual-admittances of wire antennas in terms of characteristic modes," *Antennas and Propagation, IEEE Transactions on*, vol.21, no.6, pp.868-871, Nov 1973.
- [Zha13] Zhang, S., Glazunov, A.A., Ying, Z., and He, S., "Reduction of the Envelope Correlation Coefficient With Improved Total Efficiency for Mobile LTE MIMO Antenna Arrays: Mutual Scattering Mode," *Antennas and Propagation, IEEE Transactions on*, vol.61, no.6, pp.3280-3291, June 2013.

# Curriculum Vitae

## Personal Details

*Name* Robert Ledig

*Birth name* Martens

*Family status* married

## Work Experience

*07/2009 - 06/2015* Research assistant at the University of Kiel  
Working Group of Wireless Communications  
Head: Prof. Dr.-Ing. D. Manteuffel

## Education

*10/2003 - 06/2009* Studies at the University of Kiel – Germany  
Dipl.-Wirtsch.-Ing. degree in Electrical and Information Engineering and Business Management

*11/1999 - 07/2003* Higher Education School  
Grammar School of Technique and Economics, Greifswald-Germany



## Abstract

In this thesis, the Theory of Characteristic Modes (TCM) was followed, which allows principally the use of the orthogonal chassis modes, decomposed out of the current density distribution, in order to design broadband and multiple antenna systems.

A major challenge was the development of suitable coupling structures to excite several modes independently. Here, the capacitive, the inductive and the hybrid coupling concepts were discussed and compared for the selective coupling of the characteristic modes. A reconstruction of the resulting radiation patterns and the calculation of the power coefficient realized the specific coupling of the modes, the respective power budget and antenna matching as well. In particular, the results indicated a direct relationship between the characteristic modes and the low correlation of the transfer functions in multi-antenna systems. In order to show a direct coupling of the several concepts, different kind of feeding networks at the feed-point of the investigated coupling element have been developed and evaluated. Moreover, they include the power splitter and the matching networks as well.

On the development of multi-band and broadband antennas, different coupling concepts for the common coupling of several modes have been investigated. This kind of excitation could be realized by using the coupling elements itself as a tuning element or by using space efficient matching networks at the feeding port.

The results of this thesis reveals the utilization of the theory of characteristic modes for the design of the space efficient multi-antenna systems, as well as multi-band and broadband antennas by direct coupling of the chassis itself. In addition, the approach was evaluated as a useful analysis and synthesis tool for developing integrated antenna systems on small mobile terminals.